Electronic Transport Properties of DNA Sensing Nanopores: Insight from Quantum Mechanical Simulations

Von der Fakultät Energie-, Verfahrens- und Biotechnik der Universität Stuttgart
und dem Stuttgart Research Center for Simulation Technology
zur Erlangung der Würde eines Doktor-Ingenieurs (Dr.-Ing.)
genehmigte Abhandlung

Vorgelegt von

Ganesh Sivaraman

aus Kozhikode (Indien)

Hauptberichter : Jun. Prof. Dr. Maria Fyta

Mitberichter : Prof. Dr. Johannes Kästner

Mitberichter : Prof. Dr.-Ing. Joachim Groß

Tag der mündlichen Prüfung: 04.07.2017

Institut für Computerphysik der Universität Stuttgart

2017

Erklärung

Hiermit versichere ich, die vorliegende Arbeit selbstständig verfasst und keine anderen als die angegebenen Quellen und Hilfsmittel benutzt, sowie die Zitate deutlich kenntlich gemacht zu haben.

Stuttgart, den July 4, 2017

Ganesh Sivaraman

Acknowledgments

The results presented in this thesis are an accumulation of my work as a research assistant at the Institute for Computational Physics (ICP) of the University of Stuttgart from 2012 to 2016. During the same period, I was a doctoral student member of the collaborative network SFB 716 "Dynamic simulations of systems with large particle numbers" and the Graduate School Simulation Technology of the University of Stuttgart, and a guest researcher at the Division of Materials Theory, Ångström Laboratory, Uppsala University, Sweden. This research work was supported in part by the various computational resources funded by the Ministry of Science, Research and the Arts Baden-Württemberg (MWK), and DFG ("Deutsche Forschungsgemeinschaft").

I would like to thank my adviser Dr. Maria Fyta for introducing me to the research field of nanopore sequencing. I would also like to thank her for providing a lot of encouragement, support, and independence in my scientific pursuits. I wish to thank my co-advisers Prof. Dr. Johannes Kästner, and Prof. Dr.-Ing. Joachim Groß for their valuable comments and suggestions in compiling this thesis.

I am grateful to Dr. Ralph Scheicher for hosting me in his research group, results derived from that stay contributed towards this thesis, and would like to thank him. I would also like to thank Dr. Rodrigo Amorim for taking a lot of his time, and effort in training me in electronic transport theory. I would like to thank Frank Maier for the German translations. Further, I would like to thank my co-workers Bibek Adhikari, Fabio de Souza, and Rouven Steinle.

I would like to thank my current, and former colleagues especially the administrative staff at the ICP, for the pleasant working environment. Living in Germany would not have been fun with out innumerable friends, and I am grateful for their friendship.

Finally, I would like to thank my family, for their strong encouragement and support.

Stuttgart, February 2017 Ganesh Sivaraman

ABSTRACT

The translocation of DNA through nanopores is an intensively studied field as it can lead to a new perspective in DNA sequencing [1]. During this process the DNA is electrophoretically driven through a nanoscale hole in a membrane, and use different sensing schemes to read out the sequence. Within the scope of nanopore sequencing two important sensing schemes relevant to this thesis are:

1. Tunneling sequencers based on solid state nanopores embedded with gold electrodes

2. 2D materials beyond graphene

For scheme 1, an obvious improvement is to coat the gold electrode with molecules that have high conductance and can form instantaneous hydrogen bond bridges with the translocating polynucleotide thereby improving the transverse current signal [2]. The molecule that we propose is the so called diamondoid which are diamond caged molecules with hydrogen termination. Before applying such a molecule to a nanopore electrode set up, one would like to understand their interaction with DNA and its nucleobases. For this purpose, hydrogen bonded complexes formed between nitrogen doped derivatives of smallest diamondoids (i.e. adamantane derivatives) and nucleobases were investigated using dispersion corrected density functional theory (DFT) [3]. Mutated and methylated nucleobases are also taken into consideration in these investigations. DFT calculations revealed that hydrogen bonds are of moderate strength. In addition, starting from the DFT predicted hydrogen bonding configuration for each complex, rotations, and translations along a reference axis was performed to capture variations in the interaction energies along the donor-acceptor groups of the hydrogen bonds. The electronic density of states analysis for the hydrogen bonded complexes revealed distinguishable signatures for each nucleobase, thereby showing the suitability for application in electrodes functionalised with such probe molecules. In the next step, an adamantane derivative is placed on one of the electrode and nucleotides are introduced in such a way

that nucleobases form hydrogen bonds with the of the nitrogen group of the adamantane derivatives. Electronic transport calculations were performed for gold electrodes functionalised with 3 different adamantane derivatives. Four pristine nucleotides, one mutated, and one methylated nucleotides were considered. Analysis of the transmission spectra reveal that each of the nucleotides has a unique resonance peak far below the Fermi level. We have also proposed a gating voltage window to sample the resonance peaks of the nucleotide so that they can be distinguished from each other.

An alternative to tunneling sequencers would be to use nanopores built in to ultra thin metallic nanoribbons such as graphene [4]. The sequence can be read out from the in-plane current modulation resulting from the local field effect of the translocating nucleotides in the vicinity of the metallic pore edges. But the hydrophobicity of graphene makes it a difficult candidate in aqueous environment [5]. Hence in scheme 2, the aim is to model an ultra thin material that can rectify the hydrophobicity of graphene and can be a very good candidate for current modulation sequencing. Ultra thin MoS_2 (2H) monolayer exist as direct band gap semiconductor. Nanopores based on 2H phases have been reported in the literature and are not hydrophobic. By means of chemical exfoliation of the 2H phase, a meta stable 1T phase of MoS_2 has also been synthesized by various experimental groups. The 1T phase of MoS_2 is metallic. The aim of this thesis is to model a nano-biosensor template based on a hybrid MoS_2 monolayer made up of a metallic (1T) phase sandwiched between semiconducting (2H) phase. The sensor that we propose, should have only metallic nanopore edges. As a first step, we have modeled the semiconductor-metal interface, and compared them with experiments. Then an investigation to understand the influence of the increase of the metallic unit on the electronic properties is performed. Since, point defects are highly relevant to electrochemical pore growth, a point sulfur defect analysis is provided to ascertain the weakest point in the sheet. Finally to understand the effect of the interface electronic transport calculations are performed. The transmission spectra reveals a clear asymmetry in the current flow across the interface by means of gating. In the end, the relevance of such a hybrid MoS_2 material for nanopore sequencing is discussed.

Zusammenfassung

Die Translokation von DNA durch Nanoporen ist ein aktives Forschungsfeld das zu neuen Errungenschaften im Bereich der DNA-Sequenzierung führen kann [1]. Dabei wird die DNA elektrophoretisch durch eine, in einer Membran befindlichen, wenige Nanometer große Pore transportiert, um die Sequenz der DNA mit einem geeigneten Analyseverfahren auszulesen. Im Bereich der Nanoporensequenzierung sind zwei Analyseverfahren für diese Doktorarbeit relevant:

1. Tunnelstrom-Sequenzierer basierend auf Halbleiter-Nanoporen mit eingebetteten Goldelektroden.

2. 2D Materialien die über Graphen hinaus gehen.

Eine offensichtliche Verbesserung von ersterem Analyseverfahren besteht darin, die Goldelektroden mit zusätzlichen Molekülen zu beschichten, die eine hohe Leitfähigkeit aufweisen und Wasserstoffbrücken mit den durch die Pore passierenden Polynukleotiden bilden können. Dadurch kann der Querstrom und somit das Singal verbessert werden. Das Molekül, das wir hierfür vorschlagen, ist ein sogenannter Diamantoid. Diamantoide sind Moleküle mit einem diamantartigen Kohlenstoffgerüst deren Oberfläche mit Wasserstoff terminiert ist. Doch bevor solch ein Molekül in einer Nanopore an eine Elektrode angebracht werden kann, sollten die Wechselwirkungen zwischen DNA und deren Nukleobasen verstanden werden. Zu diesem Zwecke werden durch Wasserstoffbrücken verbundene Komplexe von Stickstoff-dotierten Derivaten der kleinsten Diamantoide (zum Beispiel Adamantane Derivate) und Nukleobasen mit Hilfe dispersionskorrigierter Dichtefunktionaltheorie (DFT) [3] untersucht. Veränderte und methylierte Nukleobasen werden ebenso in diesen Untersuchungen in Betracht gezogen. Die DFT Berechnungen machten deutlich, dass die Wasserstoffbrücken von mäßiger Stärke sind. Zusätzlich wurden, ausgehend von den durch die DFT Simulationen vorhergesagten Wasserstoffbrücken-Konfigurationen jeden Komplexes, Rotationen und Translationen entlang einer Referenzachse durchgeführt, um die Variationen in den Wechselwirkungsenergien entlang der Donator-Akzeptor Gruppen der Wasserstoffbrücken festzustellen.

Die Auswertung der elektronischen Zustandsdichte, der durch Wasserstoffbrücken gebundenen Komplexe, ließ unterscheidbare Signaturen für jede Nukleobase erkennen. Somit bieten sich die untersuchten Moleküle zur Funktionaliserung von Elektroden an. Im nächsten Schritt wird ein Adamantan Derivat an eine der Elektroden platziert und Nukleotiden so hinzugefügt, dass die Nukleobasen Wasserstoffbrücken mit der Stickstoffgruppe des Adamantan Derivats bilden. Elektronische Transportberechnungen wurden an Goldelektroden, die mit verschiedenen Adamantan Derivaten funktionalisiert wurden, durchgeführt. Vier reine, eine modifizierte und eine methylierte Nukleotide wurden dabei verwendet. Die Auswertung der Transmissionsspektren verdeutlichte, dass jede Nukleotide eine eindeutige Rezonanzspitze, weit unterhalb des Fermilevels, aufweist. Um die Resonanzspitzen der Nukleotide abzutasten und somit die Nukleotide voneinander unterscheiden zu können, haben wir eine zusätzliche Gatespannung eingeführt.

Eine Alternative zu Tunnelstrom-Sequenzierer könnten Nanoporen in hauchdünnen metallenen Nanobändern, wie beispielsweise Graphen [4], sein. Die DNA-Sequenz kann durch die Modulation des elektrischen Stromes in der Ebene des Nanobandes ausgelesen werden, hervorgerufen durch die lokalen Feldeffekte in der Nähe des metallenen Bereichs der Pore durch die translatierenden Nukleotiden. Aufgrund der hydrophoben Eigenschaft von Graphen ist der Einsatz von Graphen in wässrigen Umgebungen jedoch problematisch [5]. Daher ist das Ziel im zweiten Vorhaben ein hauchdünnes Material zu modellieren, welches die hydrophobe Eigenschaft von Graphen nicht aufweist und somit ein guter Kandidat für strommodulierte Sequenzierung ist. Hauchdünne MoS_2 Monolagen, in der 2H Modifikation, sind Halbleiter mit einer direkten Bandlücke. Über Nanoporen, basierend auf dieser 2H-Form, wurde in der Literatur bereits berichtet. Ebenso sind sie nicht hydrophob. Durch chemische Abtragung der 2H-Form konnten verschiedene experimentelle Gruppen eine meta-stabile 1T-Form von MoS_2 synthetisieren, welche metallisch ist. Das Ziel dieser Doktorarbeit ist eine Nanobiosensor-Vorlage zu modellerien, welche auf einer hybriden MoS_2 Monolage basiert. Diese hybride MoS_2 Monolage besteht aus einem metallenen Bereich in der 1H-Form der zwischen halbleitenden Gebieten in der 2H-Form von MoS_2 eingeschoben ist. Die Nanopore in dem Sensor, den wir hier vorschlagen, sollte nur metallische Ränder aufweisen. In einem ersten Schritt haben wir die Halbleiter-Leiter Grenzfläche modelliert und mit Experimenten verglichen. Anschließend folgte eine Analyse des Einflusses der Größe des metallenen Gebietes auf die elektronischen Eigenschaften der hybriden Monolage. Da Gitterstörstellen für das elektrochemische Porenwachstum maßgeblich relevant sind, wurde eine Punktdefektanalyse durchgeführt, um den schwächsten Punkt in der Lage

festzustellen. Um schlussendlich den Einfluss der Schnittstelle zu verstehen, wurden elektronische Transportberechnungen durchgeführt. Die Transmissionsspektren zeigten eine deutliche Asymmetrie im Ladungsfluss durch die Schnittstelle auf, in Abhängigkeit einer Gatespannung. Am Ende wird die Relevanz eines solchen hybriden MoS_2 Materials für Nanoporsequenzierung erörtert.

SCIENTIFIC CONTRIBUTIONS

Articles in peer reviewed scientific journals:

A1 **G. Sivaraman**, F. A. L. de Souza, R. G. Amorim, W. L. Scopel, M. Fyta, and R. H. Scheicher, *"Electronic transport along hybrid MoS_2 monolayers"*, *J. Phys. Chem. C* **120**, 23389 (2016)

A2 **G. Sivaraman**, R. G. Amorim, R. H. Scheicher, and M. Fyta, *"Benchmark Study of Diamondoid-functionalized Electrodes for Nanopore DNA Sequencing"*, *Nanotechnology* **27**, 414002 (2016)

A3 **G. Sivaraman**, R. G. Amorim, R. H. Scheicher, and M. Fyta, *"Diamondoid-functionalized gold nanogaps as sensors for natural, mutated, and epigenetically modified DNA nucleotides"*, *Nanoscale* **8**, 10105 (2016)

A4 **G. Sivaraman** and M. Fyta, *"Diamondoids as DNA methylation and mutation probes"*, *EPL* **108**, 17005 (2014)

A5 **G. Sivaraman** and M. Fyta, *"Chemically modified diamondoids as biosensors for DNA"*, *Nanoscale* **6**, 4225 (2014)

Other articles beyond the topics of this thesis:

O1 F.C. Maier, **G. Sivaraman**, and M. Fyta, *"The role of a diamondoid as a hydrogen donor or acceptor in probing DNA nucleobases"*, *Eur. Phys. J. E* **37**, 95 (2014)

O2 B. Adhikari, **G. Sivaraman**, and M. Fyta, *"Diamondoid-based molecular junction: a computational study"*, *Nanotechnology* **27**, 485207 (2016)

"You can know the name of that bird in all the languages of the world, but when you're finished, you'll know absolutely nothing whatever about the bird. You'll only know about humans in different places, and what they call the bird.... So let's look at the bird and see what it's doing – that's what counts. I learned very early the difference between knowing the name of something and knowing something"

Richard P. Feynman
What Do You Care What Other People Think?

Contents

Part I

Introduction

1 Introduction

1.1 DNA

Deoxyribonucleic acid (DNA) contains the genetic information of all living organisms in the form of linear chains of nucleic acids [6] (Fig.1.1). The fundamental building block of DNA is a nucleic acid monomer known as nucleotide. Each monomer unit consist of one of the four nucleobases linked to a deoxyribose sugar-phosphate group. Two of the four nucleobases namely adenine, and guanine are derivates of *purine*. The other two namely cytosine, and thymine are derivatives of *pyramidine*. The nucleotides are deoxyadenosine monophosphate (A), deoxythymidine monophosphate (T), deoxycytidine monophosphate (C), and deoxyguanosine monophosphate (G). The nucleotide in turn forms long polymer chain through the phosphodiester bond (not shown). The exceptional stability of DNA as a carrier of information is partly due to the fact that phosphodiester bridge is negatively charged, consequently repels potential nucleophilic species such as hydroxide ions. Adenine can form complementary base pair with thymine and cytosine with guanine. Hence a pair of complementary polymer sequence form double helical structure as seen in Fig. 1.1.

The genetic information stored in DNA is translated in to proteins produced. Hence, reading out the genetic information in an organism can directly lead to better understanding of gene expression by correlating with proteomics [1] data [8]. Genome sequencing might also help in deciphering of genetic disorder, cancer, viral action, and anti-biotic resistance thereby, leading to personalized medicine [9–13].

After a period of 13 years, the human genome project was completed in 2003 at a staggering cost of $2.7 billion, to sequencing the entire human genome [14]. Such a massive scientific endeavor was made possible by the Sanger sequencing (first generation) technique developed in late 1970's [15]. Introduced in 2007, the so called second generation

[1] Proteomics is the study of structure and function of all the proteins produced by a living organism.

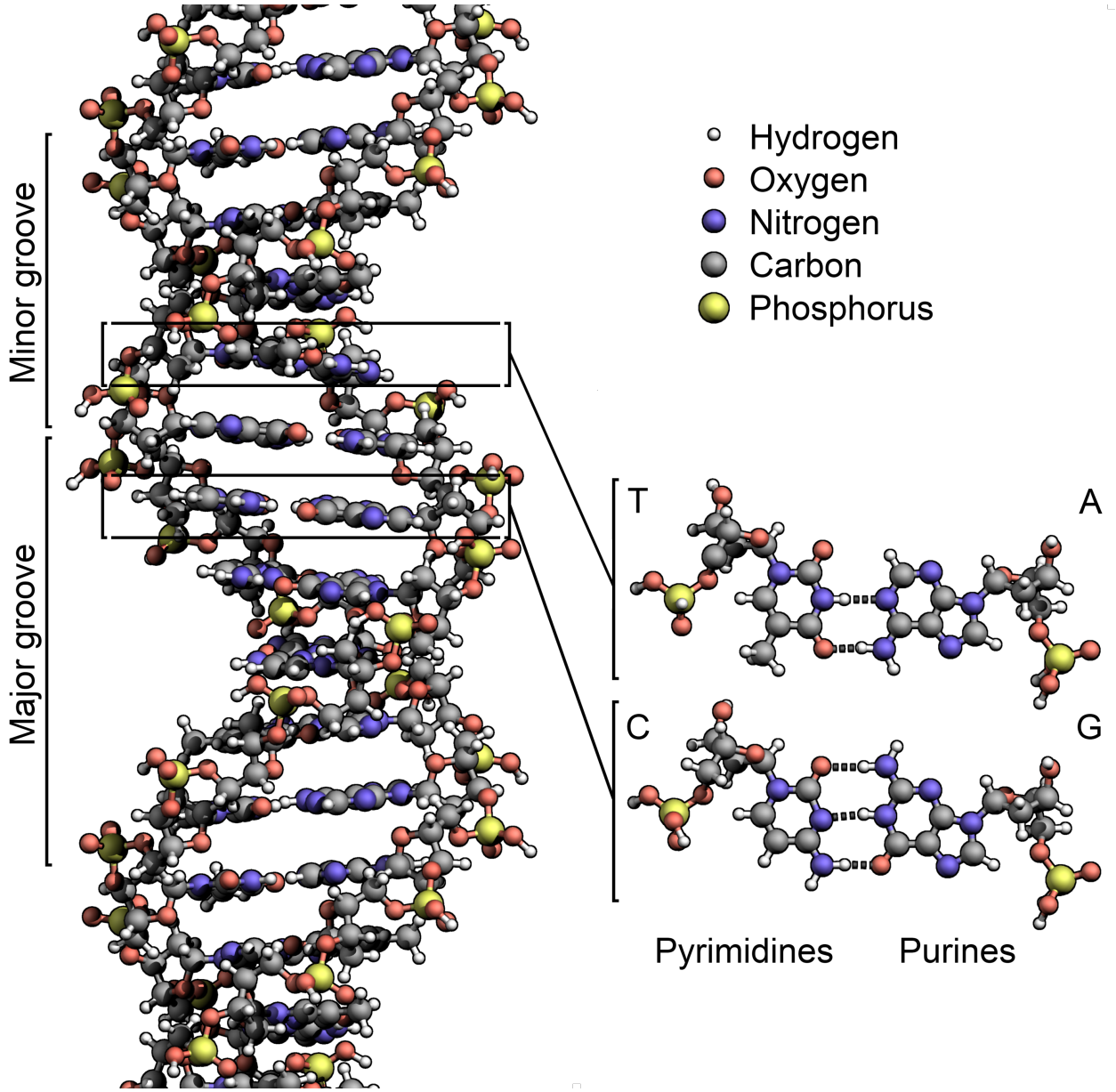

Figure 1.1: Watson and Crick model of DNA (i.e. B-DNA) [7]. The complementary base pair units are shown in the right panel. The hydrogen bond bridge formed between the pyrimidines and purines stabilize the helix. The colors denote different atom types. [Source: Wikimedia commons (DNA_Structure+Key+Labelled.pn_NoBB.png)]

techniques further reduced cost to about 1 million $ [16] for the whole genome to be sequenced in a matter of few weeks [17]. The first and second generation techniques suffer from the draw back of limited read lengths and depends on costly chemical reagents for labeling [18]. The next generation sequencing techniques (NGS) aim to rectify these drawbacks by performing the whole genome sequencing truly label free, thereby driving down the cost to about $1000 or less [19]. This thesis aims to contribute towards the

advancement of next generation sequencing techniques. Precisely the focus is a computational design of label free sensors and nanopores based on solid-state materials.

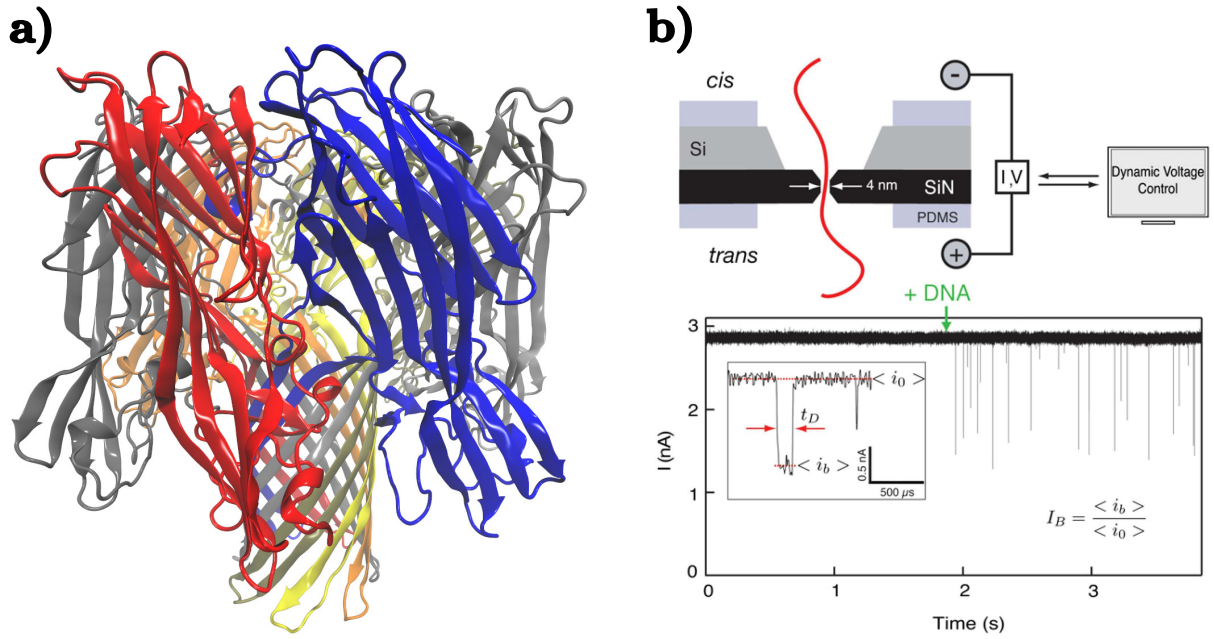

Figure 1.2: a) Structure of a biological pore protein employed in nanopore experiments. α-hemolysin pore protein from *Staphylococcal aureus* rendered with VMD [20]. Colors indicated the different chains [Source: Protein data bank ID: 7AHL] b.) Schematic diagram of DNA translocation through a solid-state nanopore with respect to bias voltage applied across the chambers. Introduction of a charged bio-polymer in the cis chamber is indicated in green and distinct blockade current spikes can been seen in the bottom panel to the right of the green arrow. One of such spikes corresponding to translocation events is zoomed and shown in the inset. Image reproduced from [21] with permission from Elsevier.

1.2 Nanopore Sequencing

Nanopores are nanometer size holes in membranes that are in contact with an aqueous electrolyte (e.g. NaCl, KCl etc.) on both sides [22]. The electrolyte flows across the channel with respect to an applied voltage and the resulting time dependent ionic current can be measured (Fig. 1.2b). A charged bio-polymer translocating across such channel could induce unique current amplitudes. Kasianowitz *et al* showed that by means of ionic current blockade originating from a polynucleotide translocating across a biological pore protein (Fig. 1.2a) embedded in lipid membrane could be used for sequencing [23]. Twenty years since this breakthrough experiment, the first devices based on biological nanopores are being commercialized by Oxford Nanopore Technologies [24].

However the ionic current measured at any point originates from a number of bases simultaneously residing in the pore, thereby requiring complex post processing to unravel sequence information [25]. Consequently techniques based on ionic current are yet to reach accuracy comparable to Sanger sequencing [26]. Ionic current sensing suffers from the draw back that it requires integration of a DNA polymerase to slow down the translocating DNA resulting in limited read length. This also means that such sensing scheme is sensitive to the nature of the translocating molecule.

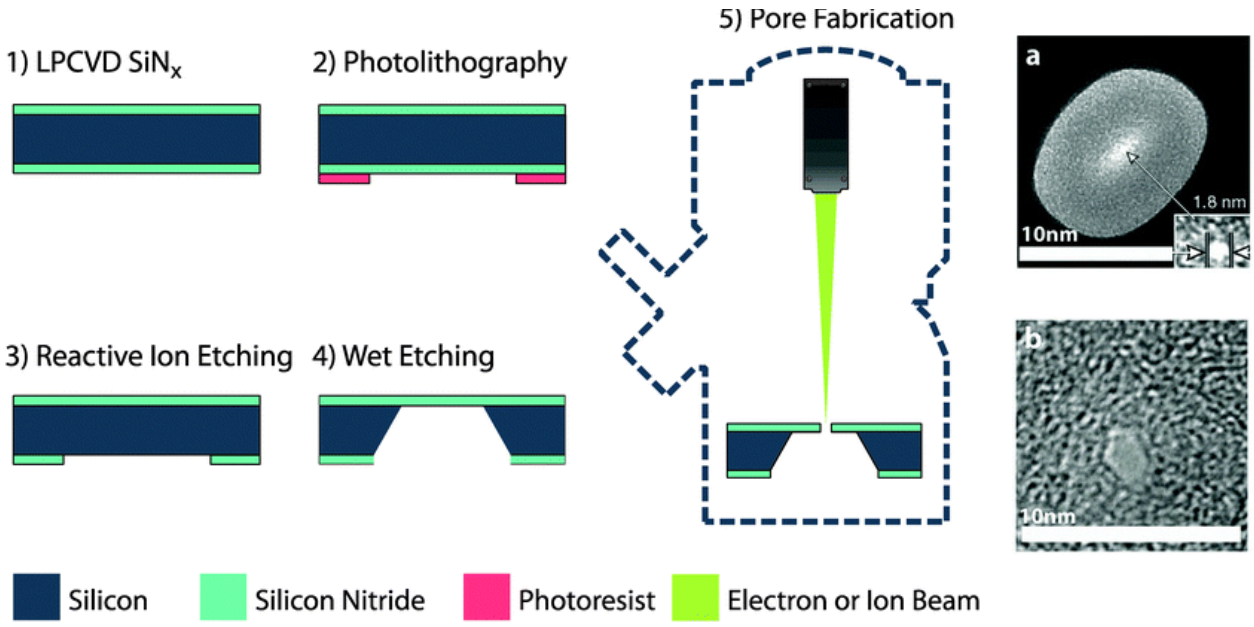

Figure 1.3: (1-4) Fabrication of a solid-state silicon nitride membrane on the top of a silicon support. (5) Incorporation of the pore in to a membrane by means of electron or ion beam. Right panel shows (a) 1.8 nm nanopore in a silicon nitride membrane formed by Ar-ion beam sculpting (b) Nanopore formed in a SiO_2 membrane formed by focused electron beam. Image reproduced from [27–29] with permission from Royal Society of Chemistry and Nature Publishing Group respectively.

Advances in semiconductor process technology has led to scalability and miniaturization of solid-state devices, fluidics, and signal processing. Hence, solid-state substrate based nanopores have been investigated for developing pores comparable in diameter to biological pores [27]. The key steps in the fabrication of solid-state nanopores has been sketched in Fig. 1.3 . The first successful single nanometer precision solid state nanopore was reported in 2001 by employing ion bean sculpting on silicon nitride membrane (Fig. 1.3a) [29]. Subsequently, Storm *et al.* reported on a direct drilling of a sub-10 nm nanopore (Fig. 1.3b) on silicon oxide by means of focused electron beam [28]. Large progress has been achieved in the field of solid-state based nanopores since the last decade, including the recent progress in to fabrication of nanopore sensors based on 2D

materials such as graphene, MoS_2, etc [18,30].

Sensing schemes beyond ionic blockade have been envisioned by means of integration of sophisticated electronics [1,27]. This thesis aims to contribute towards improvement of such a scheme, the so called tunneling sequencing [31,32]. Tunneling sequencing involves reading out the electronic structure of a single stranded DNA (ssDNA) by means of nano-fabricated mechanically controllable break junctions [33] embedded with in the solid state nanopore (Fig. 1.4a). The transverse tunneling current flowing across the nucleotides has been shown as a means for sensing [34]. The translocating ssDNA (being a charged molecule) realign with respect to the transverse voltage bias. The time scale of translocation is of the order of millisecond per nucleotide. Hence, large statistical sampling is required and the nanogap is required to be short enough to have strong enough electronic coupling with the translocating molecule and avoid potential disruption from the ionic aqueous environment [26] . Tsutsui *et al.* have show that by carefully choosing the nanogap distance (≈ 0.8 nm), thermal fluctuations and disruptions from the aqueous environment could be minimized [26,34]. The downside of choosing such a narrow gap is that the ssDNA (≈ 1.4 nm) can no longer be pulled through the nanogap and only random sampling of DNA is possible. Quantum BioSystems Inc is in the process of a commercialization based on this technology [35]. This scheme has also been shown to distinguish among amino acids which suggests that this scheme could be a potential candidate for proteomics [36]. The drawbacks include overlap of the measured current signals, background noise, and a difficulty in sensing thymine because of it's low tunneling signal [5].

One way to improve the tunneling sequencing is to functionalise the electrodes with molecules that can form hydrogen bond bridges with the nuleobases and the backbone [2] thereby improving the electronic coupling with the translocating molecule (Fig. 1.4b). This would also make it possible to use larger nanogap through which the ssDNA can be pulled.

Another sensing scheme relevant to this thesis is the so called current modulation sequencer [4, 30, 37]. This scheme involves a nanopore built in to an ultra thin metallic nanoribbon such as graphene connected to leads as shown in Fig. 1.5. Unlike a tunneling sequencer there is always a current flow (subject to a bias applied at leads) since the pore edge is metallic on all sides. Theoretical study has shown that that the in-plane nanopore current modulates (induced by variation of local density of states) due to the electrostatic interaction between pore edge and the translocating DNA [4]. The nanopore current in-turn changes as a function of the nucleobase specific electronic coupling with

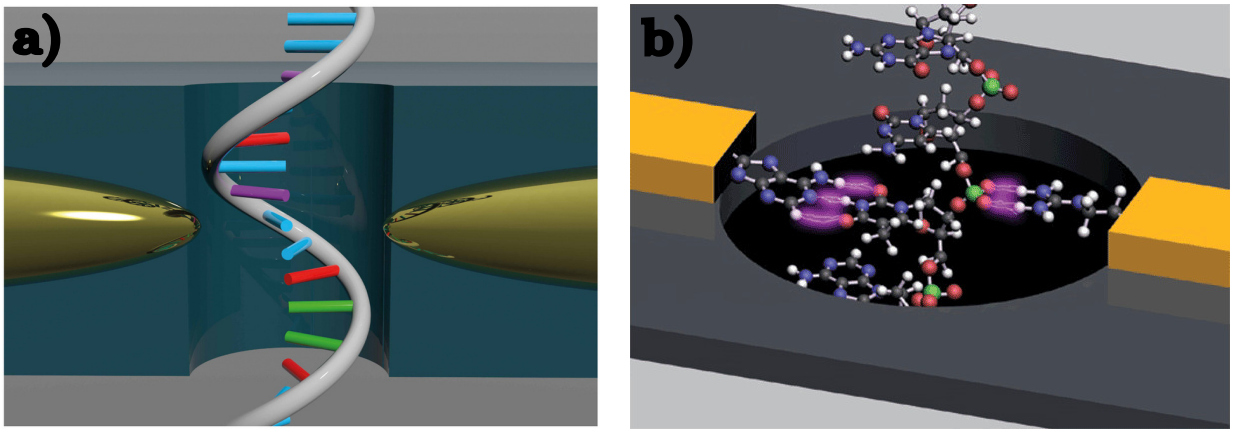

Figure 1.4: a) Schematic illustrations of gold break junction electrodes incorporated into a nanopore or nanochannel of diameter 10 nm or less (shown in Fig. 1.3). The gold nanogaps spacing on 2 nm or less. b) Modification of scheme a) by functionalizing with molecule on electrode surface that can form hydrogen bond bridges with the nucleobases and the backbone. Image reproduced from [2,36] with permission from Nature Publishing Group.

the pore edge. The advantage of this scheme being that current values of the order of μA which is much larger than the tunneling currents ($\approx$ pA) [36].

1.3 Aims

There are two fundamental aims of this thesis. The **first aim** involves the improvement of the tunneling sequencing scheme by investigating novel functionalisation groups. These can form hydrogen bond bridges with nucleobases, and thereby reduce noises in the tunneling measurements. We propose the tiny hydrogen terminated diamond caged molecules called diamondoids (Fig. 1.6) for this purpose [38]. Diamondoids occur in small amounts in earth petroleum as well as in rock crystals [39]. From Fig. 1.6, it can be observed that diamondoids comes in different shapes and sizes. These small diamond-like cages form a family of nanoscale building blocks [40,41] of which the smallest is known as adamantane. By modifying diamondoids with synthetic techniques, they can be selectively functionalized on surfaces [42]. The electronic, optical, mechanical and thermal properties of these diamondoid surfaces exhibit properties of both single-crystal diamond and nanomaterials [43,44]. It is also possible to tune the optical gap of these cages by functionalization and doping [45–47]. Diamondoids and their functional derivatives [48] have been proposed for applications such as opto-electronic devices including

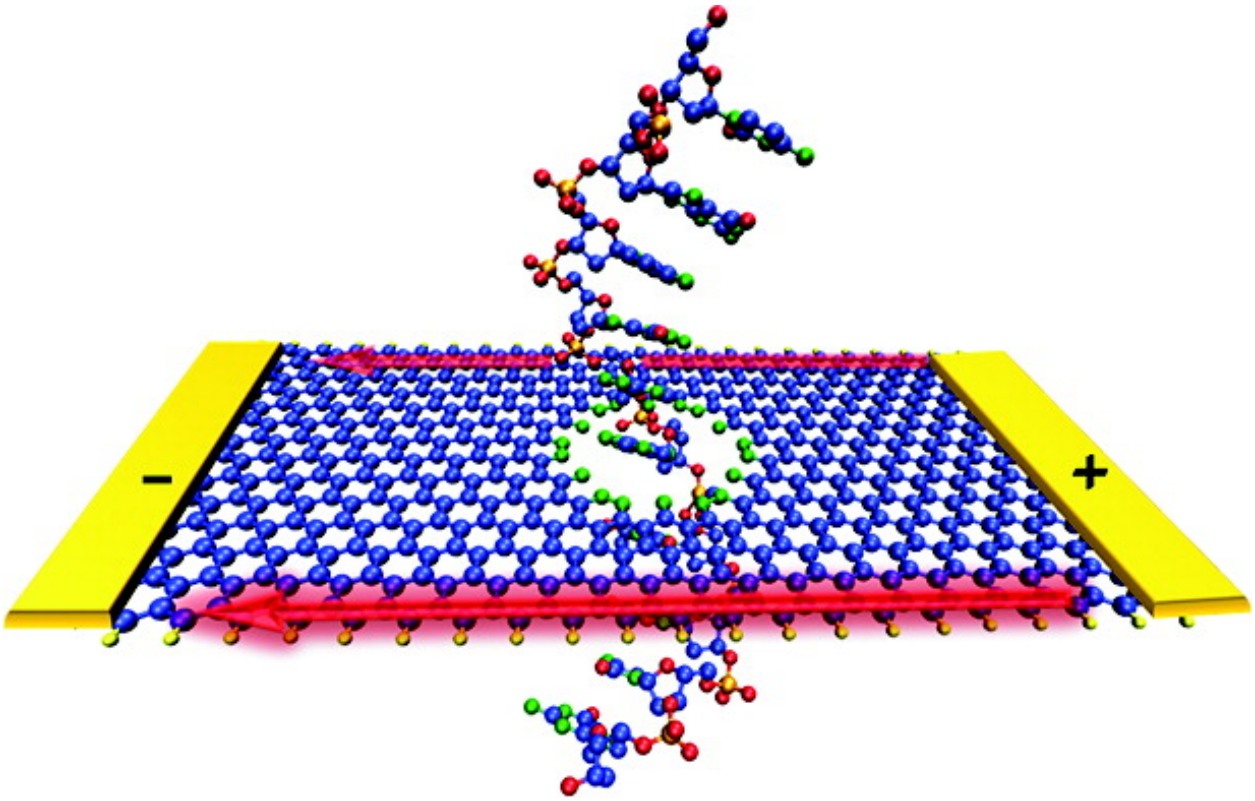

Figure 1.5: Illustration of a current modulation sensor based on zigzag graphene nanoribbon. Image reproduced from [4] with permission from American Chemical Society.

high-efficiency field emitters [48–50], single molecule biosensors [51], and as pharmaceutical agents [52]. Diamondoids can self assemble [53] and form self assembled layers on surfaces [50, 54] and ordered phases in carbon nanotubes [55].

The **second aim** is to propose and investigate ultra thin monolayers (beyond graphene) that might be an alternate candidate for achieving single base resolutions [1]. For this purpose a hybrid MoS_2 monolayer containing both metallic and semiconductor phases has been investigated as a candidate for the current modulation sensing scheme [56]. Emphasis is given on the understanding and tuning of the fundamental properties of these materials for potential biosensing applications.

Hence an overview of the thesis is presented as follows:

- An outline of theoretical schemes used in this thesis are described in chapter 2
- A detailed overview of diamondoids along with the investigation of hydrogen bonding between diamondoids, and the nucleobases are described in chapter 3

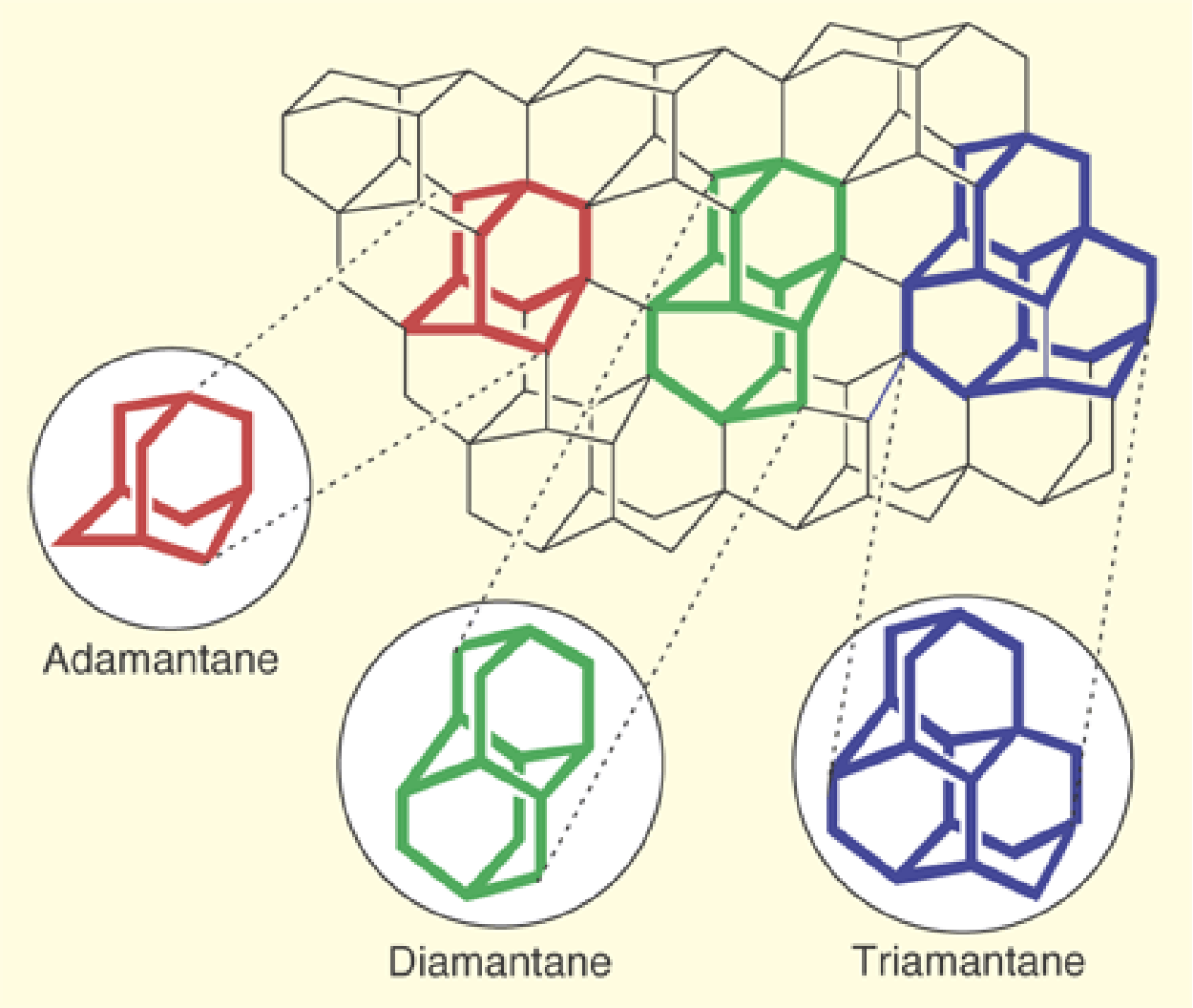

Figure 1.6: The structures of adamantane ($C_{10}H_{16}$), diamantane ($C_{14}H_{20}$), and triamantane ($C_{18}H_{24}$) segments of the diamond lattice. For clarity hydrogen atoms are omitted. Image reproduced from [38] with permission from Science.

- In chapter 4, gold electrodes functionalised with diamondoids devices are investigated. Electronic transport calculations are performed to investigate the effectiveness of such devices in discriminating nucelotides, their mutation, and methylation.
- A comparison of different diamondoid functionalised devices are provided in chapter 5
- Finally in chapter 6, alternate sensing scheme (beyond tunneling sensing) is investigated. This chapter presents the structural, electronic and transport properties of a hybrid MoS_2 monolayer in view of biosensing application.

Part II

Methodology

2 Methodology

In this chapter, an overview of the theoretical schemes relevant to this thesis will be discussed. We would start with a presentation of the quantum many-body problem. We will use a density functional approximation to perform ionic relaxation and electronic structure of the setups discussed in this thesis. Hence an overview of density functional theory (DFT) is provided. The ultimate goal of the thesis is to understand the electronic transport properties of biosensing devices. For this purpose we would end this chapter by discussing the Non-Equilibrium Green's function formalism. Note that the specific tools and parameters utilized for the actual calculations are not discussed in this chapter and for those details, the readers are advised to refer to part III.

2.1 The Many-Body Problem

All real world material involves a many-body system consisting of a system of ions and interacting electrons [57]. The state of a quantum mechanical system is described by a many-body wave function $\Psi(\{R;r\})$ and an exact theory involves solving the Schrödinger equation:

$$\hat{H}\ \Psi(\{R;r\}) = E\ \Psi(\{R;r\}) \tag{2.1}$$

where $\{R;r\}$ represents the positions of ions and electrons respectively, E is the energy of the system and $\hat{H}$ is the Hamiltonian of the system given by

$$\hat{H} = -\sum_{I}^{N_{nu}} \frac{\hbar^2}{2M_I}\nabla^2_{R_I} - \sum_{i}^{N_{el}} \frac{\hbar^2}{2m_e}\nabla^2_{r_i} - \sum_{i,I}^{N_{el},N_{nu}} \frac{Z_I e^2}{|R_I - r_i|} + \frac{1}{2}\sum_{i\neq j}^{N_{ne}} \frac{e^2}{|r_i - r_j|} + \frac{1}{2}\sum_{I\neq J}^{N_{nu}} \frac{Z_I Z_J e^2}{|R_I - R_j|} \tag{2.2}$$

where $\hbar$ is the Planck's constant divided by 2π, M_I the ionic mass of nuclear index I, m_e, mass of electron. The first two terms of $\hat{H}$ represent the kinetic energy operators for the ions and electrons respectively. The last three terms corresponds to potential energy terms for electron-ion attraction, electron-electron repulsion, and ion-ion repulsion respectively.

A simplification of the equation 2.1 can be achieved by the so called Born-Oppenheimer approximation where Ψ is explicitly dependent only on electronic degrees of freedom. A rationale for such an approximation is that ions are three to five order of magnitude higher in mass compared to electrons, hence a reasonable assumption to model the ions as classical particles in equilibrium positions. The static ions interact with electrons via $\hat{V}_{ext}$. The electronic Hamiltonian can be written as

$$\hat{H} = -\sum_{i}^{N_{el}} \frac{\hbar^2}{2m_e} \nabla_{r_i}^2 + \frac{1}{2} \sum_{i \neq j}^{N_{el}} \frac{e^2}{|r_i - r_j|} + \hat{V}_{ext} \tag{2.3}$$

Even with the Born-Oppenheimer approximation, solving for $\Psi(\{r_i\})$ is a cumbersome task because of the electronic repulsion term in equation 2.3. To tackle this issue we will present the Density Functional Theory (DFT) in the subsequent section.

2.2 Density Functional Theory (DFT)

The wave function of a many body interacting problem is too complex to be treated explicitly. An alternate idea would be to formulate the energy as a functional of ground state charge density. The Hohenberg-Kohn theorems [58, 59] provide a rigorous theoretical foundation for DFT, and are states as follows:

Theorem 1. *The ground state density $\rho(r)$ uniquely determines the potential, up to an arbitrary constant.*

The theorem 1, demonstrates that ground state charge density can be used as fundamental quantity in characterizing the system instead of external potential. But the external potential V_{ext} and number of electron N_{el} determines all the properties of the system via solving for the eigenstates of equation 2.1. This means that the wave function must be a unique functional of the charge density. Now comes the equivalence of equation 2.1 in terms of charge density. We can write down the energy functional of the system as:

$$E[\rho(r)] = F[\rho(r)] + \int V_{ext}\rho(r)dr \tag{2.4}$$

where $F[\rho(r)]$ is a universal functional of density.

Theorem 2. *The exact ground state is the global minimum value of functional* $E[\rho(r)]$.

The minimum energy obtained by theorem 2 would be greater than or equal to the ground state energy calculated by solving equation 2.1. But the universal functional $F[\rho(r)]$ is unknown and hence the exact application of DFT does not exist. A reasonable approximation to simplify the many body problem is to consider the so called "Kohn-Sham electrons" that do not interact with each other and interacts with an external potential, so that their ground-state charge density is identical to the charge-density of the interacting system. The single-particle Kohn-Sham equations can be written as :

$$H_{ks}\Phi_i = \epsilon_i\Phi_i \tag{2.5}$$

with Φ_i being the i-th Kohn-Sham wave function having the eigenvalue ϵ_i.

$$H_{ks} = -\frac{\hbar^2}{2m_e}\nabla_i^2 + V^{eff}, \tag{2.6}$$

$$V^{eff} = e^2\int\frac{\rho(r')}{|r-r'|}dr' + V_{xc} + V_{ext}, \tag{2.7}$$

$$V_{xc} = \frac{\delta E_{xc}[\rho(r)]}{\delta\rho(r)} \tag{2.8}$$

where in equation 2.6, the first term is the kinetic energy of the Kohn-Sham electrons. In equation 2.7, the first terms is the Hartree potential corresponding to electron-electron Coulomb repulsion. V_{ext} is the Coulomb potential due to the interaction between electrons and the ions.

The electronic wave function must satisfy the Pauli exclusion principle, i.e. if two electrons of same spin interchange position then Ψ must change sign. This is known as *"exchange"* property. The motion of an electron is influenced by the motion of every other electrons. This is known as *"correlation"* property. The E_{xc} (or V_{xc}) accounts for the **exchange-correlation** property, which is an unknown functional of charge density that needs to be approximated. The simplest approximation is to consider a uniform

electron gas where the exchange-correlation energy is only dependent on charge denisty at each point in space, hence referred to as the Local Density Approximation (LDA) [59] to Density Functional Theory. The exchange-correlation energy within the LDA can be written as :

$$E_{xc} = \int (\epsilon_x[\rho(r)] + \epsilon_c[\rho(r)])\rho(r)dr \tag{2.9}$$

The exchange energy density (ϵ_x) can be approximated by using the Hartree-Fock exchange energy per electron and generalizing to situations where density is not uniform. A number of expressions has been derived for the correlation energy density (ϵ_c) by fitting to energy of uniform electron gas at different densities. The biggest drawback of LDA comes from the fact that non-local many body effects are missing. Hence, it poorly describes bonded interactions in molecules and non-covalent interactions. An improvement to LDA is the so called generalized gradient approximations (GGA), where the energy also depends on the gradient of density ($\nabla\rho(r)$). Historic development of GGA functionals can be broadly classified in to two branches of ideas. The first branch of GGA functionals achieved gradient correction by means of parameters derived from fitting to specific system (e.g. BLYP [60, 61]). The second branch guided by the work of John Perdew, achieved gradient correction by means of parameters derived from exact quantum mechanical conditions (e.g. PBE [62]). The universal functional of density is still unknown and the development of exchange-correlation functional is a very active field in density functional theory community [63].

Equation 2.5 does not represent the true electronic wave function (i.e. Ψ), but only the non-interacting single particle wave function (i.e. Φ). The charge density can be computed from the Kohn-Sham wavefunctions as follows:

$$\rho(r) = \sum_{i}^{N_{el}} f_i |\Phi_i|^2 \tag{2.10}$$

where f_i is the occupation numbers corresponding to the single particle eigenstates.

2.2.1 Practical Aspects of DFT

The single particle Kohn-Sham equation 2.5, involves a set of N_{el} coupled, three dimensional, partial differential equations [64]. For obtaining the ground state of the system

the Kohn-sham equation can be solved as follows:

1. Pick an initial guess for the charge density $\rho(r)$.
2. Construct the H_{ks}.
3. Construct Φ_i by solving equation 2.5.
4. Calculate the new charge density using equation 2.10.
5. Iterate till self-cosistent charge densities are obtained.

In order to implement an iterative scheme discussed above, two important factors need to be addressed :

- **Treatment of electron-ion interaction:** In equation 2.7, the electron-ion interaction is treated as the bare Coulomb interaction. But electrons can be distinguished based on the way they contribute towards chemical bonding. Electrons which directly contribute towards chemical bonding are called *valence electrons* and those bound tightly to the ionic nucleic are called *core electrons*. All-electron methods are a class of methods which deal explicitly with all the electrons in the system. Another approach is the so called "pseudopotential" method. There is a minimal contribution towards chemical bonding by the core electronic states of an atom. Hence, the core electrons can be replaced with an effective screened potential known as pseudopotential. An approach for the construction of pseudopotentials is discussed in section 2.2.2.
- **Mathematical representation of single-particle orbitals:** The basis sets for expanding Kohn-Sham orbitals can be broadly classified into four categories.
    1. *Extended basis sets:* are delocalized, floating or atom centered type. Due to their extended nature, they are suitable for solids or liquids, but they might not be efficient for molecular systems.
    2. *Localized basis set:* are localized basis functions which can be centered at atom, or at bonds or even at the positions of 'ghost' atoms. Since this category of basis set is relevant to this thesis an example has been discussed in section 2.2.3. These are suitable for molecular system as well as for periodic systems.
    3. *Mixed basis sets:* are designed to take into account the best of the first two categories as they include extended as well as localized basis functions. But such a design might also lead to technical difficulties (e.g. over-completeness).

4. *Augmented basis sets:* in a spherical region around nuclei, an atom-centered or extended basis set is augmented with the atomic-like wave functions. Advantages include flexibility, ease of control over tuning and accuracy. Disadvantages include technical difficulties.

2.2.2 Pseudopotentials

The pseudopotentials employed in our DFT calculations are constructed from all electron atomic calculations by solving self-consistently the radial Kohn-Sham equation:

$$\left[-\frac{1}{2}\frac{d^2}{dr^2} + \frac{l(l+1)}{2r^2} + V[\rho;r] \right] rR_{nl}(r) = \epsilon_{nl} rR_{nl}(r) \tag{2.11}$$

where $V[\rho;r]$ is the self-consistent one electron potential

$$V[\rho;r] = -\frac{Z}{r} + V_H[\rho;r] + V_{xc}[\rho(r)] \tag{2.12}$$

$\rho(r)$ is the sum of the electron densities for the occupied wave function $R_{nl}(r)$, $V_H[\rho;r]$ is the Hartree potential and V_{xc} is chosen approximation to the exchange-correlation potential. The pseudopotentials are constructed in such a way that the following four conditions are satisfied:

- The pseudo-wave function generated from the pseudopotential should contain no nodes.
- Beyond a chosen cutoff radius r_{cl}, the normalized atomic radial pseudo-wave function (PP) with angular momentum l is equal to the normalized radial all-electron wave function (AE).

$$R_l^{PP}(r) = R_l^{AE}(r) \; for \;\; r > r_{cl} \tag{2.13}$$

- The charge enclosed with in the r_{cl} must be equal for AE and PP.

$$\int_0^{r_{cl}} |R_l^{PP}(r)|^2 r^2 dr = \int_0^{r_{cl}} |R_l^{AE}(r)|^2 r^2 dr \tag{2.14}$$

- The valence eigenvalues must be equal for AE and PP.

$$\epsilon_l^{PP} = \epsilon_l^{AE} \tag{2.15}$$

A pseudopotential that satisfies the above four conditions is called "norm-conserving pseudopotential" [65]. An illustration of the valence state of an anonymous atomic species can be seen in Fig. 2.1.

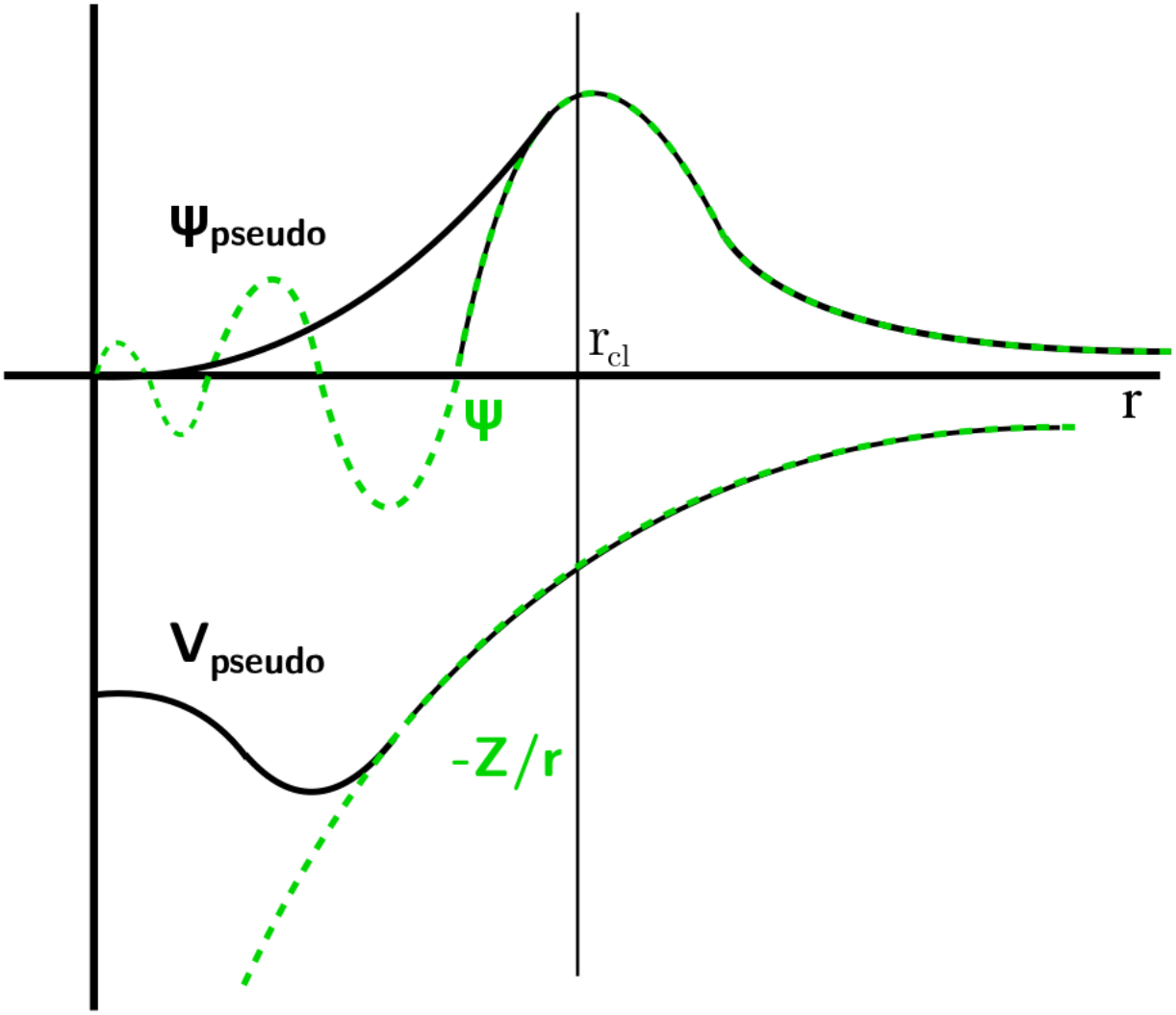

Figure 2.1: Illustration of pseudopotential for an arbitrary valence state. Top panel: All electron wave function (dashed line) and pseudo-wave function (solid line). Bottom panel: unscreened Coulomb potential ($-\frac{Z}{r}$), where Z is the atomic number and pseudopotential.

2.2.3 Numerical Atomic Orbitals (NAO)

Numerical atomic orbitals (NAO) is a localized basis set where the valence electronic states are constructed from strictly localized linear combination of atomic orbitals (LCAO). This means that after a cut-off radius the orbitals vanishes. This in-turns leads to a speed up of computations by sparsity of Hamiltonian and overlap matrices. With in the cutoff radii, the atomic orbital can be described as a product of a numerical radial term ($R_{n,l}$) for orbital n, with a spherical harmonic function ($Y_{l,m}(\theta, \upsilon)$) [66].

$$\Phi_{lmn}(r, \theta, \upsilon) = R_{n,l}(r) Y_{l,m}(\theta, \upsilon) \tag{2.16}$$

where l is the orbital angular momentum and m is the magnetic quantum number. The radial term is constructed by solving the Kohn-Sham Hamiltonian for the isolated pseudo-atom on a radial grid with a strict localization. Following the nomenclature of quantum chemistry, the NAO basis set goes from low quality, 'minimal' single ζ (SZ) to high quality, multiple ζ with polarization, and diffuse orbitals to achieve convergence in tune with quantum chemistry calculations. The SZ basis set has a single radial function per angular momentum channel. Higher ζ functions are constructed by employing split valence scheme. The angular flexibility is obtained by adding shells of higher angular momentum.

2.2.4 Basis Set Superposition Error (BSSE)

Calculations performed with real space basis functions with finite range add artifacts to the energy of weakly bound complexes (e.g. base pairs in DNA). As the weakly bound monomers approach each other, atoms from one monomer will borrow basis function from another and vice versa, resulting in artifacts in calculated property such as association energy of weakly bound complexes. This is known as the basis set superposition error (BSSE), which can be rectified by the Boys and Bernardi counterpoise correction [67]. For a complex ('12') formed from monomer '1' and monomer '2', the uncorrected association energy can be written as :

$$\Delta E_{12} = E_{12}^{12} - E_1^1 - E2^2 \tag{2.17}$$

E_{12}^{12} is the energy of the complex evaluated with the dimer basis set. E_i^i with i=1,2 are the energies of the isolated monomers evaluated with their own basis set. Let us write

down the counterpoise correction to equation 2.17, by removing the energy of monomer '1' evaluated in its own basis set from the energy of monomer '1' in the dimer basis set (i.e. '12').

$$E_1^{BSSE} = E_1^{12} - E_1^1 \tag{2.18}$$

$$E_2^{BSSE} = E_2^{12} - E_2^2 \tag{2.19}$$

The counterpoise corrected association energy of the complex (ΔE_{12}^{CP}), is obtained by subtracting the error estimated in equations 2.18, 2.19 from the uncorrected equation 2.17.

$$\Delta E_{12}^{CP} = E_{12}^{12} - E_1^{12} - E_2^{12} \tag{2.20}$$

2.3 Electronic Transport Theory

A large section of this thesis is devoted to understanding the electronic transport across nanoscale devices. Such application involve molecular systems or nanoribbons coupled to bulk electrodes. An example of a molecular electronic device[1] has been illustrated in Fig. 2.2a. A bias voltage (V_b) applied across the electrodes drives the electrons through the device resulting in the current flow. In Fig. 2.2a, it can be observed that the device region (C) consists of a molecule along with a few layers of metal (taken from the electrodes). This device in-turn is coupled to semi-infinite electrodes (L / R) on either side. This partitioning of a nanoscale electronic device in terms of a finite device region (C) coupled to semi-infinite electrodes (L/R) will be used for discussions in this subsection.

A relevant theoretical scheme must capture some of the following aspects of such devices:

- Non-equilibrium nature of the electronic transport process.
- Accurately model the periodic nature of the semi-infinite electrodes.
- In order to accurately model the charge transfer effect at the metal-molecule contact, some of the metal atoms belonging to electrodes at the contact region with the molecule is included in to the device region.

[1]Molecular electronics is a field of nanotechnology that envisions electronic component constructed out of molecules [68]

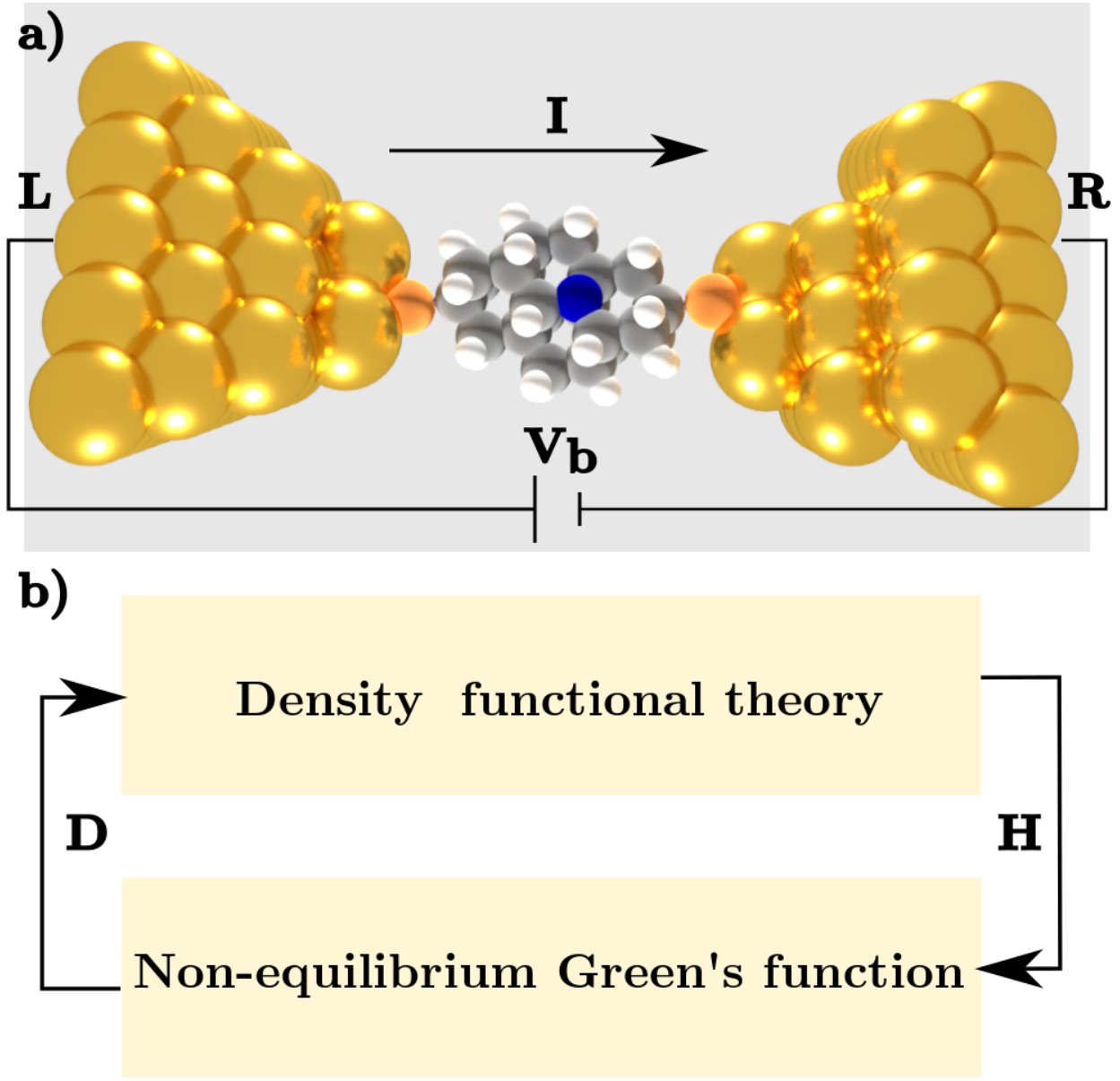

Figure 2.2: a) Illustration of a molecular junction. A diamantane molecule is coupled to a gold electrode via a thiol linkage. Few layers of gold along with the sandwiched molecules forms the device region (C). The device in turn is coupled to bulk electrodes or semi-infinite leads (L/R) on the either side. Application of voltage bias across the junction leads to a current flow from the source electrode (L) through the molecule towards the drain electrode (R). b) The self-consistent loop of the NEGF + DFT method.

- The number of layers of the metal included in the contact region of device must be enough to screen the semi-infinite electrodes from the coulomb potential induce by metal-molecule contact.

In the previous section, the DFT method was introduced as a first principle technique

[2] for describing electronic structure of wide variety of materials. Though DFT, cannot describe ground state, non-equilibrium electronic transport processes. DFT can only describe finite, molecular or periodic systems. Clearly, conventional electronic structure theory methods such as DFT are not suitable for the treatment of open boundary problems such as molecules coupled to source and drains electrodes. It will be shown later in this section that the equilibrium ground state DFT method can be couple to advanced non-equilibrium formalism for capturing the electronic transport process.

Before delving into the details of the theoretical treatment of relevant open boundary problems, let us start with a discussion of different transport regimes [69]. In comparison to the device length (L), defining the two characteristic lengths: i) mean free path (L_m), which is the mean distance electron needs to travel before the original momenta is lost and ii) phase relaxation length (L_ϕ), which is the mean distance electron needs to travel before the original phase is lost. The classical ohmic behavior is usually observed for scenarios when the device length, $L >> L_m, L_\phi$.

1. **Ballistic transport regime: $\mathbf{L << L_m, L_\phi}$.** The electronic transport process is devoid of scattering, and the geometry alone dictates the device conductance. Graphene exhibits ballistic transport with conductivity quantized on the sub-micrometer scale [70].

2. **Elastic and coherent transport regime: $\mathbf{L < L_m, L_\phi}$.** An incoming electron gets elastically scattered at the metal-molecule junction resulting in reduction of transmission with out involving energy or phase change. The resonant tunneling in short molecules usually belongs to this transport regime. The problems discussed in this thesis are in the context of this regime.

3. **Inlastic and incoherent transport regime: $\mathbf{L \geq L_m, L_\phi}$.** The device length is sufficiently long so that the incoming electron gets inelastically scattered by phonons or other electrons, leading to energy loss or dephasing.

The Keldysh non-equilibrium Green's function method (NEGF) provides a theoretical framework for modeling all the three electronic transport regimes [71, 72]. since the problems treated in this thesis belongs to the elastic transport regime, an overview of the NEGF method coupled to DFT would be provided in the next section relevant to that regime. Hence, enthusiastic readers are advised to consult the comprehensive literatures already available in this field [73–75].

[2] with in the limitations of exchange-correlation functional

2.3.1 Elastic Transport Regime

The localized NAO basis set discussed in section 2.2.3, offers the possibility to extend stable numeric calculations to a system size of hundreds of atoms. This also means that a numerically efficient implementation of DFT coupled to NEGF can model nanoscale devices coupled to semi-infinite electrodes with different electrochemical potentials. DFT is a natural choice for coupling to NEGF because charge density can be directly obtained from NEGF as well. The only empirical term that goes in to these calculations are the exchange-correlation functional, and the commonly used GGA functional flavor is found to deliver reasonable insights in to the transport processes in devices considered in this thesis.

Referring to the system set up discussed in Fig. 2.2a and related nomenclatures. The discussion is within the framework of localized NAO basis sets, that vanish after finite cut-off radius. Consequently all of the overlap or Hamiltonian matrix elements between atoms sitting at two different electrodes will be zero. Hence, the two electrodes (L / R) only interact with each other through the central device region (C). The first step involves the construction of Hamiltonian, and the overlap matrices using DFT for the device (C), and the semi-infinite electrodes (L/R) as follows:

$$H = \begin{bmatrix} H_L & H_{LC} & 0 \\ H_{CL} & H_C & H_{CR} \\ 0 & H_{RC} & H_R \end{bmatrix}$$

and

$$S = \begin{bmatrix} S_L & S_{LC} & 0 \\ S_{CL} & S_C & S_{CR} \\ 0 & S_{RC} & S_R \end{bmatrix}$$

The Hamiltonian is assumed to be converged to bulk values for the left (L), and right electrode (R) regions. The Hamiltonian, and the overlap matrices vary from the bulk values for the L-C, C and C-R regions. Self energy captures the readjustment of the molecular energy level due to the contact effect, and also the semi-infinite nature of leads. The self energy for the metal-molecular contact is given by:

$$\Sigma_{(L/R)}(E) = \gamma^{\dagger}_{(L/R)}(E) g^{r}_{(L/R)}(E) \gamma_{(L/R)}(E) \tag{2.21}$$

where $\gamma_{L/R}(E) = [H_{C(L/R)} - ES_{C(L/R)}]$ is the interaction between the respective leads, and the molecule. $g^{r}_{L/R}(E)$ is the surface Green's for the individual leads. Once the self energies, and Hamiltonian are set up, the retarded Green's functions can be constructed according to:

$$\mathcal{G}\left(E, V_b\right) = \left[E \times S - H - \Sigma_{\mathrm{L}}\left(E\right) - \Sigma_{\mathrm{R}}\left(E\right)\right]^{-1} \tag{2.22}$$

E and V_b correspond to the energy and the applied bias voltage, respectively.

The retarded Green's function is directly related to the electron density by means of the following two equation:

$$\rho(r) = \sum_{\alpha\beta} D_{\alpha\beta} \Phi_{\alpha}(r) \Phi_{\beta}(r) \tag{2.23}$$

and

$$D = -\frac{1}{\pi} \Im \int \left[\mathcal{G}\left(E, V_b\right) f(E - \mu)\right] dE \tag{2.24}$$

where $\Phi_{\alpha/\beta}(r)$ is the numeric atomic orbital. The density matrix element $D_{\alpha\beta} = \sum_i f_i c^{*}_{\alpha i} c_{\beta i}$ with f_i and $c_{\alpha/\beta i}$ being the occupancy, and expansion coefficient for the $\Phi_{\alpha/\beta}(r)$ of the i-th state, respectively.

One can observe that the charge density is directly accessible from the retarded Green's function, but the Hamiltonian itself is in turn dependent on the electron density. Hence, within the NEGF + DFT method, the charge density is calculated self-consistently using Green's functions, until convergence is achieved as shown in Fig. 2.2b. Accordingly, the electronic transmission $T(E)$ can be written as:

$$T\left(E, V_b\right) = Tr\left[\Gamma_{\mathrm{L}}\left(E, V_b\right) \mathcal{G}\left(E, V_b\right) \Gamma_{\mathrm{R}}\left(E, V_b\right) \mathcal{G}^{\dagger}\left(E, V_b\right)\right] \ , \tag{2.25}$$

with the matrix $\Gamma_{(L/R)}(E) = i\left[\Sigma_{(L/R)} - \Sigma^{\dagger}_{(L/R)}\right]$. The transmission function $T(E)$ represents the fraction of electrons transmitted from source electrode (L) to the drain electrode (R) via the central device region (C). Further details on the theory and also the implementation can be found in the literature [76]. The last theoretical aspect raised here is the Keldysh formalism leading to the local current or the current between two states M and N as:

$$i\left(E\right)_{N \to M} = 4\frac{e}{h} \sum_{\substack{n \in N \\ m \in M}} \Im\left[\left\{\mathcal{G}\left(E\right) \Gamma_{\mathrm{L}} \mathcal{G}^{\dagger}\left(E\right)\right\}_{mn} H_{nm}\right] \tag{2.26}$$

Here, the sum is performed over all orbitals m(n), associated with the sites M(N), respectively. For a zero bias calculation, the local current maps the transmittance projection between two states M and N.

Part III

Results

3 Investigation of bonding between diamondoid molecules and nucleobases

3.1 Introduction

DNA carries the genetic information of all living organisms. In this respect, a lot of efforts have turned into novel biotechnological applications which could sense biomolecules, such as DNA, and read-out efficiently the information therein. One of the promising candidate for a future label free DNA sequencing technology is a nanopore based DNA sequencer [2, 19, 22]. In this technique a single-stranded DNA molecule is translocated through a nanometer-sized pore by electric means. Transverse current measurements can lead to the identification of the nucleotide sequence, for which the signal-to-noise ratio is still too low. The biosensing properties of the nanopore, though, could be enhanced through functionalization of the nanopore [2, 27]. The specific interaction of the functionalizing molecule (Fig. 1.4b) with the DNA units has the potential to reduce the noise in the transport measurements [77]. It is thus important to search for a molecule, which could specifically bond to each DNA nucleobase and lead to distinct signals. These molecules should be comparable in size to the nucleobases and compatible with electronics.

3.1.1 Diamondoids

Candidates for this purpose are diamondoids [38]. These are tiny hydrogen-terminated diamond cage-like structures, which have shown strong potential for nanotechnological [40, 48] and pharmaceutical applications [52, 78, 79]. Some of the derivatives of the lower diamondoid, adamantane, such as amantadine, memantine, and rimantadine [80],

have found applications as anti-viral [81] and anti-Parkinsons agents [82]. Studies have shown that the amine substituted lower diamondoids develop good conductance properties depending on their relative orientation between two electrodes [83] and have good electron emission properties [42, 49, 84, 85]. Thiol groups have also been proposed to be very good candidates for functionalizing diamondoids, in order to attach them to nanoscale devices [46, 86].

The goal of our work is to exploit the hydrogen bonding possibility of diamondoids with nucleobases, as well as the semiconducting properties of the diamondoid-nucleobase complex along the hydrogen bonded orientations to enhance future tunneling current measurements for sensing DNA. As a first step in studying the feasibility for a diamondoid to sense DNA, we seek the bonding characteristics of a diamondoid placed close to a DNA nucleobase and investigate the strength of the resulting hydrogen bond, as well as its dependence on the relative distance and orientation of the two molecules. The choice of a diamondoid as a probe for sensing DNA is based on the variability in sizes and the various modification possibilities it offers [40, 87], as well as the ease in chemically attaching these onto the edge of nanopore, an issue we will discuss again in the Conclusion Section.

3.2 Computational Details

We perform computer simulations for different diamondoid-DNA nucleobase complexes. In this way, we probe the binding characteristics of these two entities, the diamondoid and the nucleobase. Bonding of a diamondoid to all four nucleobases, adenine (A), thymine (T), cytosine (C), and guanine (G) is studied. In order to promote bonding we choose derivatives of the smallest diamondoid, adamantane [80]. We begin with three derivatives of adamantane, amantadine (”ama”), memantine (”mem”), and rimantadine (”rim”). The first two have one of their sites substituted by an amine group, while the third one has one of its sites substituted by an ethanamine group. These are all sketched in Table 3.1. The reason for these choices is first computational efficiency and second that we would like to probe the biosensing possibilities of a small molecule relative in size with the DNA nucleobases. We next combine each of the three diamondoid derivatives with one of the four nucleobases. All the possible conformations for interaction are chosen in a way that the amine group of the diamondoid acts as a hydrogen bond acceptor for the nucleobases. Here, we scan a finite part of the conformational space of these two entities, as it is not possible to include the whole conformational space in our

quantum mechanical calculations. Our aim though is to present a proof of principles regarding the binding possibilities of diamondoids and DNA nucleobases and not to provide a thorough scan of their different conformations.

Table 3.1: Amine-derivatives of adamantane

memantine	amantadine	rimantadine
$C_{12}H_{21}N$	$C_{10}H_{17}N$	$C_{12}H_{21}N$
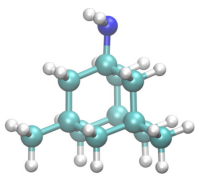	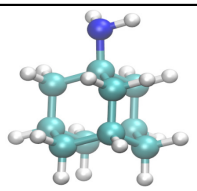	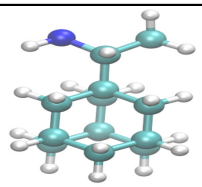

Our calculations are based on density functional theory (DFT) and have been performed using the code SIESTA [88]. We use norm-conserving Troullier-Martin pseudopotentials [89] and a split valence triple zeta polarized basis set [66]. A mesh cutoff parameter (which corresponds to the fineness of the real space grid) of 250 Ry has been found to be optimal for the calculations. We have been using the exchange-correlation functional VDW-DF2 [3] which has the form:

$$E_{xc}[\rho(r)] = E_x^{GGA}[\rho(r)] + E_c^{LDA}[\rho(r)] + E_c^{nl}[\rho(r)], \tag{3.1}$$

$$E_c^{nl}[\rho(r)] = \int d^3r \int d^3r' \rho(r)\phi(r,r')\rho(r') \tag{3.2}$$

The Kernel ϕ is a given function of $Rf(r)$ and $Rf(r')$ where $R = |r - r'|$ and $f(r)$ is a function of $\rho(r)$ and its gradient. The Exchange part is described by $PW86R$ semi-local exchange functional. Due to the explicit inclusion of a strictly non local correlation term ($E_c^{nl}[\rho(r)]$), this functional is found to describe dispersion interactions with improved accuracy in comparison to a semi-local generalized-gradient-approximation (GGA) functional [90]. The pseudopotentials, the basis set, and the VDW-DF2 functional were benchmarked with respect to the geometry and binding energy of Adenine-Thymine Watson-Crick base pairs [91]. The geometry optimization was performed using the conjugate gradient algorithm and the structure was relaxed until the forces acting on the atoms where lower than 0.04 eV/Å. The benchmarking results where in excellent agreement with previous calculations [92]. The interaction energy is calculated as the

difference between the total energy of the geometry-optimized hydrogen bonded complex with that of isolated monomers in the gas phase. The results have been corrected for the basis set superposition error (BSSE) [67] without a geometry distortion correction. This choice was based on the comparison of our results to those of known nucleobase complexes in the literature [91,92].

3.3 Results and Discussion

We next present the main outcome of our investigation and begin our analysis by investigating the strength of the hydrogen bond. We should first note that for all the diamondoid-nucleobase complexes we have studied, there is at least one non-negligible hydrogen bond that forms and connects the two components, diamondoid and nucleobase.

3.3.1 Association Energy

The association energy for individual hydrogen bonded complexes is summarized in Table 3.2. The association energy is the hydrogen bond energy denoting the strength of the hydrogen bond. The association energy is defined as the total energy of the complex substracted by the total energy of the two isolated components, nucleobase and diamondoid. The total energy is the energy as obtained through the DFT calculations. The bond-length and bond-angle for the geometry optimized structure is shown in Table 3.3 with respect to the amine group hydrogen bond acceptor site of the diamondoid. The hydrogen bond-angle is usually in the range of $140 - 180$ deg.. At angles closer to planar the interaction is expected to be electrostatic. At larger angles, the interaction is dispersion driven. Note also that hydrogen bonding can be classified according to the interaction strength, i.e. association energies (E_{assoc}) as [93,94]: (i) strong [$E_{assoc} >$ 15 kcal/mol(0.65 eV)], (b) moderate [$E_{assoc} \approx$ 4-15 kcal/mol(0.17-0.65 eV)], and weak [$E_{assoc} <$ 4 kcal/mol(0.17 eV)].

Inspection of Table 3.2, clearly reveals that all the hydrogen bonds of the diamondoid-nucleobase complexes are of moderate strength and lie between $9 - 12$ (0.38-0.52)kcal/mol (eV). It is also evident from Table 3.3, that for the hydrogen bonded complexes formed by memantine and amantadine the hydrogen bond-angle is closer to planar. For the complexes formed by rimantadine (except for the rimantadine-guanine complex) the bond

Table 3.2: Association energy of hydrogen-bonded complexes.

Association energy E_{assoc} [kcal/mol, (eV)]			
System	memantine	amantadine	rimantadine
adenine	$-8.978(-0.3893)$	$-9.306(-0.4035)$	$-9.298(-0.4032)$
thymine	$-10.228(-0.4435)$	$-10.198(-0.4424)$	$-9.972(-0.4324)$
guanine	$-11.711(-0.5078)$	$-11.719(-0.5082)$	$-10.290(-0.4462)$
cytosine	$-12.122(-0.5250)$	$-11.609(-0.5034)$	$-11.328(-0.4912)$

angle is lower in comparison to the other complexes. We base this difference on the fact that the hydrogen atoms in the amine group of rimantadine need to rearrange, so that the amine group can act as a hydrogen bond acceptor. On the other hand, a minimal rearrangement is required in the case of the amantadine and memantadine complexes. As can be inspected from Fig. 3.1 for the chosen initial configuration of these complexes, the amine group readily accepts the hydrogen from the donor site of the adjacent nucleobase resulting in angles close to planar. Note, that in all cases the hydrogen bond-lengths are in the range of $\approx 3.0 - 3.2$ Å.

Table 3.3: Bond-length (donor-acceptor distance in Å) and bond-angle (donor-hydrogen-acceptor angle in degrees) of the hydrogen-bonded complexes.

bond-length(bond-angle) Å(deg.)			
System	memantine	amantadine	rimantadine
adenine	3.080(169.6)	3.106(174.4)	2.996(147.8)
thymine	3.122(171.4)	2.993(174.23)	2.918(152.5)
guanine	3.190(175.6)	3.171(169.6)	3.200(169.7)
cytosine	3.061(179.2)	3.06(178.4)	3.071(146.5)

3.3.2 Orientation and Distance Dependence

An additional important indication of the hydrogen bond strength is its deviation with respect to the diamondoid-nucleobase optimized geometry as predicted from the DFT calculations. This we define as the *optimized geometry* and serves as a reference for comparison. This reference is needed, as in real applications a nucleobase may approach the diamondoid at orientations and distances different from the ideal scenario,

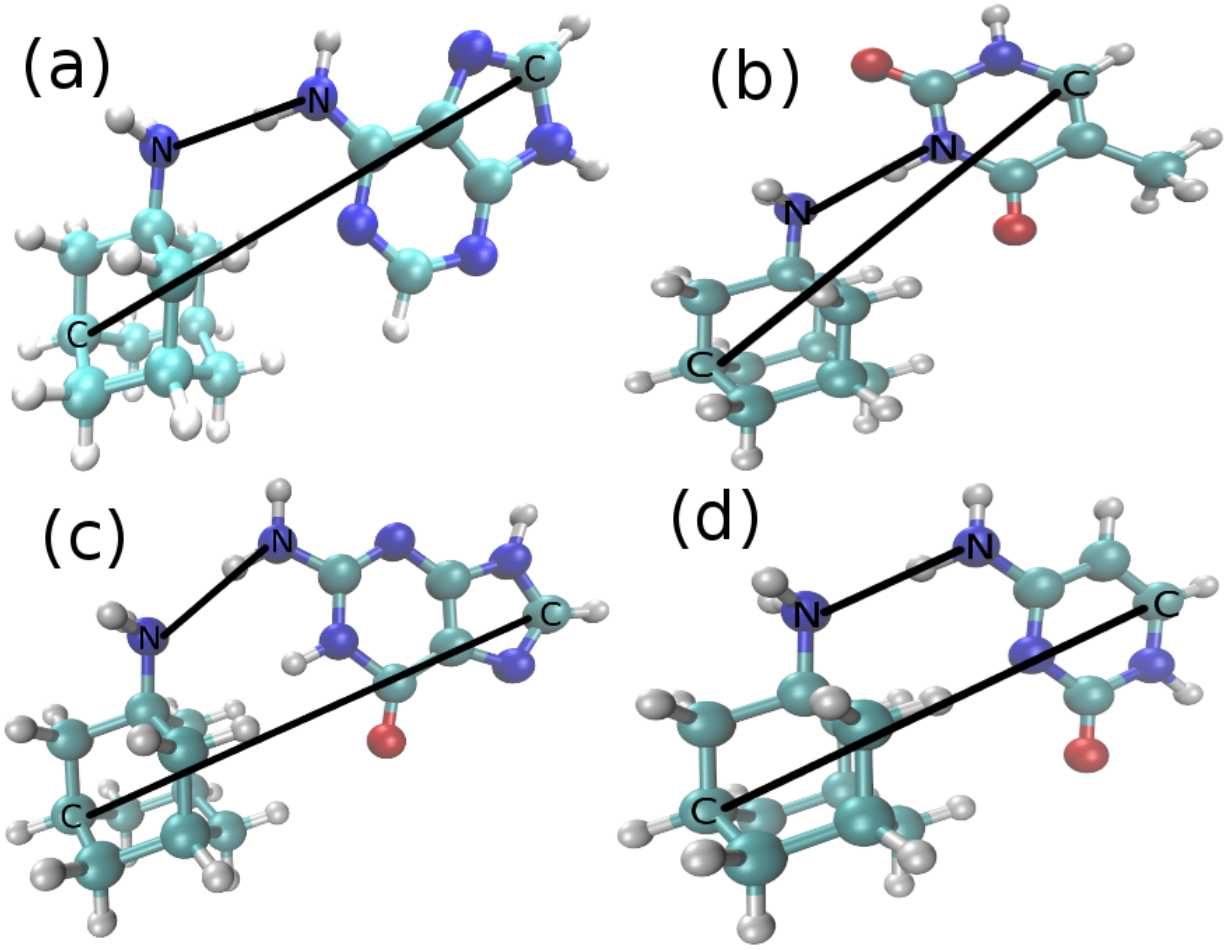

Figure 3.1: The N–N donor acceptor axis denotes the axis along which the geometry optimization was done. The C–C axis denotes the propeller angle rotation axis (see text for definitions). The conformations correspond to the initial configurations chosen for our simulations for the (a) ama-A, (b) ama-T, (c) ama-G, and (d) ama-C complexes, respectively.

which is studied using the DFT optimized geometry. In the following, we will characterize the distance and orientation dependence of the hydrogen bond for all diamondoid-nucleobase complexes. For this we present our results with respect to the distance between the amine group hydrogen-bond donor of the diamondoid to the acceptor group of the nucleobase (the distance is defined between the two N atoms involved in this bond). The N–N donor-acceptor axis denotes the axis along which the geometry optimization was done. We also define a propeller angle for the relative orientation of the diamondoid with respect to the nucleobase. The propeller angle rotation axis is defined by two carbon atoms. The one is the carbon atom on the nucleobase site which defines one end of the propeller axis and has been chosen according to similar studies found in the literature [92]. The second C atom on the diamondoid end has been chosen to

belong to the rigid cage structure of diamondoid. It is the site of the diamondoid which is in plane with the nucleobase and can be directly or through a thiol group be attached on a surface of a biosensing device. The N–N and propeller (C–C) axes about which the nucleobase was rotated with respect to a fixed diamondoid can be seen in Fig. 3.1 for the amantadine-nucleobase complexes. These axes are exactly equivalent for the complexes formed by the other two diamondoids.

We begin with an optimized geometry as a reference for which the propeller angle is defined as 0 degrees. We then vary the distance between the two units of the complex, the diamondoid and the nucleobase, and summarize the results in Fig. 3.2. This figure shows the variation of the association energy (E_{assoc}) with respect to this distance for all complexes studied in this work. It is obvious that all energies lie in the same moderate range as mentioned previously for the optimized cases (see Table 3.2). For the same nucleobase the association energy minimum corresponds to the same distance. This does not hold only for the case of the memantine-T complex for which the minimum is shifted towards higher distances compared to the other T-complexes. A further analysis of this result has been done in one of the following section in which the frontier orbitals of the complexes are analyzed.

We next take as the reference the optimized complexes, i.e. the ones who correspond to the association energy minima in Fig. 3.2 in order to unveil the rotational dependence of the hydrogen bonding in the diamondoid-nucleobase complexes. This dependence is studied by rotating the nucleobase along the C–C axis shown in Fig. 3.1. The results can be reviewed in Fig. 3.3 for all diamondoid-nucleobase complexes studied here. In this graph, the deformation energy is shown, i.e. the energy difference between the complex in which the nucleobase has been rotated and the optimized reference structure of the same complex. It is clearly evident that when the donor group of the nucleobase approaches the amine acceptor group of the diamondoid at larger angles the dispersion forces increase, thus the interaction and the deformation energy increases. An exception was found in the case of the ama-T complex in which the interaction remains strong, i.e. the deformation energy goes to zero even at large negative propeller angles. This is justified by the observation that for all negative propeller angles, a very small deviation in the donor-hydrogen-acceptor angle was observed. Note, that for positive propeller angles, the deformation energy again increases as in all other complexes. For these angles, a change in the donor-hydrogen-acceptor angle is now evident. One interesting observation is that for the cytosine interaction with memantine, at larger angles, the interaction becomes weak (the deformation energy increases) with respect to that of the geometry optimized hydrogen bonded reference structure. In this case, as the absolute value of the

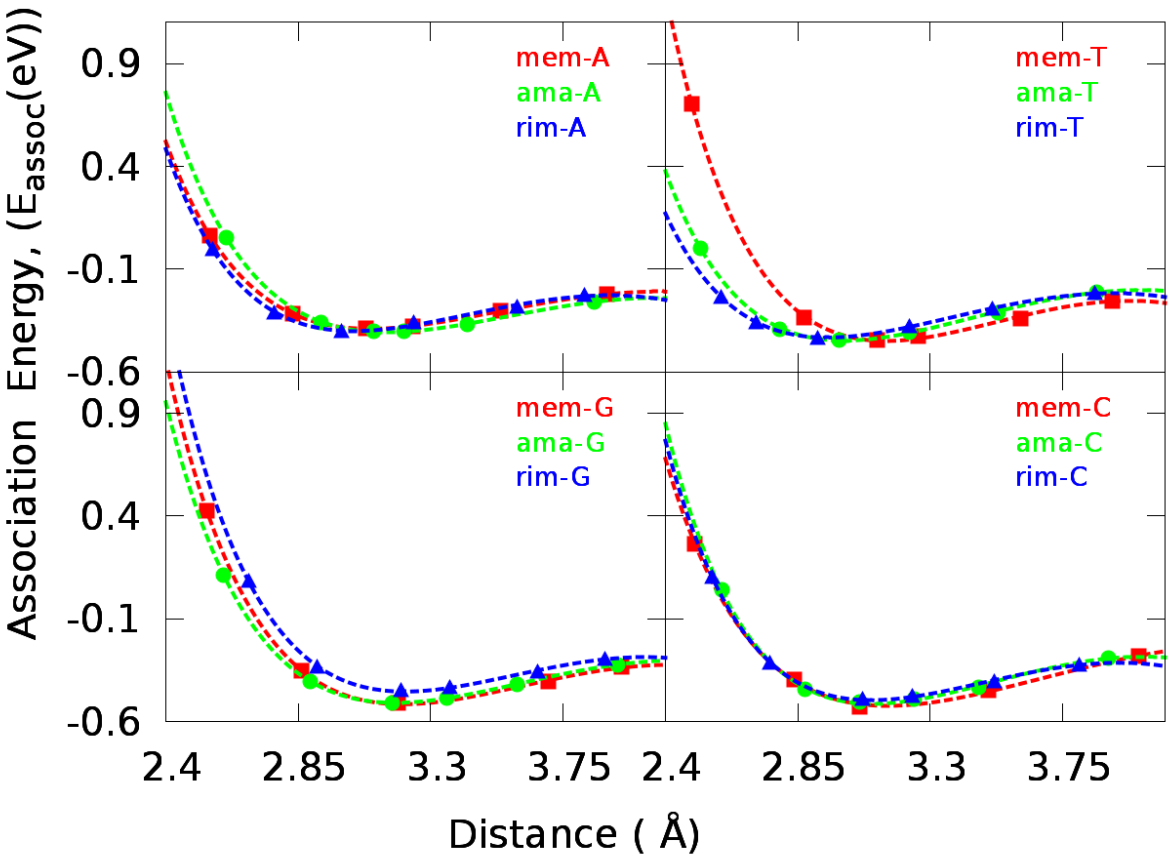

Figure 3.2: Association energy (E_{assoc}) as a function of the diamondoid-nucleobase distance.

propeller angles increase, the conformation of the complex deviates significantly from the reference, i.e. the conformation of stronger coupling between memantine and cytosine. For all other cases, the interaction is found to be moderate again with respect to the reference structure.

A comparison of all complexes reveals that the deviation from the optimized reference geometry is non-monotonic. This behavior is based on the fact that the rotation along the C–C axis in each complex is not symmetric for positive and negative propeller angles. This occurs mainly because the hydrogen bond angles (shown in Table 3.3) are non planar. Two exceptions occur for the mem-C and ama-C cases, which are almost symmetric, as the hydrogen bond angles of their reference conformations are almost planar. Overall, no conclusion can be drawn whether this deviation is stronger for one of the diamondoids in any complex. This is again evident from Fig. 3.3 where the energy for the mem-A complex shows a smaller increase compared to the mem-G case, which probably

reflects larger deviations from the reference structure for larger angles for the latter case. The behavior of the other complexes is similar. Note, that we have focused on the one strong/moderate hydrogen bond that occurs between a diamondoid and a nucleobase, for which the characteristics are given Table 3.3. This hydrogen bond is expected to lead to enhanced nucleobase-specific tunneling currents in a sensing device. Nevertheless, more than one weak hydrogen bonds have also been observed in all complexes, but for these both the hydrogen bond and hydrogen bond angle are large enough, decreasing significantly the association energy. Hence, the lifetime of these weak hydrogen bonds is expected to be very short to be used in sensing the bases, and are thus not of high interest in this work.

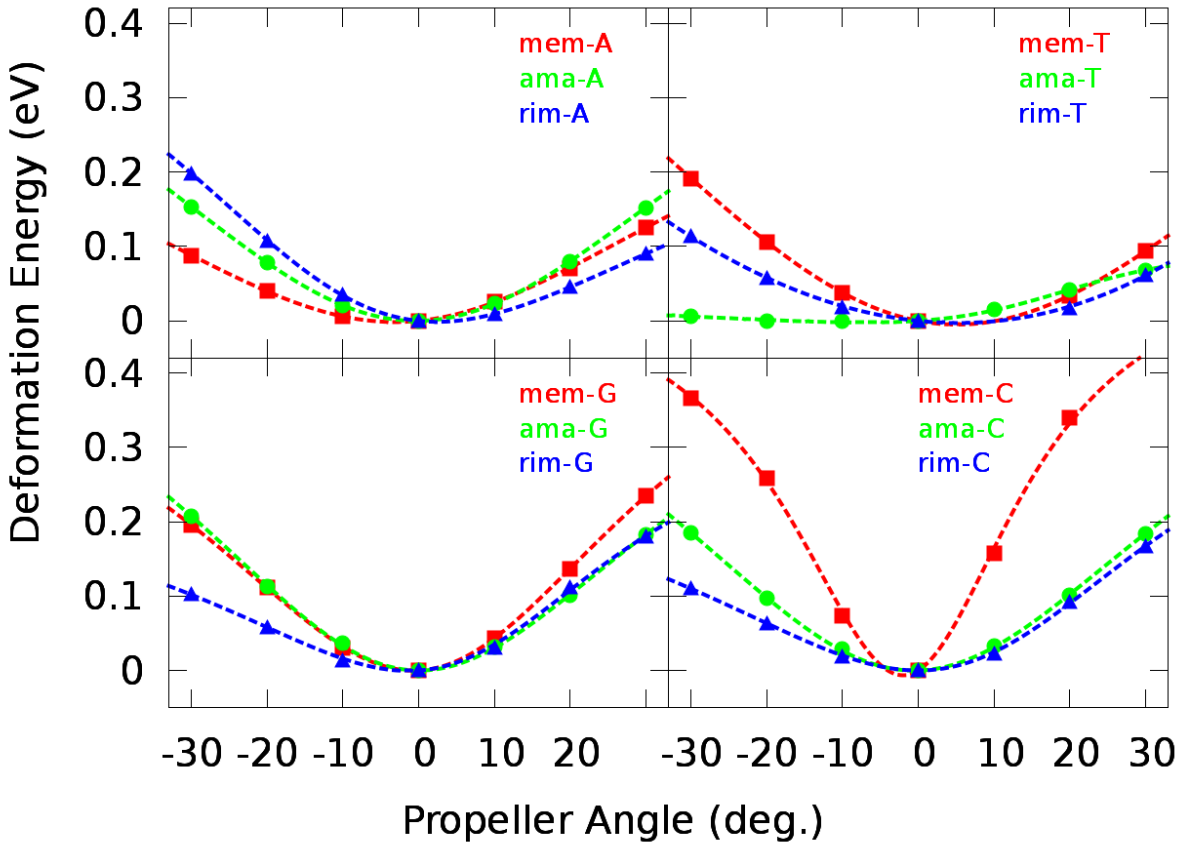

Figure 3.3: Deformation energy as a function of the propeller angle with respect to the optimized geometry corresponding to the minimum for each diamondoid-nucleobase complex in Fig. 3.2.

3.3.3 Frontier Orbitals and Electronic Structure

At a final step, the electronic properties of the nucleobase-diamondoid complexes are analyzed. We focus on their frontier orbitals - the highest occupied and lowest unoccupied molecular orbitals, HOMO and LUMO, respectively - as well as their electronic structure as probed through the electronic density of states (eDOS) and the electronic band-gap. We next always refer to the geometry optimized structure of each diamondoid-nucleobase complex. We begin with the analysis on the frontier orbitals and show these for the hydrogen bonded structure of amantadine with all nucleobases in Fig. 3.4. For all ama-nucleobase complexes both the HOMO and LUMO states are located at the nucleobase site. The HOMO and LUMO orbitals of the complex are associated with the nucleobase only. For comparison, the HOMO and LUMO orbitals for isolated adenine and amantadine molecules are shown in Fig. 3.5b and 3.5c respectively. Comparing the lower panels in this figure with panel (a) from Fig. 3.4 reveals that the HOMO, LUMO orbitals of adenine not only dominate in the complex, but are also not altered by the presence of the adjacent adamantane. The HOMO, LUMO states of the isolated adenine are indeed those that correspond to the HOMO and LUMO states of the ama-A complex, respectively.

Similar are the features for some of the mem- and rim- hydrogen-bonded complexes, shown in Fig. 3.6 and Fig. 3.7, respectively. The HOMO and LUMO states of the complexes correspond to the HOMO and LUMO states of the nucleobase for the mem-A, mem-G, and rim-G cases. We find a deviation from this observation for the other memantadine and rimantadine complexes, namely rim-A, rim-T, mem-T, rim-C, and mem-C. In these cases, the diamondoid is also associated with the HOMO state of the complex. In the first three cases (i.e. rim-A, rim-T, and mem-T), two are the factors that stabilize the complex, the repulsion between the HOMO state of the nucleobase and that of the diamondoid, as well as the attraction of the LUMO state of the nucleobase with the HOMO state associated with the amine group site of the diamondoid. In the previous section it was observed that the mem-T complex has its energy minima shifted towards higher distances compared to other diamondoid-T complexes. The origin of this comes from a possible compromise between the attractive and repulsive interaction of the frontier orbitals, as well as the fact that the donor-hydrogen-acceptor angles for mem-T are close to planar in comparison to rim-T. Accordingly, the repulsion of the frontier orbitals is reduced by increasing the distance. In the last two cases (i.e. rim-C and mem-C), the HOMO state of the complex is associated solely with that of the diamondoid, while the LUMO state originates only from the nucleobase resulting in

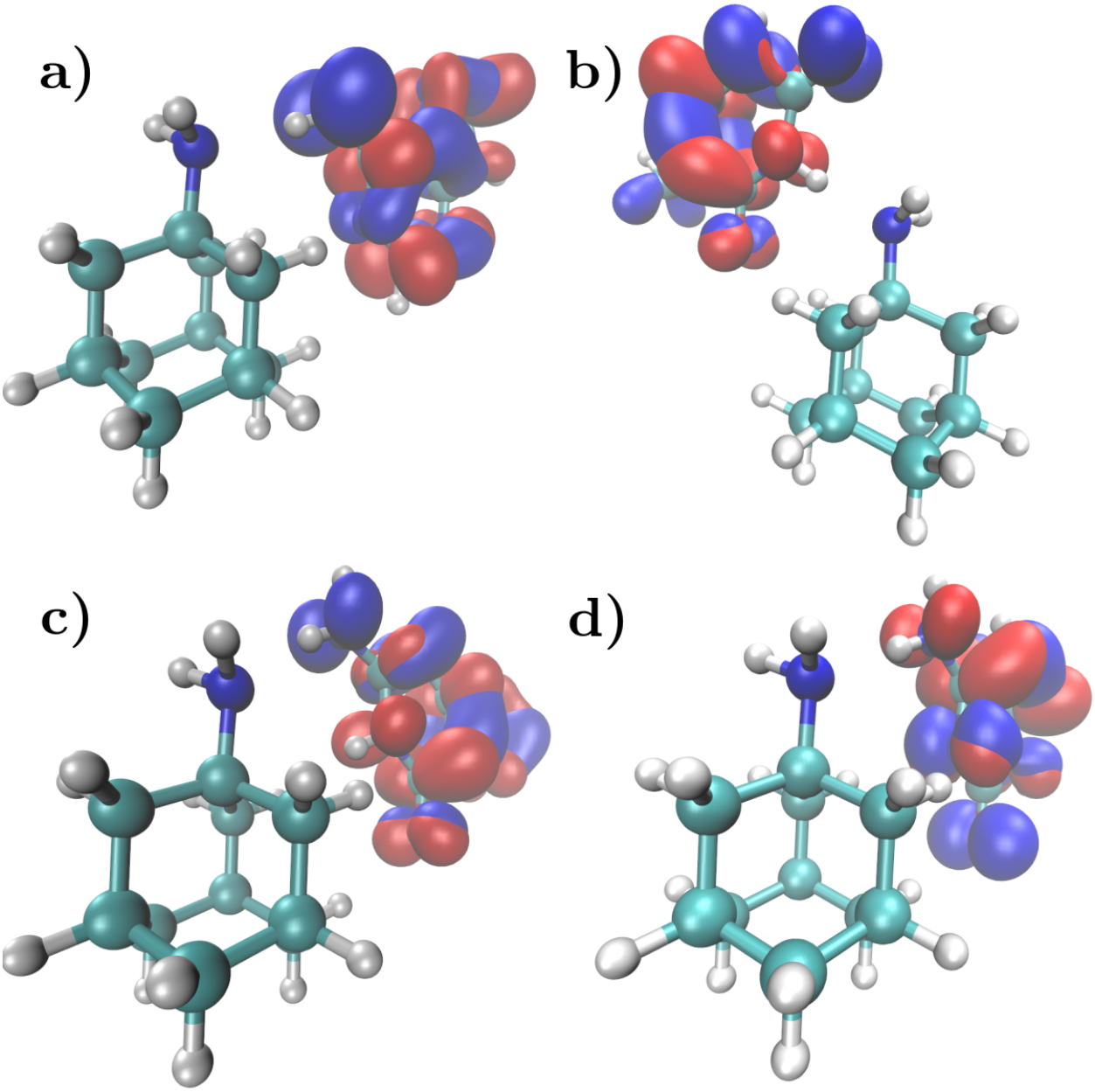

Figure 3.4: The frontier orbitals, HOMO (blue) and LUMO (red), for the four hydrogen bonded amantadine-nucleobase complexes: (a) ama-A, (b) ama-T, (c) ama-G, and (d) ama-C.

hydrogen-bonded complexes which are stabilized by the attraction of these two states. Note, that diamondoid levels which usually populate the HOMO are driven down in about two third of the complexes studied here, and the HOMO and LUMO levels in those cases are solely located on the nucleobase. A possible explanation of this could be a charge transfer between the diamondoid and the nucleobase, which shifts the diamondoid HOMO levels towards lower energies. An additional study to shed more light into this issue is further planned.

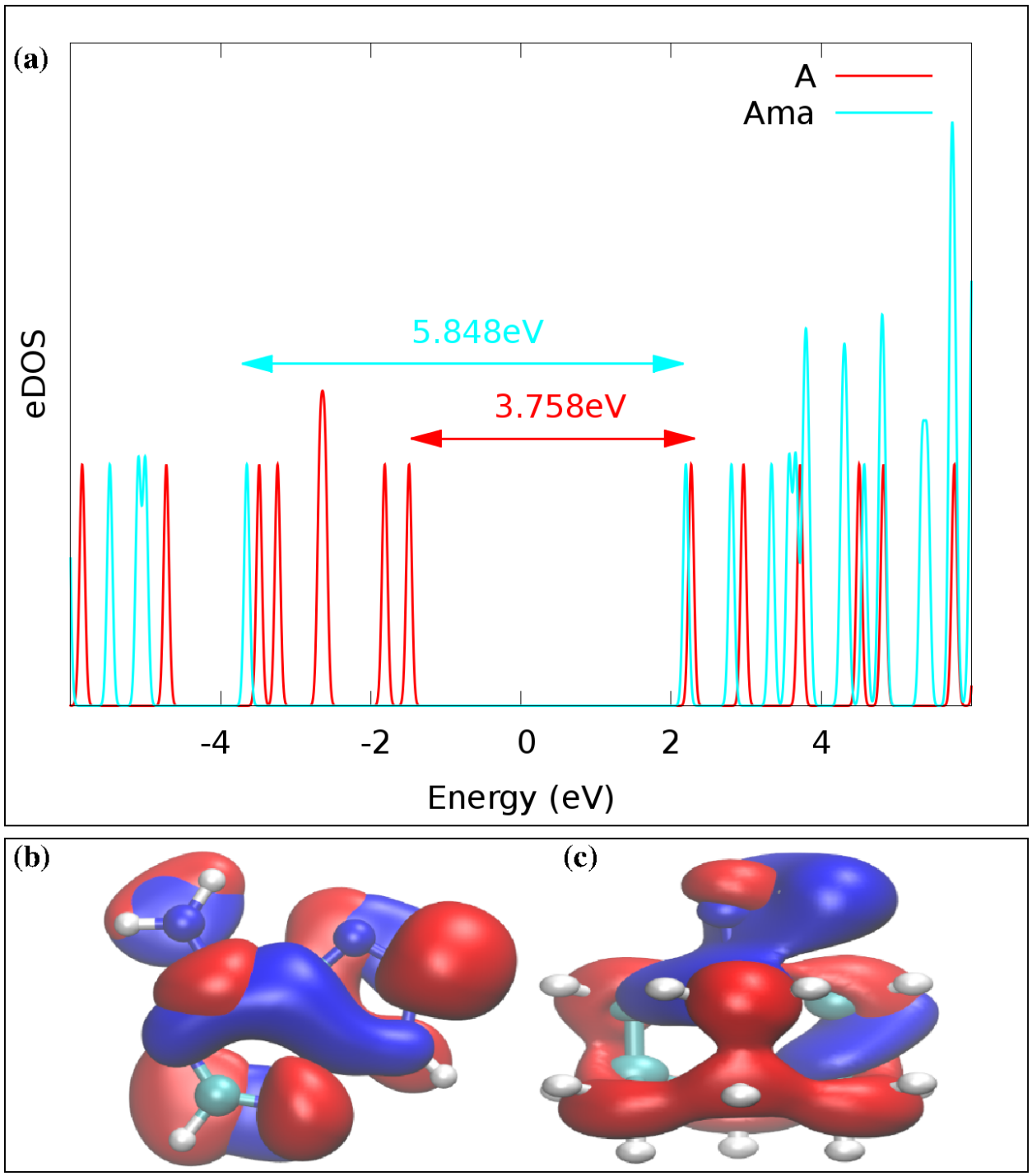

Figure 3.5: a) Electronic density of states of an isolated amantadine and an isolated adenine. b) Frontier orbitals . The HOMO orbitals are sketched in blue and the LUMO in red.

In order to understand this and also provide an insight on possible conductance measurements along these complexes, we turn to the electronic density of states (eDOS) of the complexes. These are summarized in Figs. 3.8, 3.9, 3.10, for the ama-, mem-, and rim-

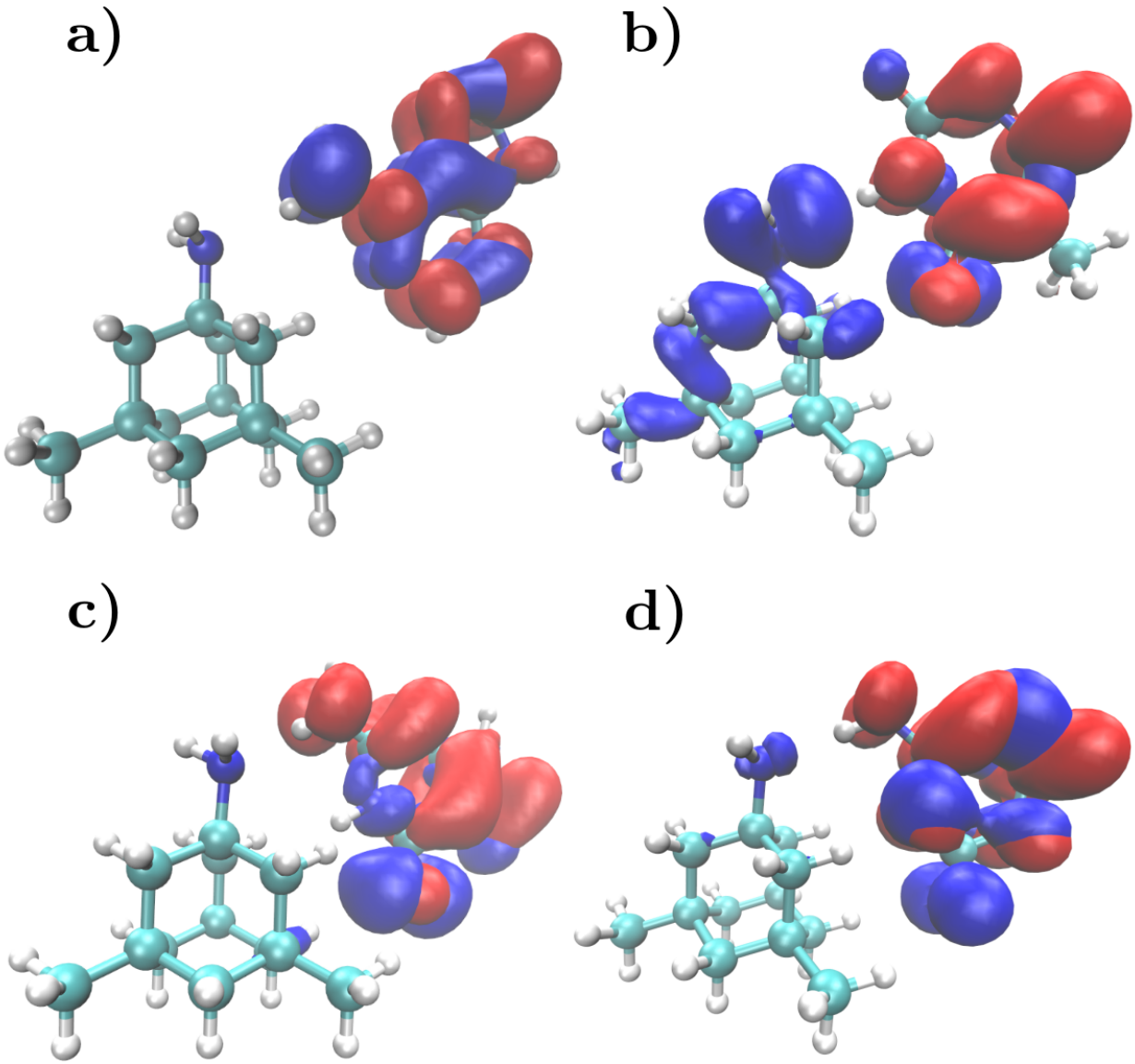

Figure 3.6: The frontier orbitals, HOMO (blue) and LUMO (red), for the four hydrogen bonded memantine-nucleobase complexes: (a) mem-A, (b) mem-T, (c) mem-G, and (d) mem-C.

nucleobase complexes, respectively. The eDOS for the isolated nucleobases and isolated diamondoids are also given in each panel for comparison. The numbers on the graphs denote the electronic band-gaps of the complexes and isolated nucleobases. The eDOS are shifted with respect to the LUMO state of the isolated diamondoid in each case. This choice was made because the isolated diamondoid is assumed to be the reference for evaluating the electronic properties of the complexes. In a potential biosensing device,

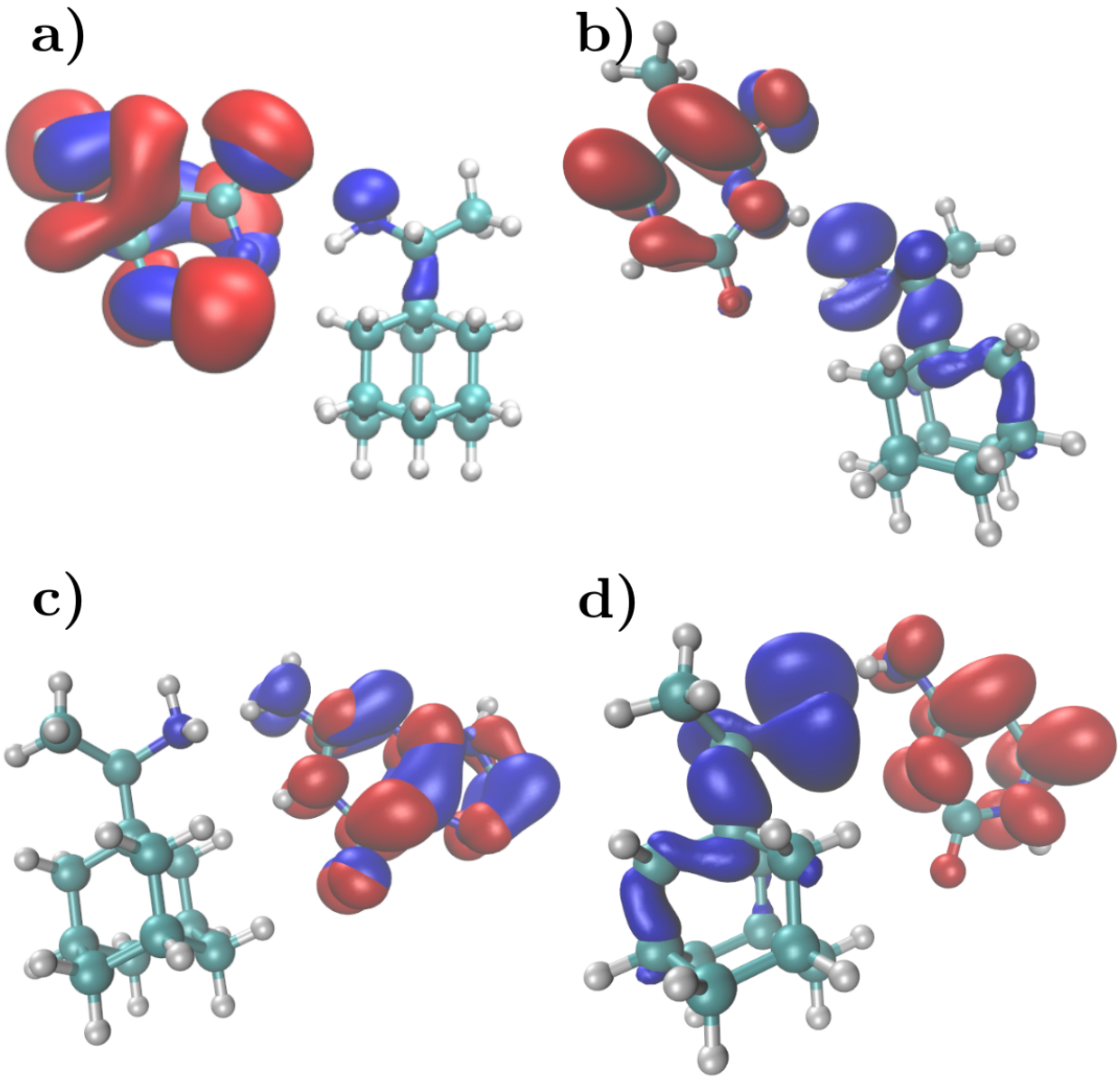

Figure 3.7: The frontier orbitals, HOMO (blue) and LUMO (red), for the four hydrogen bonded rimantadine-nucleobase complexes: (a) rim-A, (b) rim-T, (c) rim-G, and (d) rim-C.

the diamondoid will be the sensing probe. It should be underlined, that we are aware of the problem of DFT in calculating correct electronic band gaps. Here, though, we do not care about absolute numbers, but rather aim in comparing the band-gaps for the different complexes and the isolated diamondoids studied. The electronic band-gaps we have obtained for the isolated diamondoids from our computations are 5.848 eV, 5.829 eV, and 5.719 eV, for amantadine, memantine, and rimantadine, respectively.

Inspection of the eDOS reveals, that in all complexes a part of the band gap region of

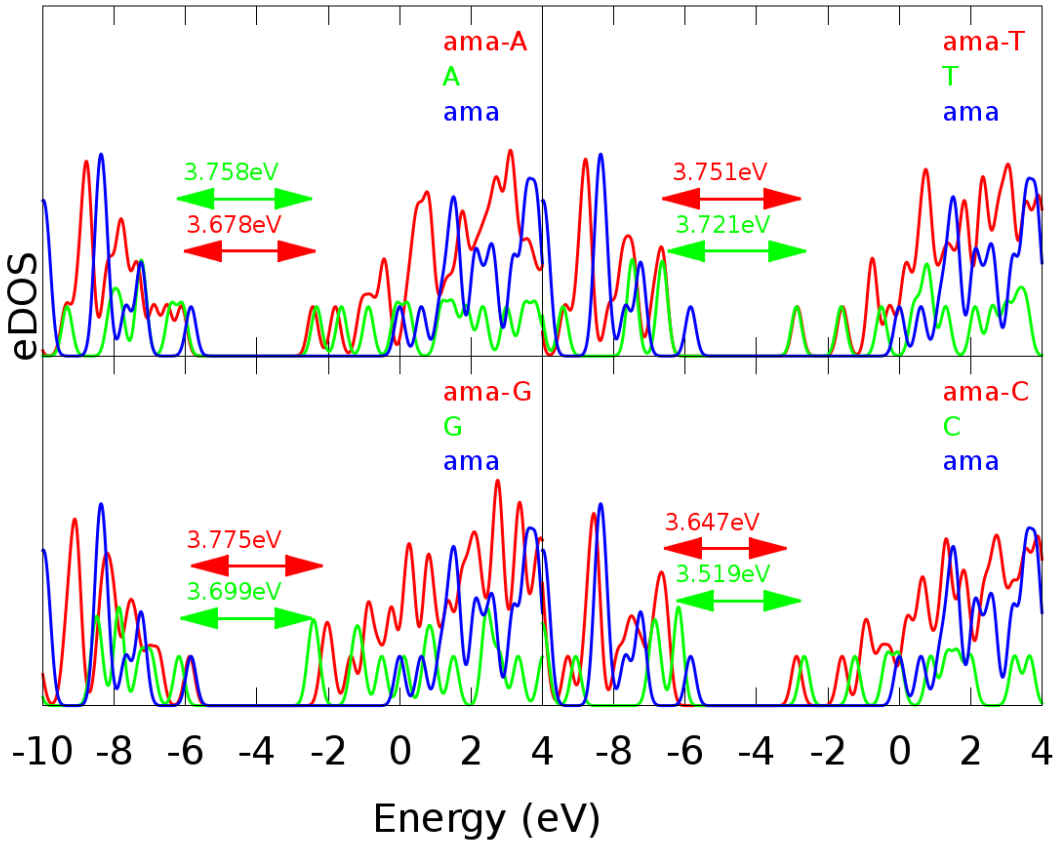

Figure 3.8: The electronic density of states (eDOS) and band gap for the amantadine-nucleobases complexes: (a) ama-A, (b) ama-T, (c) ama-G, and (d) ama-C. The eDOS in all cases are shifted with respect to the LUMO state of amantadine which is placed at 0 eV.

the isolated diamondoids is filled by the states of the nucleobases. As a general remark, the band-gaps of the hydrogen bonded complex are in comparable range to that of the isolated nucleobases. For all the diamondoid-A complexes the band-gap difference between the complex and the bare nucleobase (Fig. 3.11) is about 0.08-0.1 eV, for the diamondoid-T complexes it is 0.03-0.06 eV, and for the diamondoid-G it is 0.06-0.09 eV. We see a large difference between the two diamondoid-C complexes the band-gap differences mentioned above are about 0.12-0.13 eV, but for rim-C this difference rises to 0.36 eV. Similarly the corresponding band gap differences for the rim-T case are about 0.03-0.04 eV larger than in the ama-T and mem-T cases.

The first important implication of these results with respect to biosensing abilities of small modified diamondoids is that rimantadine can be used to clearly distinguish

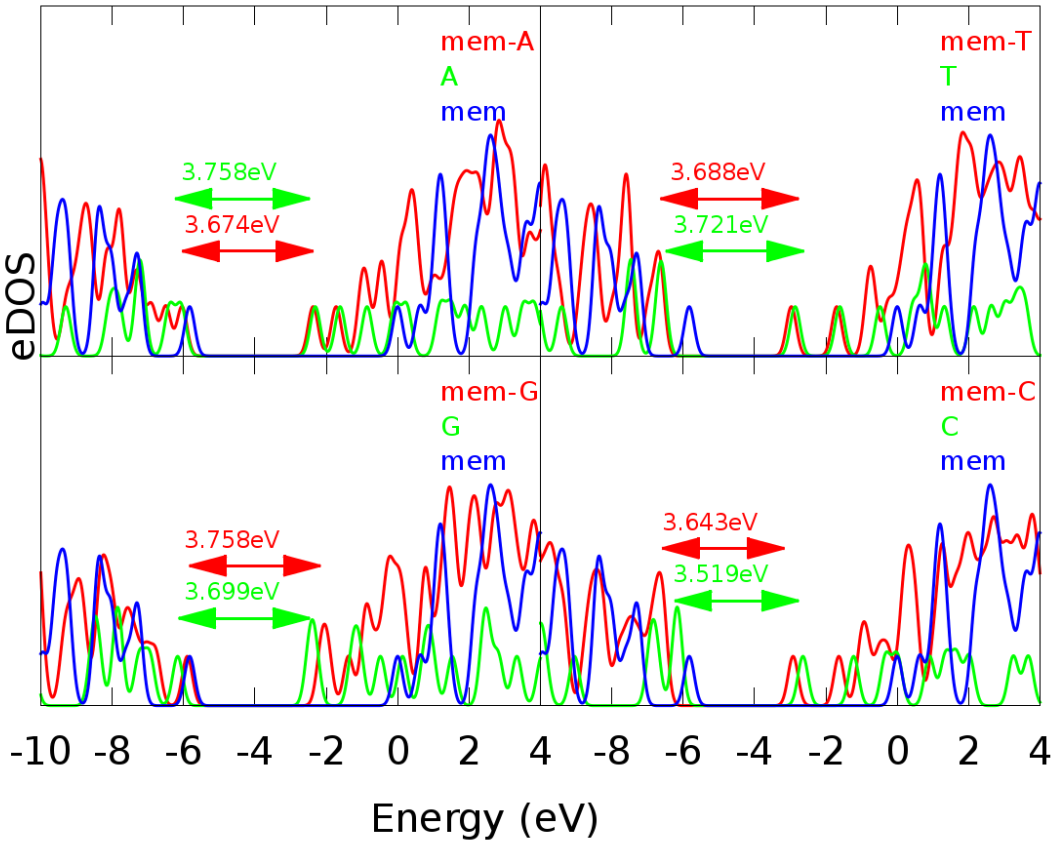

Figure 3.9: The electronic density of states (eDOS) and band gap for the four hydrogen bonded memantine-nucleobase complexes: (a) mem-A, (b) mem-T, (c) mem-G, and (d) mem-C. The eDOS in all cases are shifted with respect to the LUMO state of memantine which is placed at 0 eV.

cytosine among all the other nucleobases, and possibly also thymine. Differences in the band-gaps could imply that variations in the transport properties along different diamondoid-nucleobase complexes can potentially also be observed. According to the eDOS data we present here, for a specific diamondoid, the band-gap differences of the complex and the isolated nucleobase are small, but do differ. For example, these differences are 0.08 eV for ama-A, 0.03 eV for ama-T, 0.77 eV for ama-G, and 0.14 eV for ama-C, and are non-negligible. Taking the isolated diamondoids as references will lead to the following band-gap differences between the isolated diamondoids and the A-complexes. These will be 2.09 eV, 2.06 eV, and 1.96 eV for the ama-A, mem-A, and rim-A cases respectively. The respective differences between the band-gaps for isolated diamondoids and the ama-T, mem-T, and rim-T complexes are 2.13 eV, 2.10 eV, and 2.0 eV. Some of

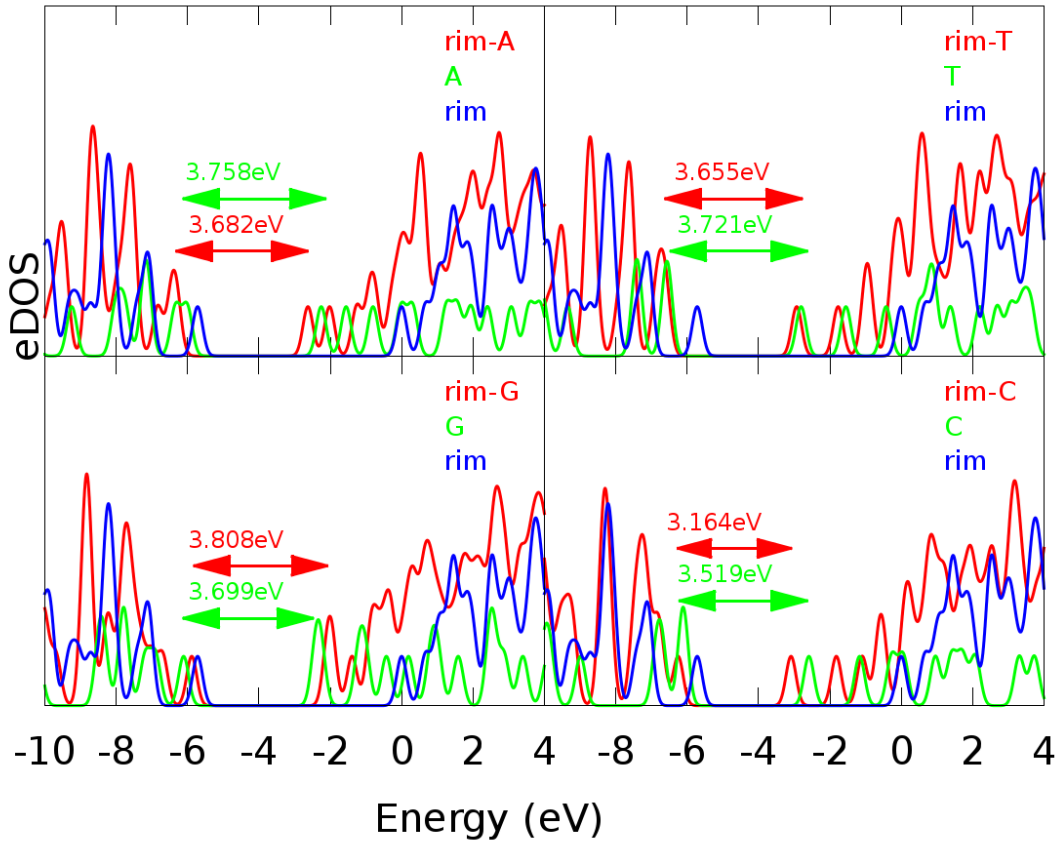

Figure 3.10: The electronic density of states (eDOS) and band gap for the four hydrogen bonded rimantadine-nucleobase complexes: (a) rim-A, (b) rim-T, (c) rim-G, and (d) rim-C. The eDOS in all cases are shifted with respect to the LUMO state of rimantadine which is placed at 0 eV.

these differences are within the error, but differences do exist. We should note here, that in a biosensing device, either it is a nanopore or a surface on which a diamondoid is attached and should sense DNA molecules, a salt solution will be present. In this respect, the presence of other species would decrease the signal-to-noise ratio of the device making the energy differences given above smaller. As a possible solution which we propose and are currently investigating are ways to further enhance the differences in the electronic properties (and as a consequence in their transport properties) of the different complexes by chemically modifying the diamondoids.

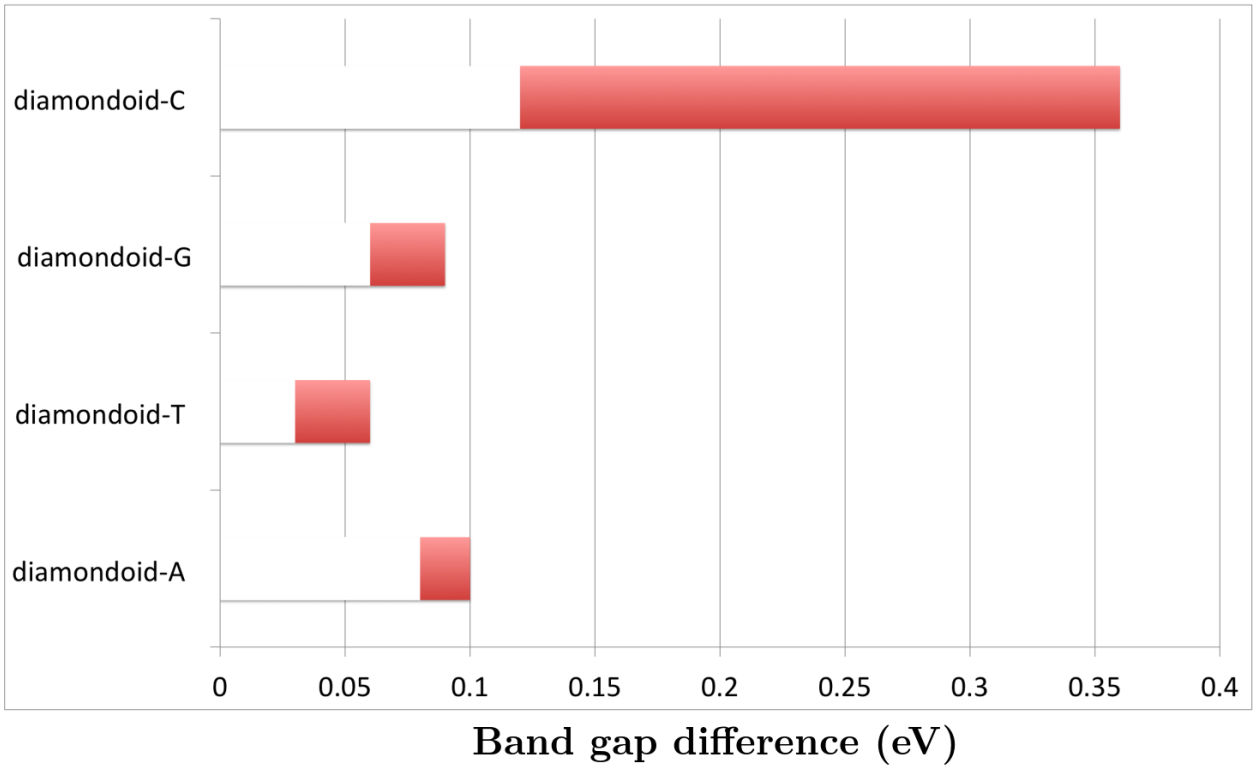

Figure 3.11: The band-gap difference between the complex and the bare nucleobase

3.3.4 Mutated Nucleobase and Epigenetic Marker

It is very critical for a DNA sequencing technique to detect mutations [95] and epigenetic markers [36]. Keeping this in mind, one would like to qualitatively understand if a diamondoid functionalised nanopore would be able to distinguish between a mutated group and a natural nucleobase. The differences in the electronic structure of these molecules results in a distinguishable electronic tunnelling current [36]. We have tried to understand the electronic properties of rimantadine interacting with mutations of nucleobases and compare then with results presented in the previous sections. The mutant groups used in this study are the following and can be seen in table 3.4.

- 5-methyl-cytosine [96] which is an epigenetic marker
- 8-oxoguanine [97] which is a mutation of guanine

The electronic denisty of states (eDOS) for the rimantadine-mutant and rimantadine-nucleobase complex has been shown in figure 3.13 and figure. 3.7 respectively. By comparing the HOMO-LUMO gap from these figures, the following observation follows:

Table 3.4: Mutants of nucleobases

8-oxoguanine	5-methyl-cytosine
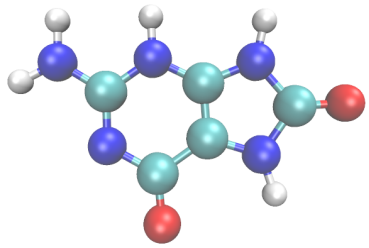	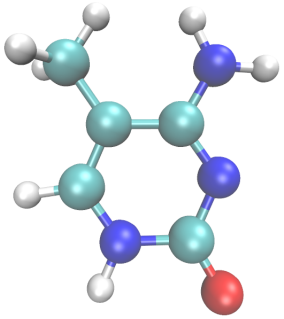
8-OG	5-mC

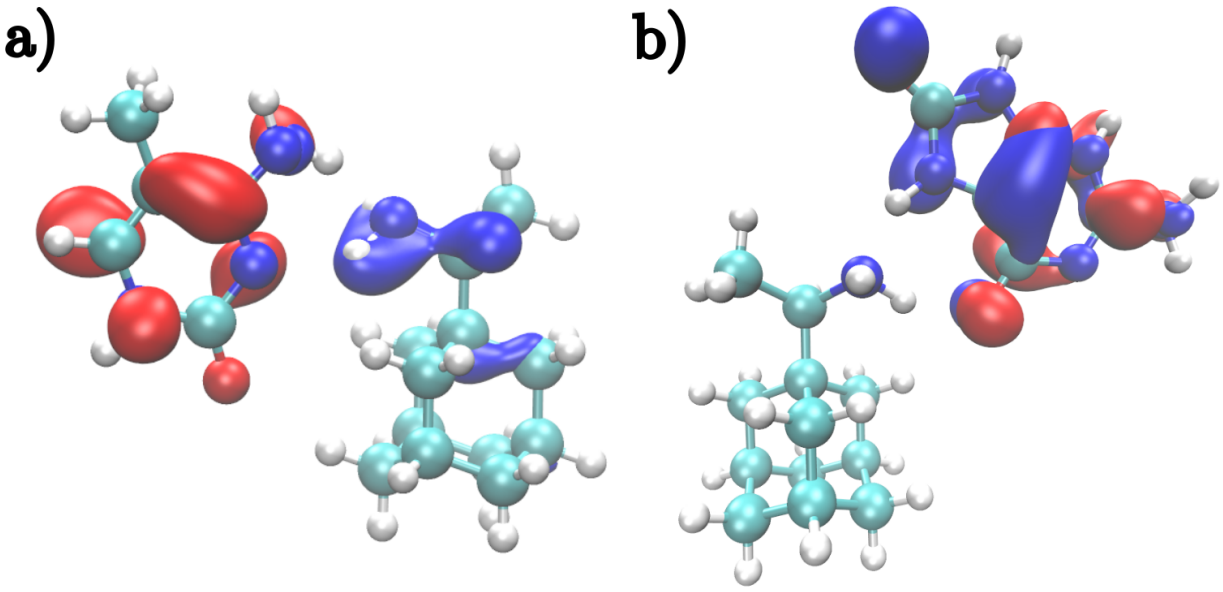

Figure 3.12: The frontier orbitals, HOMO (blue) and LUMO (red), for a)rimantadine-5-methyl-cytosine complex, and b) rimantadine-8-oxoguanine complex

- The HOMO-LUMO gap for rim-C and rim-5-mC are 3.164eV and 3.258eV respectively.
  - The difference of band gap between the rim-C and rim-5-mC is 0.094 **eV** .
- Similarly the HOMO-LUMO gap for rim-G and rim-8-OG are 3.808eV and 3.238eV.
  - The difference of band gap between the rim-G and rim-8-OG is 0.57 **eV** .

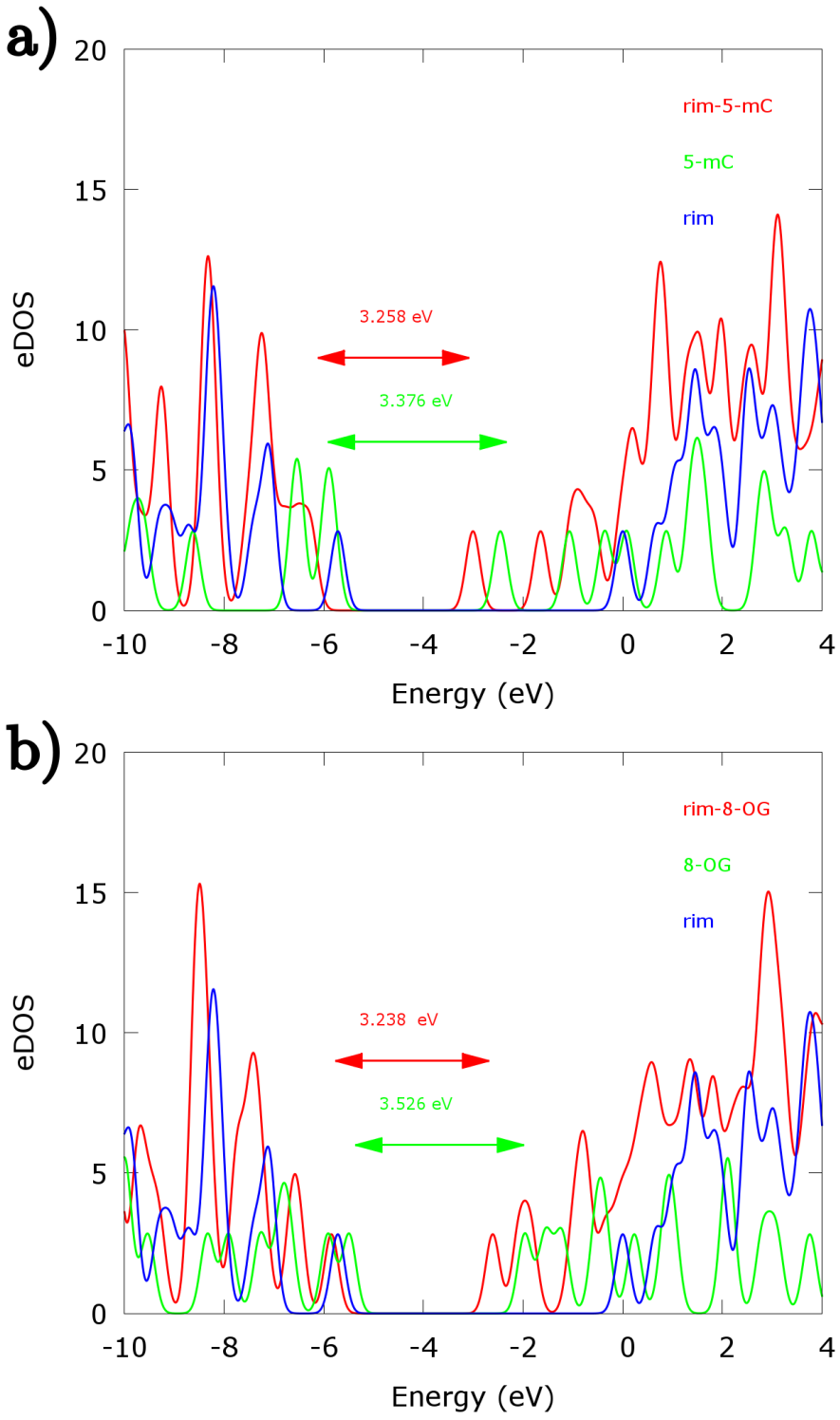

Figure 3.13: The electronic density of states (eDOS) for a)rimantadine-5-methyl-cytosine complex, and b) rimantadine-8-oxoguanine complex. The eDOS in all cases are shifted with respect to the LUMO state of rimantadine which is placed at 0 eV.

- We may qualitatively argue that in a full transport calculation, this difference may result in a distinguishable tunnelling current.

Similarly the frontier orbitals for rim-mutated nucleobase complex can be seen in figure 3.12. The rim-5-mC has been seen to be stabilised by the attraction between the HOMO of the diamondoid with the LUMO of the of the methylated cytosine (5-mC). But in the case of rim-8-OG, only the frontier orbital of the 8-oxoguanine seems to play a role in the hydrogen bonding.

3.4 Summary and Conclusions

In summary, the aim of the current work was to investigate the bonding characteristics of tiny diamond clusters, the diamondoids, with nucleobases in view of potential biosensing applications. We have found, that in all cases the diamondoids tend to form hydrogen bonds with the nucleobases. The strength of the bonds are moderate, but measurable through electronic means. The bonding of the two units depends strongly on their distance and relative orientation. We have unraveled the electronic structure of the hydrogen-bonded complex by investigating the electronic band gaps, as well as the frontier orbitals of the complexes. In most cases, the main contribution in these orbitals arises from the nucleobases, while the diamondoids either do not contribute at all or are related only to the HOMO states. The differences in the electronic band gaps between the diamondoid-nucleobase complexes and the isolated nucleobases propose ways to distinguish between the nucleobases, as we have discussed in the text. We should also note here, that a wide conformational scan will be needed to examine the variation of the electronic properties for all the different distances and orientations of the diamondoid-DNA complex. This was not possible with the computational tools available in this work. It also remains to be shown how the surrounding environment in a real biosensing device will also affect the strength of the hydrogen bonds between the diamondoid-probe and the DNA molecule.

Our results are relevant to biosensing applications. We propose a biosensing device, which consists of two electrodes that are functionalized by at least one diamondoid. Regarding this functionalization, the attachment of diamondoids on metallic surfaces has

been experimentally done before through thiol groups [42]. To our knowledge, in the case of graphene or graphene nanopores, there is no relevant study. The attachment of the diamondoid on the graphene edge should depend on the terminations on the nanopore edges. Attachment could be possible by removing at one site the terminating atom and form a strong covalent C-C bond between the graphene and the diamondoid. Another possibility would be to attach the functionalizing diamondoid directly to the terminating atom, by forming a N-H bond or a C-H bond in the case of a N-terminated or H-terminated graphene sheet, respectively. Nevertheless, the attachment of a diamondoid on graphene is not clear and would also depend on the graphene edges, whether these are zig-zag or armchair ones. This issue goes beyond the scope of the thesis, hence requires a dedicated investigation on its own.

Once the electrodes have been functionalized they are placed into a solution of biomolecules, single-stranded DNA as an example, and would potentially be able to recognize the bases using an electric field along the electrodes. A specific application we had in mind is the translocation of DNA through nanopores for ultra-fast DNA sequencing. In this case, one or additional diamondoids should functionalize the nanopore. Some of these can play the role of a *backbone-grabber* to instantly stall the biomolecule and the others play the role of the *nucleobase-reader* and sense the nucleobase [2]. These diamondoids could potentially also alternate their roles throughout the process in order to assist multiple measurements and decrease the read-out error. The choice of the size of the diamondoids will depend on the nanopore diameter. The detection will be done using transverse current measurements along the nanopore [36]. According, to the analysis we presented on the electronic band gaps of the hydrogen bonded complexes, the different complexes should give distinguishable electronic signatures. In order to realize this, transport measurements are necessary. The use of modified diamondoids might also enhance the electronic footprint of each nucleobase in the diamondoid-nucleobase hydrogen bonded complex. Finally, it also remains to be shown, how the presence of water and ions, will affect the electronic signals and could lead to strongly distinguishable nucleobases. Work along these directions of a diamondoid functionalized gold electrodes will be addressed in chapter 4.

Acknowledgment

Part of this chapter was reproduced from Refs. [98, 99] with permissions from the royal society of chemistry and europhysics letter editorial office respectively .

4 Electronic transport across diamondoid functionalised devices

Having explored the binding, and the electronic properties of the diamondoid-nucleobase complexes in chapter 3, we further investigate the use of diamondoids in functionalizing nanopores.

4.1 Introduction

Nanometer-sized pores opened in a material have shown a high potential as a cheap and ultra-fast third generation sequencing technology [1, 18, 22, 30, 36, 100]. A nanopore sequencer involves a single molecule technique. This does not require any labels or amplification. Such a device can potentially sequence almost in real time. Nanopores are of low cost and compatible with conventional electronics. They can be rendered into a parallel high-throughput device for reading-out DNA and are able to support long read lengths. Nanopores can electrophoretically translocate biomolecules (DNA, RNA, and proteins) within a salt solution, giving rise to ionic current blockades. The ionic signals can in turn be used to detect the translocation of the biopolymers [101].

Different sequencing protocols, that is ways to identify the bases along DNA have been proposed. Among these, the use of transverse current signals across nanopores shows a high promise in view of sequencing applications [1, 31]. Specifically, in a tunneling recognition scheme a voltage bias which is applied across the electrodes is able to capture the translocating single stranded DNA (ssDNA) [27, 36, 102]. It involves a solid state nanopore including break junction electrodes which can measure the transverse tunneling current, detect the difference in the electronic structure of the translocating nucleobases, and read out the genetic information (i.e. sequence the nucleobases). This

method of sensing can be very efficient, but the distinctive coupling of the different nucleotide species to the electrodes needs to be improved and a sufficient sampling in the measurement of each nucleotide located between the electrodes [5,103].

A possible improvement is to functionalize the electrodes with small molecules which can form hydrogen bond bridges with the translocating nucleotides [77]. In this way, the functionalizing molecule introduces molecular states in the electronic gap of the band structure of the electrodes across which the electrons can hop enhancing the tunneling current [2]. We have seen in chapter 3, the potential of amine-derivatives of lower diamondoids to be used as functionalization molecules in a nanogap [98,99]. Diamondoids are tiny hydrogenated diamond cages, with tunable electronic properties and a variety of potential applications [48]. The smallest diamondoids with a diameter up to a few nanometers are commonly known as 'lower diamondoids'. The hydrogen bonding between amine-modified diamondoids and DNA nucleobases was proven strong enough to be detected, while a comparison of the electronic properties of the diamondoid/nucleobase complexes showed distinguishable characteristics [98]. This suggests a possible electronic detection of the nucleobase identity, which needs to be confirmed by inspection of the tunneling current signals. To this end, in this work, we perform quantum transport simulations as a proof of concept on the ability of diamondoid-functionalized electrodes to identify different types of DNA nucleotides. Note, that nucleotides are the nucleobases attached to a sugar-phosphate group of the DNA backbone. In the following, a lower diamondoid, amantadine (ama), is used as the functionalization molecule of gold electrodes. These electrodes can potentially be embedded in a solid-state nanopore. In order to effectively attach the functionalizing molecule on the gold surface of the electrode, one hydrogen atom of the diamondoid cage has been replaced with a thiol group at the apical position [105]. Our investigation (as an extension to chapter 3) will involve the four nucleotides, as well as a mutated nucleotide, and an epigenetic marker. We show, that diamondoid-functionalized gold electrodes can be used to identify these molecules and differentiate between them.

4.2 Computational Details

We use the amantadine-functionalized gold electrodes to investigate the quantum transport properties of four natural nucleotides: deoxyadenosine monophosphate (dAMP, in the following abbreviated simply as A), deoxythymidine monophosphate (dAMT, in the

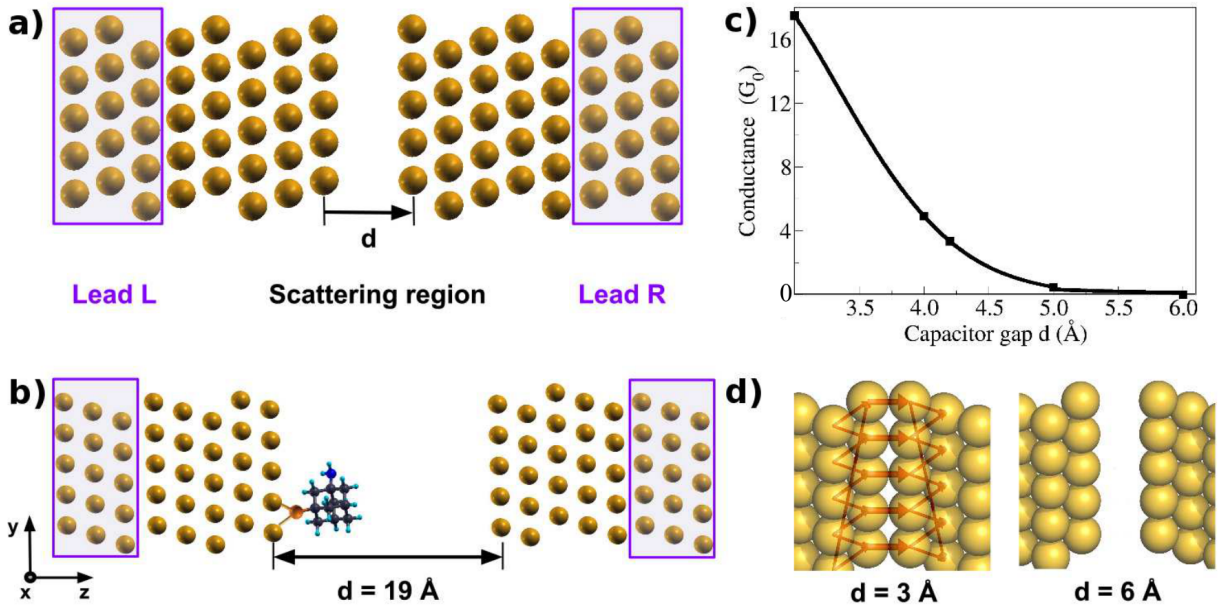

Figure 4.1: The computational setup for the transport calculations along the **Z** direction is shown in panels **a)** and **b)**. Three outer layers of the Au(111) material on either side of the nanogap form semi-infinite leads. The inner five layers of Au(111) on either side along with the embedded molecules form the scatter region. **c)**: Variation of the zero bias conductance with the capacitor gap size **d)**: Local current [104] across the nanogap for two different capacitor gaps. In these panels, gold atoms are shown in yellow, carbon in gray, nitrogen in blue, hydrogen in cyan, and sulfur in orange.

following abbreviated simply as T), deoxycytidine monophosphate (dAMC, in the following abbreviated simply as C) and deoxyguanosine monophosphate (dAMG, in the following abbreviated simply as G). These are separately placed between the functionalized electrodes. Here, we investigate only the single-functionalization case, that is only the left electrode has been functionalized by a diamondoid. Only one diamondoid (ama) will be used in this work, as a proof of concept. The choice of this diamondoid is based on a broader analysis (to be published elsewhere) using additional diamondoids as functionalization molecules. In addition to the analysis of the tunneling current signals arising from each nucleotide between the functionalized electrodes, we extend the investigation to study the efficiency of such a functionalized-nanopore device in distinguishing natural nucleotides from mutations (the 8-oxodeoxyguanosine monophosphate - 8-oxo-Gua, in the following abbreviated simply as d8oG [97]) and epigenetic markers (the 5-methyl deoxycytidine monophosphate - 5-mdCMP, in the following abbreviated simply as d5mc [96]) . The diamondoid is attached on a (111) gold surface. For the calculations we have used semi-infinite electrodes.

In this work, density functional theory based (DFT) [58,59] simulations as implemented in the code SIESTA [88] were carried out. The use of quantum-mechanical calculations has been proven very efficient in the field of nanopore sequencing [106]. We have used the generalized gradient approximation of Perdew-Burke-Ernzerhof (PBE-GGA) [62], and the norm-conserving Troullier-Martins pseudopotentials [89]. For expanding the Kohn-Sham states, we have considered a double-ζ with polarization basis-set (DZP) for the molecules, and a single-ζ with polarization (SZP), for the gold atoms ($5d^{10}$, $6s^{1}$). These basis sets have been proven efficient in simulating similar systems [77, 98]. An energy shift of 0.01 Ry with a real space sampling grid (mesh cutoff) of 200 Ry, and $5 \times 5 \times 1$ kpoints using the Monkhorst-Pack scheme were also used. The ionic relaxations were performed until the net forces of each atomic component become smaller than 0.01 eV/Å. The gold (111) unit cell was fully relaxed and we obtained the lattice constant of 4.186 Å which compares well with the data reported in literature [107].

The electronic transport calculations are performed using DFT combined with the non-equilibrium Green's functions (NEGF) formalism, as implemented in the TranSIESTA [76] code. Fig. 4.1a shows the electronic transport setup, composed of three parts: the two electrodes (left and right) and the scattering region (device).

Fig. 4.1c) shows the zero bias conductance for different nanogap widths (d). We have noticed a high conductance for distances smaller than 4.5 Å. For distances larger than 5 Å the conductance goes to zero. The local current is shown in Fig. 4.1d, for two nanogap widths. For the smallest nanogap width of 3 Å, we have seen the highest conductance. Since, no bias voltage was applied across the electrodes, this conductance can lead to the projection of the transmittance and the tunneling current passing across the gap. For a nanogap of 6 Å, the conductance is zero and the local current is observed to diminish.

For the device functionalization we have used a supercell of $14.8 \times 14.8 \times 40.8$ Å. Five unit cell repetitions in x and y direction, and ten perpendicular to the atomic planes in the z direction with a gap of 19 Å between the gold capacitor were used and are shown in Fig. 4.1b. A thiolated amantadine is placed close to the left gold layers and was relaxed until the thiol group of the amantadine was bonded to the gold surface. Next, a nucleotide was added close to amantadine with an orientation favoring the formation of hydrogen bonds with the diamondoid. The nucleobase and the sugar-phosphate group are pointing towards the right inner gold layer. The choice of the distance between the gold layers is based on the condition that even the largest two nucleotides (A and G) should fit inside the gap. These specific conformations are chosen for consistency to our earlier studies [98].

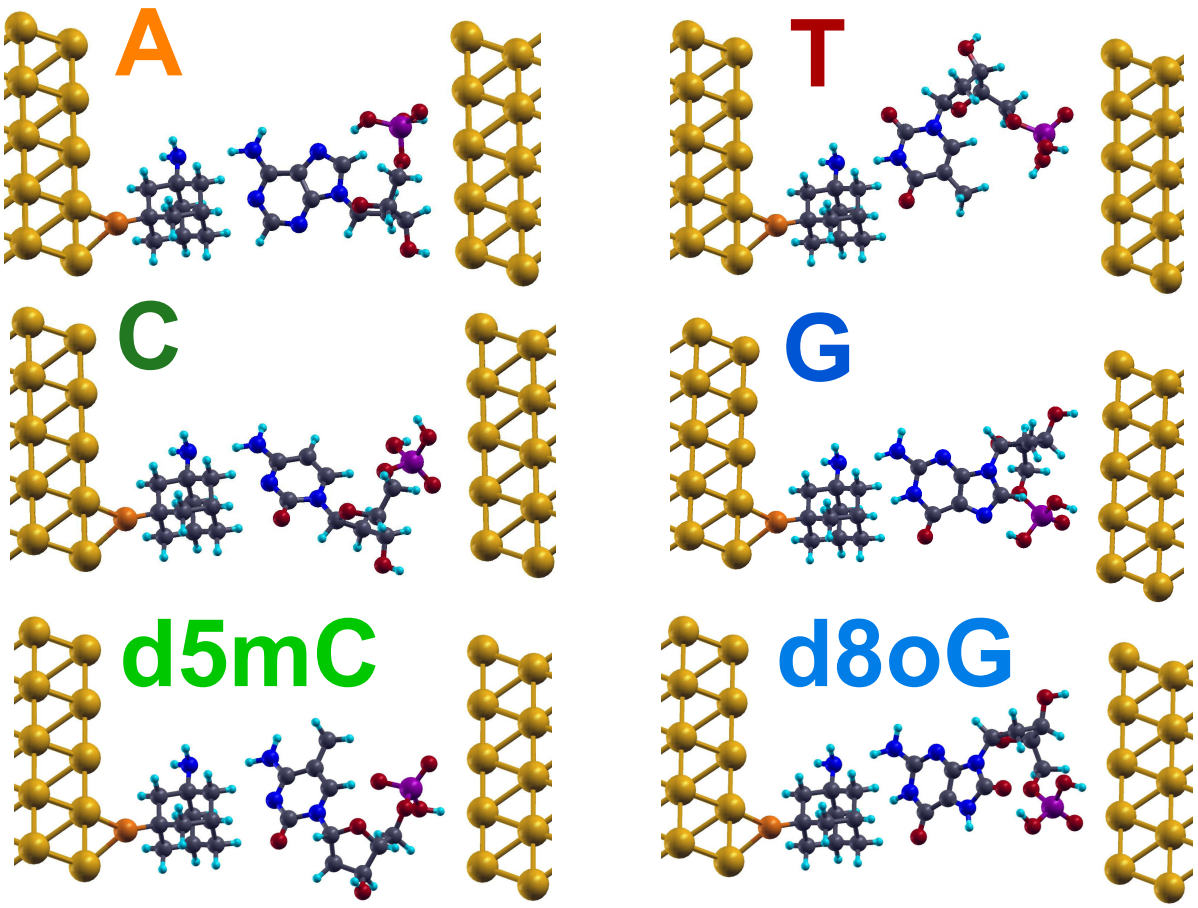

Figure 4.2: Fully relaxed geometries of diamondoid-functionalized electrodes including the nucleotides. The transport calculations are performed for the systems shown in this figure. The setups are generated for six nucleotide cases: the four natural ones, as well as one methylated and one mutated nucleotide, as denoted by the labels. In these panels, gold atoms are shown in yellow, carbon in gray, nitrogen in blue, hydrogen in cyan, oxygen in red, phosphorus in purple, and sulfur in orange. The same color coding is used throughout this work.

In real experiments, DNA is a charged molecule, which would react to a small bias voltage across the device and would re-orient with respect to the applied bias direction. Accordingly, a conformational scan would be necessary to capture the dynamics of the nucleotides within the electrodes and include the conformational variability in the analysis. In this work, though, we aim to present a proof of principles on the bio-sensitivity of a diamondoid-functionalized sequencing device and will not focus on the effect of the nucleotide conformations on the transport properties. This should be the subject of a separate study.

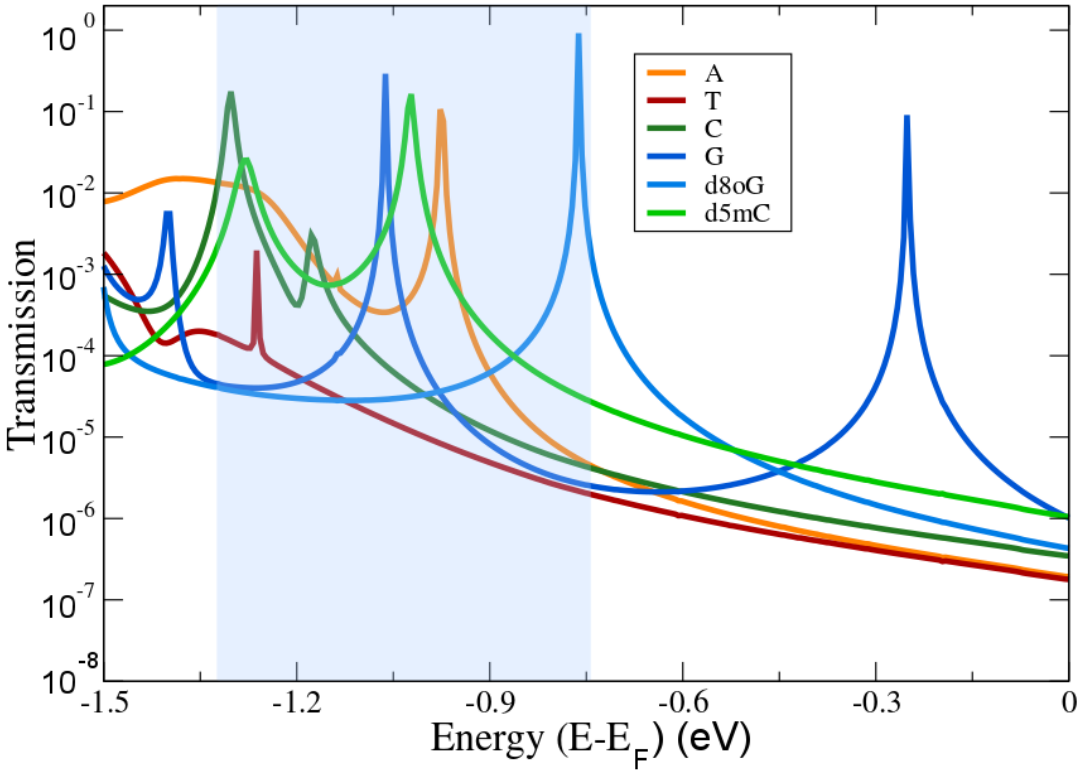

Figure 4.3: Transmission curves plotted on a semi-log scale for the six geometries shown in Fig. 4.2. The shaded region is of interest for sensing (see text). The energy axis has been shifted so as to align zero with the Fermi energy, E_F.

4.3 Results

The geometries obtained after relaxation for all the natural nucleotides (A, C, T, G), as well as for the two modified nucleotides (d5mC and d8oG) within the diamondoid-functionalized gold electrodes are depicted in Fig.4.2. For all cases, the nucleobases are pointing to the diamandoid side, while the phosphate groups are closer to the right electrode. No covalent bonding occurs between the nucleotides and the electrodes. The residual distances in each side are not larger than 2.5Å. The full relaxation of each geometry gives the best coupling between the molecules and the device. These configurations will be used further in evaluating the transport properties for all nucleotides.

The main challenge for the gold(111)-diamondoid functionalized device is to efficiently distinguish the nucleotides using the tunneling current signals. To this end, Fig. 4.3

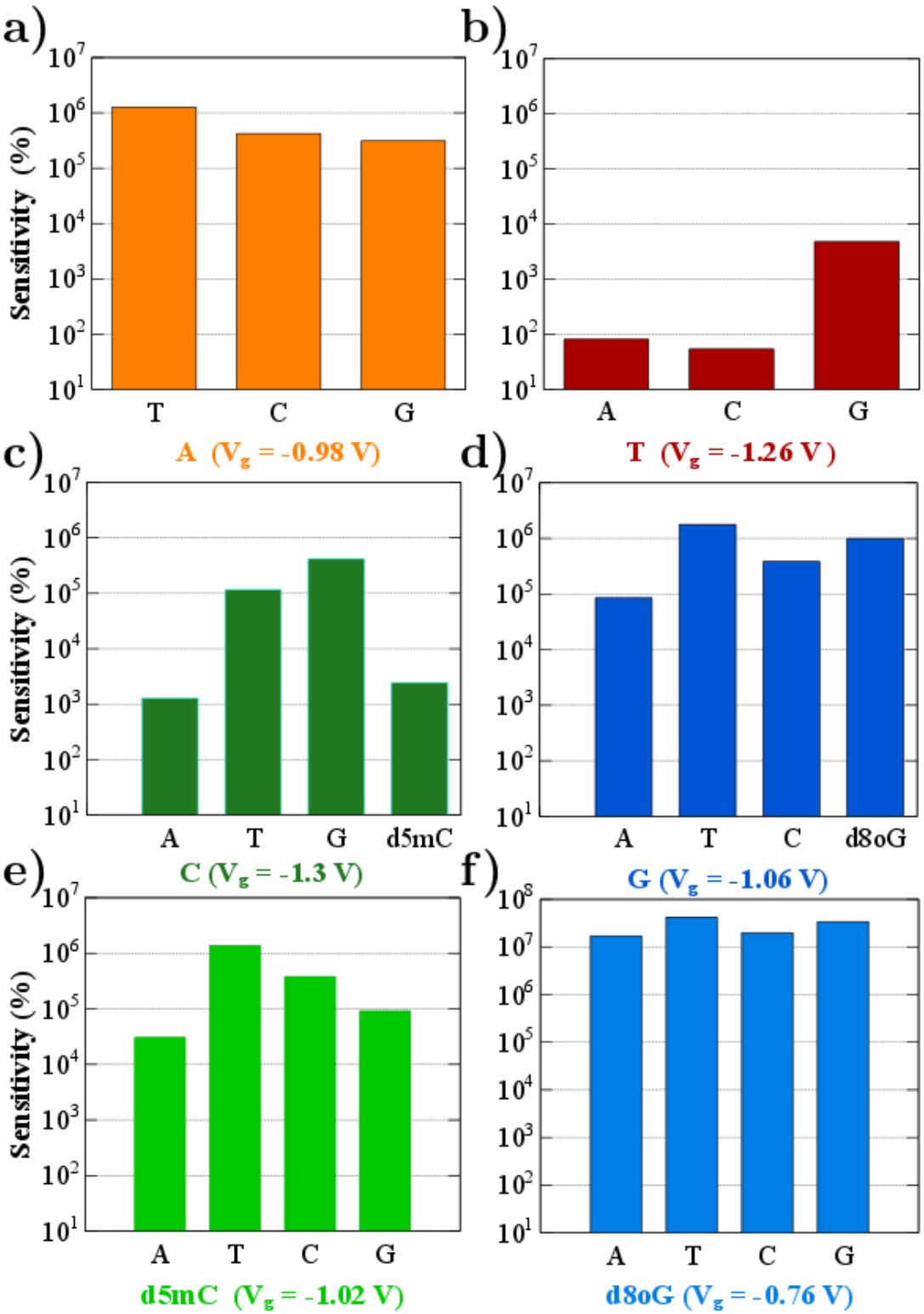

Figure 4.4: The device sensitivity is plotted on a semi-log scale for different gating voltages corresponding to the transmission peaks of the reference nucleotides. The labels denote the reference nucleotide and the respective gating voltage.

shows the calculated transmission curves for all nucleotides. We observe sharp peaks with $T(E) \approx 10^{-1}$, at different energies for each nucleotide in the transmission *T(E)* spectra. The values for $T(E)$ in the range $10^{-4} - 10^{-6}$ correspond to energies far from the resonances. In order to evaluate the peak origin, we calculated the projected density of states via Green's functions, which were projected in three atomic groups: (i) gold atoms, (ii) nucleotide, and (iii) diamondoid. We have found that the higher contribution for each peak comes from the nucleotides (see Fig. A.1 in appendix A). These results suggest that for specific energies, the transmittance spectra resonances lead to the nucleotide fingerprints. The observed T(E) hierarchy at the Fermi level (G > C > A > T) shows a difference up to one order of magnitude for the nucleotides compared to G. A and T show a very similar transmission close to the Fermi level, which might result in overlapping electronic signals, and a difficulty in distinguishing them from each other. The sensing device proposed here shows better read-out possibilities than other types of functionalizing devices. A qualitative comparison of the transmission peaks shown in Fig.4.3 of the present paper to those obtained from cytosine-functionalized gold electrodes (Fig.4 in Ref.77) reveals that in the former setup the peaks are energetically further separated and hence more distinguishable than in the latter case.

In the following, we analyze the energy range (shaded region in Fig. 4.3), which includes the resonance peaks for all nucleotides studied here, in order to propose a path to clearly identify each nucleobase. Accordingly, we will tune the Fermi energy in a nucleotide-specific way. In practice, in real experiments, this can be done by tuning the gating voltage of an external gate. For example, if we are interested in identifying d8oG to which the first peak in the right side of the shadow region corresponds to, we would need to tune the Fermi energy to $V_g = -0.76$ eV. In order to generalize this analysis, we will assume a similar definition of the gating conductance g (for a small bias) as a function of the gate voltage, V_g [108]:

$$g(V_g) = G_0 T(\mu) \tag{4.1}$$

where $\mu = \mathrm{E}_F - \mathrm{eV}_g$, T is the transmission function, and $G_0 = \frac{2e^2}{h}$.

In order to sense DNA based on the formalism above, a reference system with a specific conductance is needed. Based on this reference, the properties of each nucleotide can be identified. For tunneling systems, the reference device conductance is zero for a large capacitor distance, as was shown in Fig. 4.1c. Accordingly, another reference system is needed. As a solution to this, we introduce the device sensitivity, considering one

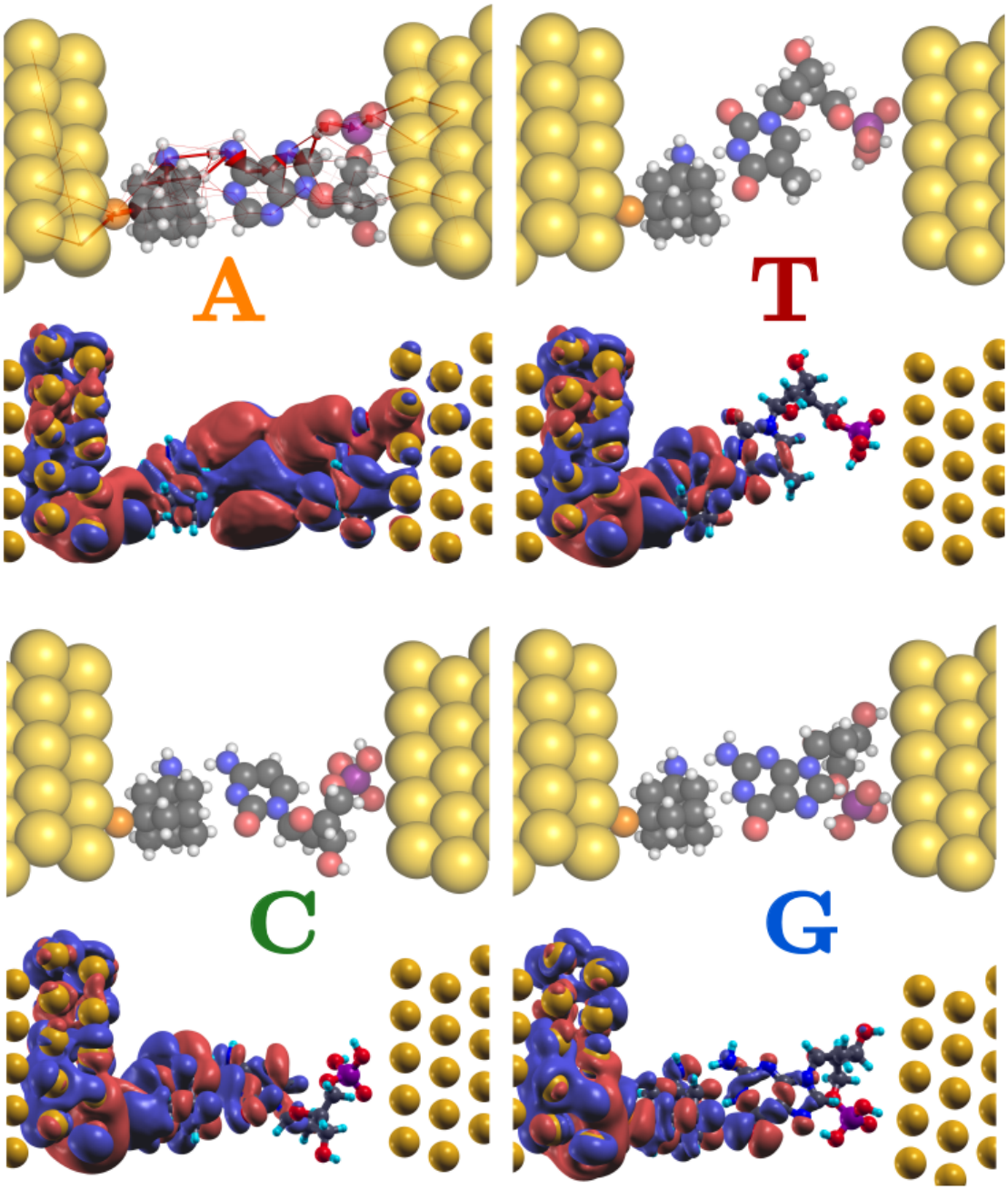

Figure 4.5: A comparison of four natural nucleotides at a gating voltage of V_g= -0.98 V which corresponds to the first transmission peak for A below the Fermi level. The local currents are plotted in the top panel and the eigenchannel wavefunctions at the bottom panel. For clarity all wavefunctions are plotted for the same isovalues, while positive values of the wavefunctions are shown in purple and negative in blue. The imaginary part is not clearly visible in most of the cases since its too small or below the cutoff.

nucleotide as a reference with respect to the sampling gating voltage V_g as:

$$S(V_g)[\%] = \left| \frac{g_{ref} - g_x}{g_x} \right| \times 100\,,$$

where g_{ref} is the reference gating conductance, which corresponds to the transmission peak of a specific nucleotide at a gating voltage V_g, and g_x is the gating conductance, at the same gate voltage (V_g) for any other nucleotide (excluding the reference nucleotide).

From the sensitivity at a specific sampling gating voltage, it is possible to observe how well resolved the conductance of the reference nucleotide will be with respect to other nucleotides. The device sensitivity according to the definition above and for all nucleotides is summarized in Fig.4.4. (Results for the modified nucleotides, d5mc and d8oG, are shown only in panels c)-f), since for these the question is whether they can be distinguished from their natural counterparts, C and G.) We begin the analysis with the sensitivity for A (Fig.4.4a). For this, A is taken as the reference at a gating voltage of $V_g = -0.98$ V. It is evident from this figure, that the sensitivity of the device in recognizing A is at least five orders of magnitude higher than its natural counterparts (T, C, and G). Accordingly, we can infer that at this gating voltage, the device could clearly identify A.

In order to understand the underlying physics in Fig.4.4a, the zero bias scattering state eigenchannel wavefunctions (EWF) [109], at $V_g = -0.98V$, are shown in the lower panel of Fig. 4.5. Both the real and imaginary contributions to the EWFs are shown. For the reference A, the real part of EWF is localized over the whole scattering region. For the non-reference nucleotides (T, C, and G) the EWF is mainly located at the diamandoid site, showing a small contribution on the nucleotides sites. For the non-reference nucleotides, the EWFs clearly decay as we move from the left electrode to the right, resulting in a smaller *T(E)*. Inspection of the imaginary part of the EWFs for A, points to states spreaded almost over the whole device, from the left, over the molecules, to the right electrode. This behavior clearly denotes an enhancement of the electronic coupling between the gold electrodes, the diamondoid, and A. Such a spreaded contribution is not observed for the non-reference nucleotides. This effect of electronic coupling is reflected in the local currents [104], which are also sketched in the top panel of Fig. 4.5. According to this figure and based on the above analysis, local currents are observed mainly for the reference A and not for the non-reference nucleotides, for which the local current is negligible. These results indicate that, based on the device sensitivity and the local current measurements for a gating voltage of $V_g = -0.98V$, it is possible to identify only A.

In Fig. 4.4 we observe that the device sensitivity spans a range of $10^2 - 10^7$ and note that the gating voltage should be carefully chosen in order to identify the nucleotides. At a

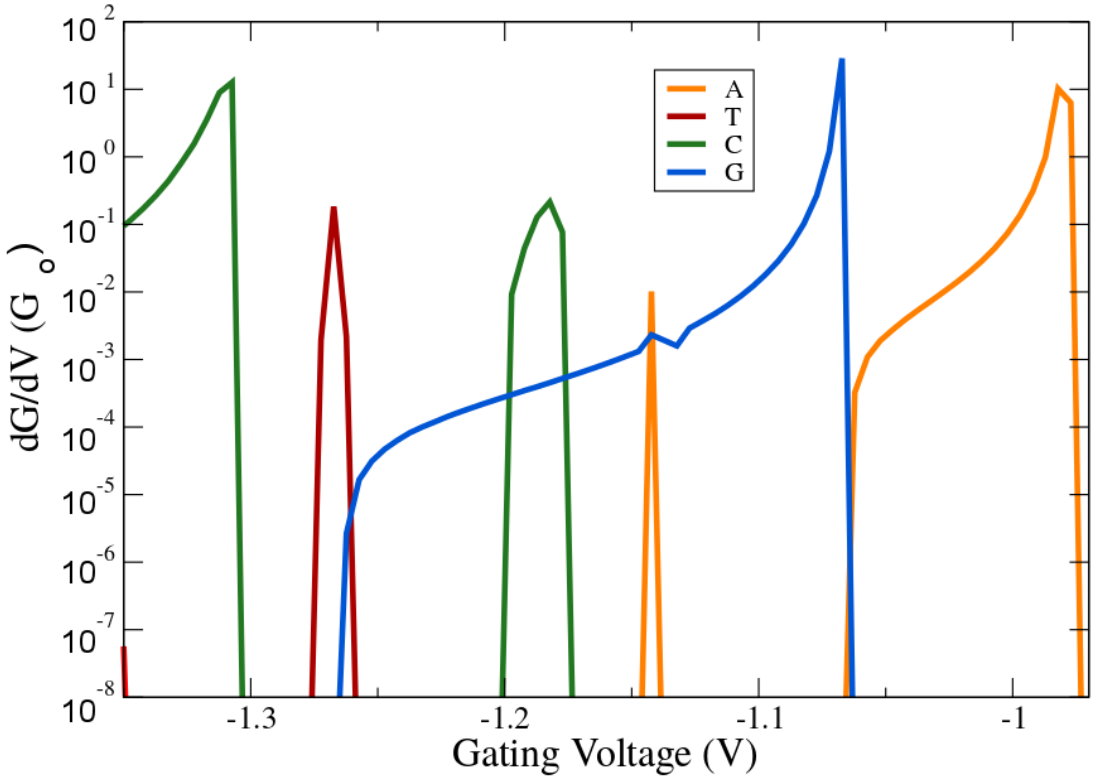

Figure 4.6: Derivative of the conductance with respect to the gating voltage plotted in the gating window for the four natural nucleotides

gating voltage V_g = -1.3 V, the conductance of C is at least three orders of magnitude more resolved compared to its natural non-reference counterparts (A, T, and G). At V_g = -1.06 V, the gating conductance for G is at least four orders of magnitude more resolved than that for the non-reference A, T, and C. For $V_g = -0.98V$ or $V_g = -1.06V$, the sensitivity distributions for the non-reference nucleotides are not considerably broad, but differ only by one order of magnitude. On the other hand, taking C as a reference for $V_g = -1.30V$, leads to a sensitivity in the range $10^3 - 10^5$ (see Fig. 4.4c).

Fig. 4.4b shows the sensitivity histogram for T at $V_g = -1.26$ V, calculated from the transmission curves in Fig. 4.3. In the latter figure, the transmittance peak for T is very sharp and smaller than the peaks for the other nucleotides. It is clear that T shows at least one order of magnitude difference in the transmission with respect to the relevant data for A, G, d8oG, and d5mC, and about two orders of magnitude difference from the C case. At this gating voltage, other nucleotides (A and C) have a much higher transmission

than T. In order to evaluate the contribution of the nucleotides on the transmission, we have calculated the projected density of state (PDOS). We have observed (see Fig. A.1b in appendix A) that the transmission peak for T has at least two major contributions: one from the diamondoid and one from the nucleotide T.

Up to this point, we have shown that it is possible to identify the nucleotides by choosing the respective gating voltage. In the following, we consider another possibility to distinguish the nucleobases based on the respective differential conductance $\frac{dG}{dV_g}$. This can resolve peaks of the nucleotides in cases when these are not easily distinguishable. This can for example be the case for T, according to our previous analysis. The advantage in using the differential conductance is that his quantity can lead to information on the conductivity changes for a range of gating voltages V_g. Fig. 4.6 shows how well resolved the conductance change for each natural nucleotide is. For A and C, the differential conductance does not overlap with that for the other nucleotides in the range $V_g < -1.3$ V and -1.06 V ¡ V_g¡ -0.97 V. In the range $V_g = -1.26 \pm 0.01$ V the differential conductance for T is highly resolved, as it is not overlapping with any of the other nucleotides. This observation indicates the possibility to distinguish T for this gating voltage range. The differential conductance for G is very broad and overlaps with A and C. Further inspection of Fig. 4.6 reveals three ranges for the gating voltage, in which no overlapping between the curve for G and those for the other nucleotides occurs. These results point to the possibility to use the information arising from the differential conductance in order to identify the natural nucleotides within a range of the gating voltage.

Another important issue in the field of DNA sequencing is the possibility to distinguish pristine nucleotides (like C and G) from their modified forms (like d5mC and d8oG). The transmission curves in Fig. 4.3 show defined peaks for these two modifications, which are not overlapping with the curves for the pristine nucleotides. In Fig. 4.4c and f, we show the sensitivity for pristine C and its mutant d5mC, and in Fig.4.4d and g the data for dGMP and d8oG, respectively. At the chosen gating voltage values the modified nucleotides can be easily distinguished from their pristine counterparts. The EWF and local currents are shown in Fig.4.7. For a gating voltage V_g=-1.3 V, corresponding to the peak for C in the transmission spectra, C can be distinguished from d5mC. For d5mC and a gating voltage of V_g=-1.02 V, corresponding to the transmission peak for this nucleotide, the sensitivity difference from the pristine C is about five orders of magnitude. The respective EWFs for d5mC and C are presented in the left panels of Fig. 4.7 for a gating voltage of V_g=-1.3 V. The real part of the EWFs is localized in both cases. In the pristine C, though, a stronger coupling to the right electrode occurs. This

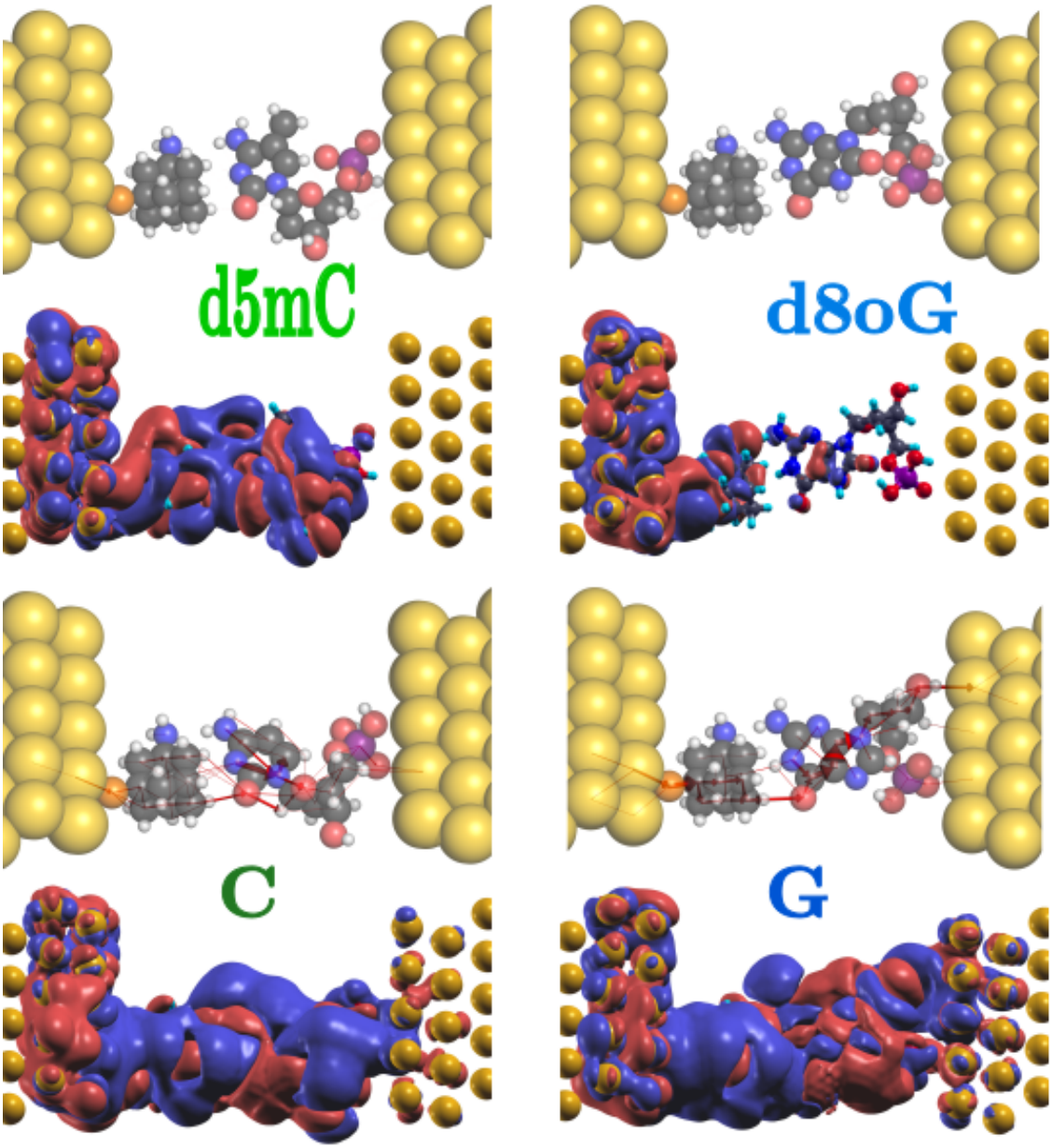

Figure 4.7: A comparison of C vs d5mC can be seen on left the panels for V_g= -1.3 V (corresponding to the second transmission peak below the Fermi level for C). A comparison of G vs d8oG is made in the right panels for V_g= -1.06 V (corresponding to the second transmission peak below the Fermi level for G). For each case, the local currents are sketched in the top panel and the EWFs at the bottom panel. For clarity all wavefunctions are plotted for the same isovalue and are color coded according to their positive (purple) and negative (blue) signs.

difference is mapped on the local currents, also shown, which are negligible for d5mC, but are finite for C.

Finally, by sampling at V_g=-1.06 V, the gating voltage corresponding to the transmission peak for G, it is possible to distinguish G from the mutation d8oG. For V_g=-0.76 V, which corresponds to the transmission peak for d8oG, the sensitivity for d8oG is seven orders of magnitude higher than that for dGMP. Going back to V_g=-1.06 V, at this voltage, the real part of the EWF is localized along the entire device for G and at the functionalized left electrode for the d8oG case, as shown in the right panels of Fig. 4.7 for G and d8oG. For this gating voltage, the electrodes in the pristine case (G) are coupled and there is a respective local current. In the mutated nucleotide (d8oG) there is no current at this gating voltage. These results again strongly indicate the possibility to distinguish the pristine G over its mutation d8oG. Inspection of the EWFs for d8oG shows a significant difference in the symmetry of the eigenchannel compared to that of G, which suggests a larger asymmetry in the I-V curves for the case of d8oG with respect to G at a low applied bias [110]. This asymmetry indicates that d8oG can potentially reveal its rectifying behaviour when the gating voltage is tuned so that the conduction due to these orbitals moves closer to the Fermi level.

4.4 Conclusions

Using quantum-mechanical calculations, we were able to provide a proof of concept regarding the feasibility of a bio-sensor based on amantadine-functionalized gold electrodes. Our work has shown that such a device can detect the different nucleobase and their modifications based on quantum tunneling measurements across the electrodes. Different gating voltages can tune the sensitivity of the functionalized electrodes with respect to specific nucleotides having a high transmission peak at these voltages. We have also revealed the sensing mechanism for one of the pristine nucleotides (T) by analyzing the derivatives of the conductance with respect to the values of the gating voltage. The sensitivity at different gating voltages is also related to the coupling or decoupling of the functionalized electrodes, and the observation or lack of observation of local currents. In order to reveal the physics underlying the observed transport properties, the scatter state wavefunctions at a higher transmission, as well as the local current plots were presented and discussed.

Our results involve the zero bias voltage case, but can give an indication of the IV-characteristics of the diamondoid-functionalized device at a small applied bias. The current as a function of applied voltage in the low bias regime (up to 0.1 V) for d5mC and d8oG should be significantly different compared to their respective natural nucleotides.

Our data support this assumption, as a low applied bias should not prevent the possibility of distinguishing the different nucleotides based on their I-V response [111]. It is not trivially clear how the transmission peaks would shift with respect to an applied bias. However, Figs.4.5,4.7 indicate that the EWFs in all cases are more associated with the same (left) electrode implying that the transmission peaks would shift towards the same direction to more negative energies. Accordingly, at a low bias and for a moderate coupling of the electrodes, we can assume that all the transmission peaks do not shift too strongly and that the shift is similar in all cases. The sharp transmission peaks for G and d8oG at -0.28 eV and -0.75 eV, respectively would then show a sharp rise in the current for G between -0.2 V and -0.3 V. The sharp rise in the current for d8oG would be expected at more negative bias voltages. For C and d5mC having their transmission peaks below -1 eV, a bias of about -1 V beyond the low bias limit would be needed. At such a high applied bias the situation is expected to change, as the peaks would shift in a different way, possibly leading to overlapping and indistinguishable transmission peaks. Overall, the amount of increase in the current for each nucleotide is related to the gating voltage needed to shift the transmission peak closer to the Fermi energy and the applied bias voltage. Note, that within our methodology, the calculations at a very small bias are still possible as the system is still not out of equilibrium. The application of a large bias, though could also lead to a breakdown of the system.

The focus of this work was to reveal the suitability of diamondoid-functionalized electrodes as biosensors. There are of course many complex issues that have not been taken into account at this point. Some of these involve the effect of conformational variability and dynamics in the transport properties across the electrodes and the corresponding sensitivity of the device. The effect of the surrounding medium, i.e. water and ions is also expected to play a major role. The question is whether these factors will only shift the transport spectra shown in this work or will make the whole picture more complex. Some of these points we aim to address in follow-up studies in the near future. A conformational scan of the DNA orientation in the nanopore and the role of a solvent in the pore can be unveiled in view of the electronic current signatures in diamondoid-functionalized nanopores. The role of the solvent is expected to influence the transport properties. Next in chapter 5, we turn our attention to the comparison of the performance of different diamondoid derivatives as functionalization molecules in a nanopore device, which is also expected to shed light onto pathways to enhance the sensitivity of functionalized nanopores.

Acknowledgment

Part of this chapter was reproduced from Ref. [51] with permissions from the royal society of chemistry.

5 Comparison of diamondoid functionalised devices

As a follow up to the amantadine-functionalized devices discussed in detail in chapter 4, we perform a detailed comparative investigation of different diamondoid-functionalized electrodes in order to point to the functionalizing molecule with the most efficient sensing properties. The remainder of this chapter is organized as follows: introduction, the computational scheme and set-up of the functionalized sensing electrodes, and the comparative analysis of the results for different electrode functionalizations. In the end, we discuss the impact of these results and conclude.

5.1 Introduction

Derivatives of diamondoids have been shown to form hydrogen bonds to DNA nucleobases [98, 112] and efficiently functionalize gold electrodes to sense DNA nucleobases and their mutations [51, 98]. These functionalized electrodes can be embedded into nanopores in order to produce DNA sequencing devices [1, 2, 77]. DNA molecules can be electrophoretically driven through such nanopores giving rise to nucleobase transverse current signals across the nanopores [36, 113]. Using a functionalization in the nanopore has the potential to enhance these transverse signals [77, 114]. It is crucial to find small molecules of the size of the nucleobases, which can functionalize nanopores and indeed increase the signal-to-noise ratio in the electronic current measurements. Such an increase is required to facilitate an almost error-free reading-out of the DNA nucleotides and promote sequencing.

Work along these lines is carried out in view of choosing a molecule for efficient functionalization of electrodes embedded in nanopores. The term 'efficient' is here meant as enabling a selective read-out of the nucleotides through these electrodes which lead to distinguishable electronic signals for each nucleotides. To this aim, lower amine-doped

diamondoids [80] are scanned and are attached to gold electrodes, which are in turn investigated for their biosensing properties.

5.2 Computational Details

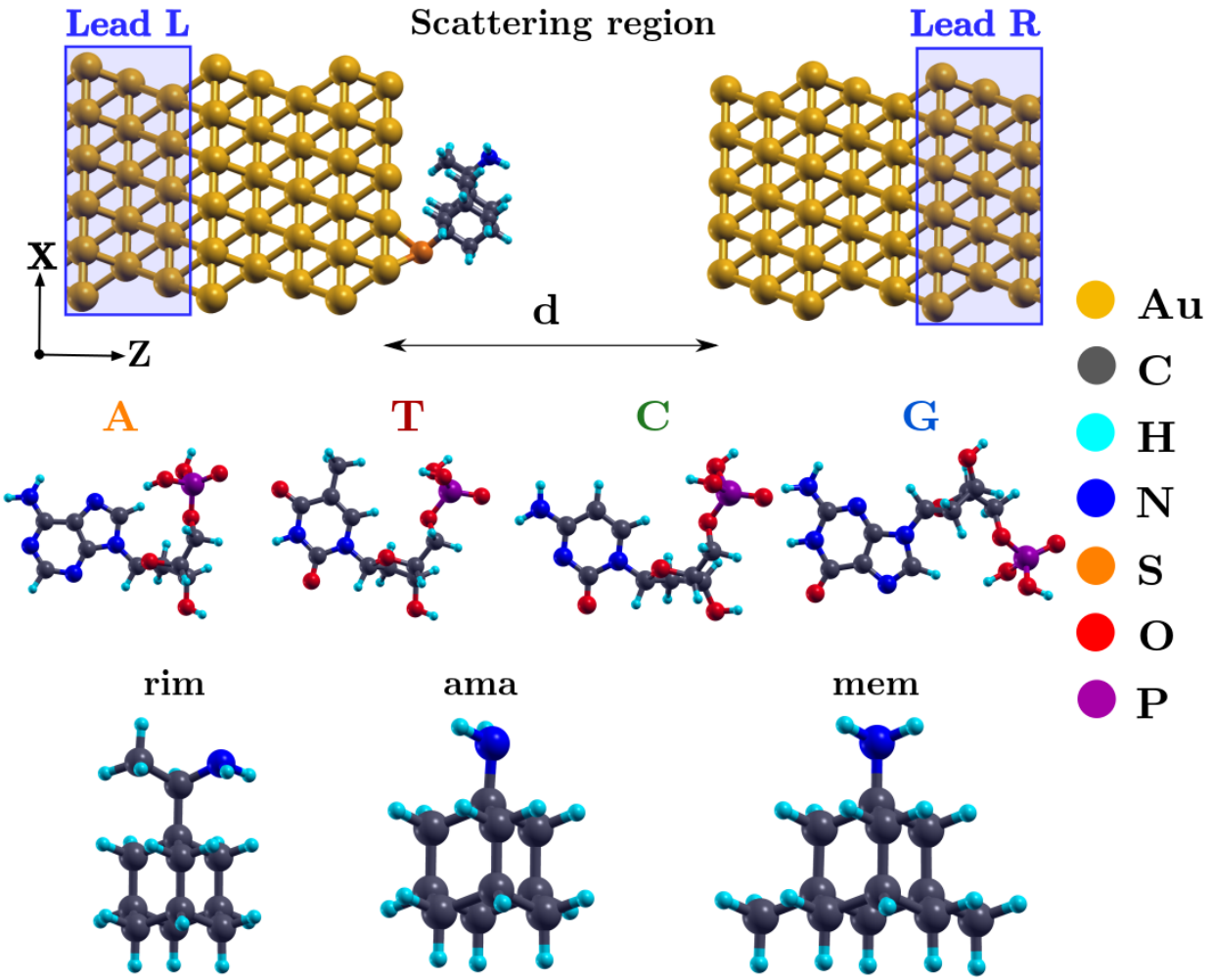

Figure 5.1: In the top row, a typical example of diamondoid-functionalized Au(111) electrodes studied in this work are shown. A rimantadine molecule is shown to functionalize the electrodes. Electronic transport occurs along the z-direction. The four nucleotides which will be placed between the electrodes are also shown in the middle row: deoxyadenosine monophosphate (A), deoxythymidine monophosphate (T), deoxycytidine monophosphate (C), and deoxyguanosine monophosphate (G). In bottom row, the three amine derivates of lower diamondoids, rimantadine (rim), amantadine (ama), and memantine (mem) are respectively shown. The color coding in the right panel will be used throughout this chapter.

In order to assess the sensing efficiency of diamondoid-functionalized gold electrodes such as the ones shown in Fig.5.1 (top row) we examine their electronic and transport properties when DNA nucleobases are placed in the gap between them. The three different amine-modified diamondoid derivatives [80] shown in Fig.5.1 (bottom row), rimantadine, amantadine, memantine are used for the functionalization of the electrodes. These will be referred to as 'rim', 'ama', and 'mem', respectively, in the following. The four DNA nucleotides shown in Fig.5.1 (middle row), deoxyadenosine monophosphate, deoxythymidine monophosphate, deoxycytidine monophosphate, and deoxyguanosine monophosphate are placed in the electrode gap. We will refer to these simply as 'A', 'T', 'C', and 'G', respectively. Each nucleotide interacts with the functionalized electrodes through hydrogen bonds with the functionalizing diamondoid. An extensive analysis of amantadine-functionalized gold electrodes was carried out and presented in chapter 4. Hence, results for the ama-functionalized electrodes has been reproduced solely for comparison purpose alone.

The systems modeled include two Au(111) electrodes, left and right, and the scattering region of gold. The three outer layers of Au(111) on either side of the electrodes form the semi-infinite lead. The ten inner layers of Au(111) along with the embedded molecules form the device region as sketched in Fig.5.1 (top row). A gap of a fixed distance d separates the two electrodes. This gap is sufficiently large to include the functionalizing diamondoid and a nucleotide. We have tested that for distances $d > 4$ Å, no tunneling current exists [51]. Note, that we investigate only the single-functionalized case, in which the diamondoid is chosen to functionalize only the left electrode. The right electrode remains unmodified. The transport direction occurs from the left electrode to the right one in the positive z-direction as shown in Fig.5.1 (top row). The nucleotides are initially placed close to the diamondoid at distances which would lead to the formation of hydrogen bonds [51]. The functionalizing diamondoid and the nucleotide interact through hydrogen bonds. In this binding, amantadine and memantine are always donors. In the rimantadine case, though, the diamondoid can be a donor or an acceptor in the hydrogen bonding to the nucleotides depending on the relative arrangements of these two molecules. For the rimantadine case, then, we need to account for the two different arrangements in which rimantadine acts as (a) an acceptor ('rim-1') or (b) a donor ('rim-2') to the hydrogen bonding. These two configurations are depicted in Fig.5.2.

A density functional theory (DFT) scheme as implemented in SIESTA [88] was used to investigate the systems. The electronic transport calculations were carried out using the non-equilibrium Green's functions (NEGF) approach within TranSIESTA [76].

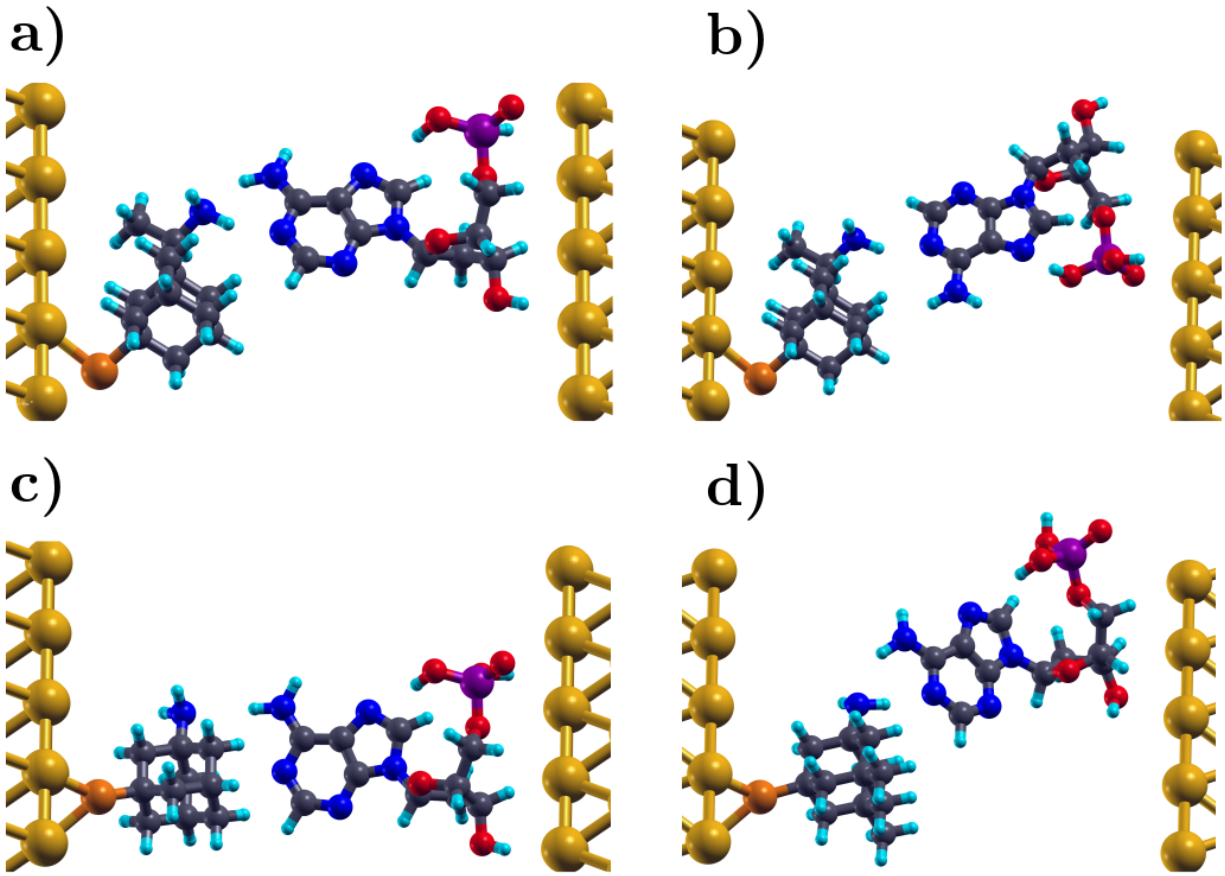

Figure 5.2: The different arrangements of the diamondoids with respect to the nucleotides. (a) rim-1, (b) rim-2, (c) ama, and (d) mem forming hydrogen bonds with the neighboring nucleotide (shown here on the example of A). In (a), (c), and (d) the diamondoid is a hydrogen acceptor to the binding, while in (b) it is a donor to the bond. For the color coding, we refer the reader to the color bar in Fig.5.1.

The generalized gradient approximation of Perdew-Burke-Erzernhof (PBE-GGA) [62], and the norm-conserving Troullier-Martins pseudopotentials [89] were used. For the expansion of the Kohn-Sham states, a double-ζ polarized basis-set (DZP) for the nucleotides, diamondoid derivatives and a single-ζ with polarized (SZP), with ($5d^{10}$, $6s^1$) orbital states for the gold atoms were considered. These basis sets have been proven efficient in simulating similar systems [51,77]. An energy shift of 0.01 Ry with a real space sampling grid (mesh cutoff) of 200 Ry, and $5 \times 5 \times 1$ k-points using the Monkhorst-Pack scheme were also used. The ionic relaxations were performed until the net atomic forces are smaller than 0.01 eV/Å. For the device functionalization, a supercell of $14.8 \times 14.8 \times 40.8$ Å ($14.8 \times 14.8 \times 39.8$ Å) for rimantadine (memantine) was used. Five unit cells in the x and y directions and ten along the z direction with a gap of 19Å(18Å) for rimatadine (memantine) were repeated to build the supercell.

For the two semi-infinite gold electrodes, the (111) surface was taken and were structurally relaxed. A lattice constant of 4.186 Å was obtained from the relaxation and compares well with literature data [107]. In the second step, a thiolated amine-modified diamondoid (Fig.5.1 (middle row)) is placed close to the left gold layers and relaxed until the thiol group of the diamondoid was bonded to the gold surface. Finally, a nucleotide was added close to diamondoid with an orientation favoring the formation of hydrogen bonds with the diamondoid. The sugar-phosphate group are pointing towards the right inner gold layer. The choice of the distance between the gold layers is based on the condition that even the largest two nucleotides (A and G) could fit inside the electrode gap. These specific conformations are chosen for consistency to our earlier studies (chapter 3).

5.3 Results and Discussion

We begin our analysis with the electronic transmission curves for all cases. The calculated transmission for the rimantadine- (both acceptor and donor conformations) and the memantine-functionalized electrodes are summarized in Fig.5.3. The data for all four nucleotides are included in the graphs. In these, the shaded areas correspond to a region including the most prominent peaks for the nucleotides. These areas are considered as the energy window for scanning the sensing properties of the diamondoid-functionalized electrodes and will be used for the comparison of the efficiency of each diamondoid.

Inspection of Fig.5.3 reveals that the transmission hierarchy at the Fermi energy, $T(E_F)$, for rim-1 follows the trend $G > A > C > T$. The respective peaks are found in the range $10^{-2} - 10^{0}$. On the other hand, for rim-2 and mem exhibit different $T(E_F)$ hierarchy, including a much wider spread, namely $C \gg G \gg T \gg A$ and $C \gg G > T \gg A$, respectively. For rim-2 the values of the $T(E)$ peaks differ and lie in the range $10^{-3} - 10^{-1}$. For mem, the $T(E)$ peaks differ by one order of magnitude, but the T and G peaks have similar values (Figure 5.3d). Note that the relevant hierarchy for amantadine was found $G \gg C \gg A > T$ with values for the peaks in $T(E)$ in the range $10^{-3} - 10^{-1}$ ((Figure 5.3c). The fact that the peaks for all nucleotides in all functionalization cases are clearly distinguishable points to efficient and device-specific sensing of the nucleotides.

The zero bias conductance, which is the the transmission at the Fermi energy could give

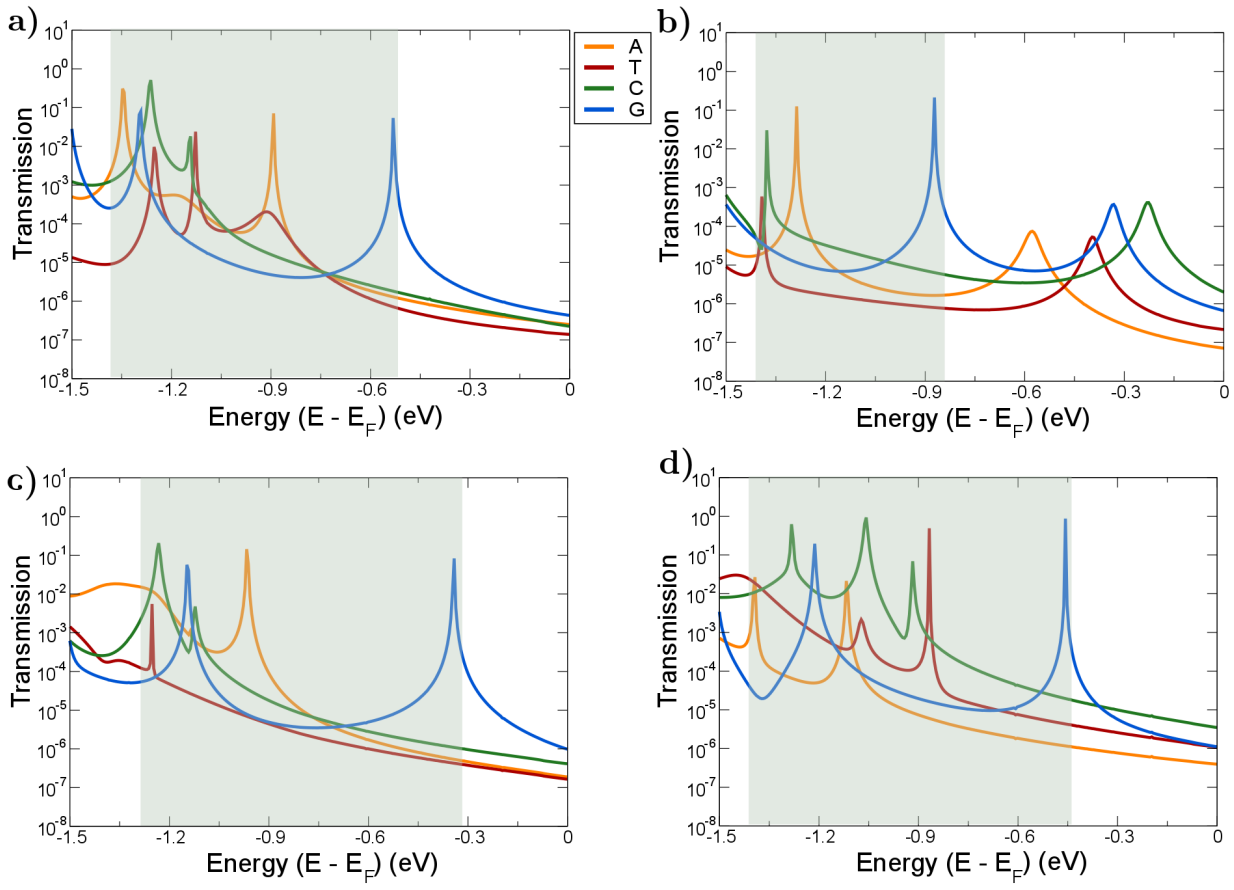

Figure 5.3: Transmission spectra plotted as a function of energy relative to the Fermi energy (aligned with zero) on a semi-log scale for the different functionalized electrodes. In these, a) rim-1, b) rim-2, c) ama, and d) mem are used as functionalizing molecules. The shaded areas correspond to the scanning window (see text) for the sensing analysis.

another indication of whether sensing is efficient or not. It is necessary for the discrimination of the nucleotides that the zero bias conductance for all cases is distinguishable. The results in Fig.5.3 show that these are indeed distinguishable at the Fermi energy. There is an overlap of the zero bias conductance values for T and G and the memantine functionalization, as well as A and C in the rim-1 functionalization. In the amantadine functionalization, the curves at the Fermi level for A and T are very close together, while those for C and G are clearly distinguishable (Fig. 5.3c) [51]. In order to deal with similar or overlapping signals for the zero bias conductance at the Fermi energy, we turn to gating sensing. Accordingly, the resonant peaks for each nucleotide and the different functionalizations were sampled. This is similar to the experimental case of tuning the Fermi energy through gating in a specific energy region (the shaded regions in Fig.5.3) where resonances arising from the different nucleotides occur. Nucleotide-specific trans-

mission peaks are evident in the gating windows in all functionalized electrodes studied here. Our results suggest that it is possible to identify the nucleotides with the functionalization diamondoids by tuning the Fermi energy in a nucleotide-specific way. Overall, the memantine-functionalized electrodes seem to have the best potential for sensing as the transmission peaks for the four nucleotides are clearly distinguishable compared to the rim-1, rim-2, and ama cases. In the the rim-1, rim-2, and ama cases, some peaks are very close to each other and would not allow a clear identification of the respective nucleotides. In the following discussion, we focus on the analysis of the mem-functionalization.

5.3.1 DNA Identification

As discussed before, the transmission peaks in the mem case in Fig.5.3c, are clearly distinguishable. In the following, we illustrate the protocol to identify one particular nucleotide of the four types, which we call the reference nucleotide, and distinguish it from the other possible three nucleotides, which we refer to as non-reference nucleotides. Accordingly, in order to identify for example G, which corresponds to the first peak below the Fermi energy in the shaded region, a gating voltage of $V_g = -0.46$ V would need to be applied in order to shift the Fermi level to that energy. In order to understand the electronic characteristics of the mem-functionalized gold electrodes, we turn to the zero-bias scattering state eigenchannel wavefunctions (EWF) [109]. At $V_g = -0.46$ V these are shown in Fig. 5.4.

For the reference nucleotide G, the real part of EWF is delocalized over the whole scattering region. For the non-reference nucleotides (A, T, and C), the EWF are mainly located at the diamondoid site and the functionalized side of the electrodes. In those cases, only a small contribution on the nucleotides sites is seen. Accordingly, for G, there is a clear and enhanced strong coupling of the left and right electrodes, memantine, and the G nucleotide indicating higher probability of electrons flowing at this referred gate voltage. For A, T, and C, though the EWF's clearly decay as we move from the left electrode to the right, resulting in negligible transmission.

This qualitative analysis can be quantified through the concept of sensitivity (introduced in chapter 4), which reveals how well resolved the conductance of a reference nucleotide will be with respect to other nucleotides:

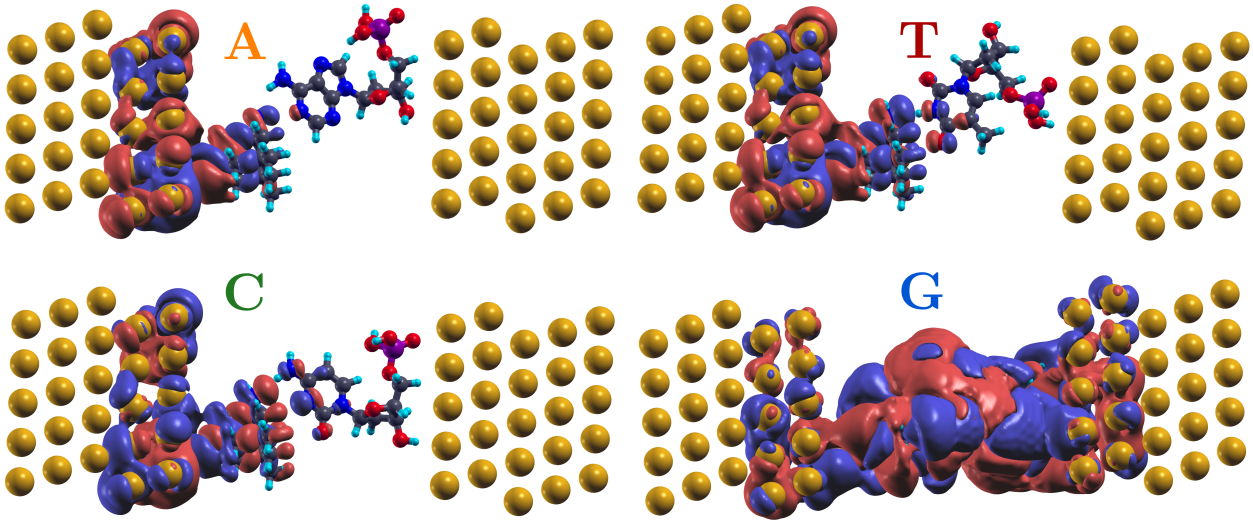

Figure 5.4: Eigenchannel wavefunctions for memantine functionalized gold(111) for the four nucleotides at V_g= -0.46 V corresponding to the first transmission peak of G below the Fermi level. For clarity all wavefunctions are plotted for the same isovalues, with positive values of the wavefunctions in red and negative in blue. Both the real and imaginary contributions to the EWFs are shown, but the imaginary part is either too small or below the cutoff and is not clearly visible in most of the panels.For the color coding of the atoms, we refer the reader to the color bar in Fig.5.1.

$$S(V_g)[\%] = \left| \frac{g_{ref} - g_x}{g_x} \right| \times 100\,,$$

where g_{ref} is the reference zero-bias conductance under application of a given gating voltage, which corresponds to the transmission peak of a specific nucleotide at a gating voltage V_g, and g_x is the gating conductance, at the same gate voltage for any other nucleotide (excluding the reference nucleotide). Following the discussion on the electronic wavefunctions and the mem case, we begin the analysis with the sensitivity $S(V_g)$ for recognizing G. This was found to be at least six orders of magnitude higher than A, T, and C as long as the gating voltage is very close to $V_g = -0.46$ V (the energy corresponding to the first peak for G in the transmission graph in Fig.5.3d). The other two nucleotides, T and C, would easily be recognized as long as the device is tuned at the correct gating voltage. Within the same context and for the same device, using a gating voltage of $V_g = -1.12$ V which corresponds to the transmission peak of A in (Fig.5.3d) would resolve A by at least two orders of magnitude more than the other nucleotides T, C, and G. Overall, the sensitivity of a memantine-functionalized nanogap (Fig. 5.6) was found to be higher than the nanogap functionalized by other diamondoids investigated as part of this study.

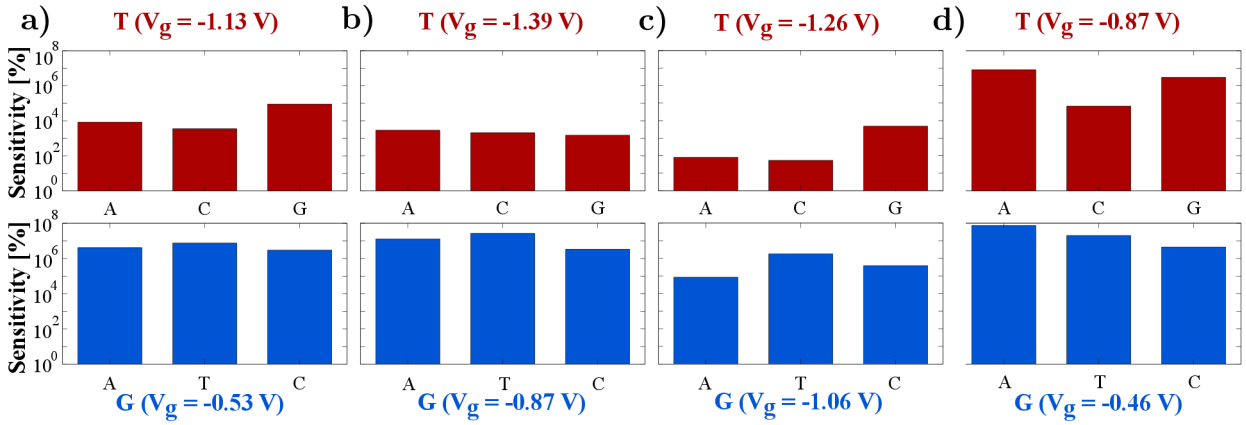

Figure 5.5: The device sensitivity is plotted on a semi-log scale for the a) rim-1, b) rim-2, c) ama, and d) mem diamondoid-functionalized nanogaps. The top panel shows the sensitivity in reading-out T, while the bottom panel shows the sensitivity in reading-out G. The different gating voltages correspond to the transmission peaks of the reference nucleotides in Fig.5.3 and in our previous study [**?**]. The labels denote the reference nucleotide and the respective gating voltage.

The results for all diamondoid functionalizations are summarized in Fig.5.5. The best and worst identified nucleotide from our analysis are taken (see Fig.5.3). These are G and T, respectively. G has in all cases a well defined transmission peak, while the peak for T is often almost overlapping with the peak of another nucleotide. In Fig.5.5, the gate voltage corresponding to the transmission peak of T or G for each of the diamondoid cases is shown. It becomes clear from the figure, that T is least distinguishable with the ama-functionalized electrodes, as it is less than 2 orders of magnitude better resolved than C (top panel in Fig.5.5c). Also, using the rim-2 setup, T can be 3 orders of magnitude better resolved than A, C, and G, which at this gate voltage have a very similar conductance and their peaks cannot be separated (top panel in Fig.5.5b). On the other hand, G can be best identified with a mem-functionalized device and up to 8 orders of magnitude better than A, 7 orders of magnitude better than T, and about 6 orders of magnitude better than C (bottom panel in Fig.5.5d). With the ama-functionalization, which was not very efficient for T (see the analysis in chapter 4), G can be 6 orders of magnitude better identified than T at the gating voltage corresponding to the transmission peak of G. Overall, the sensitivity analysis in Fig.5.5 clearly underlines the differences in an efficient identification of the DNA nucleotides with the different diamondoid-based gold electrodes. A good choice of the diamondoid is essential for a clear identification of the nucleotides.

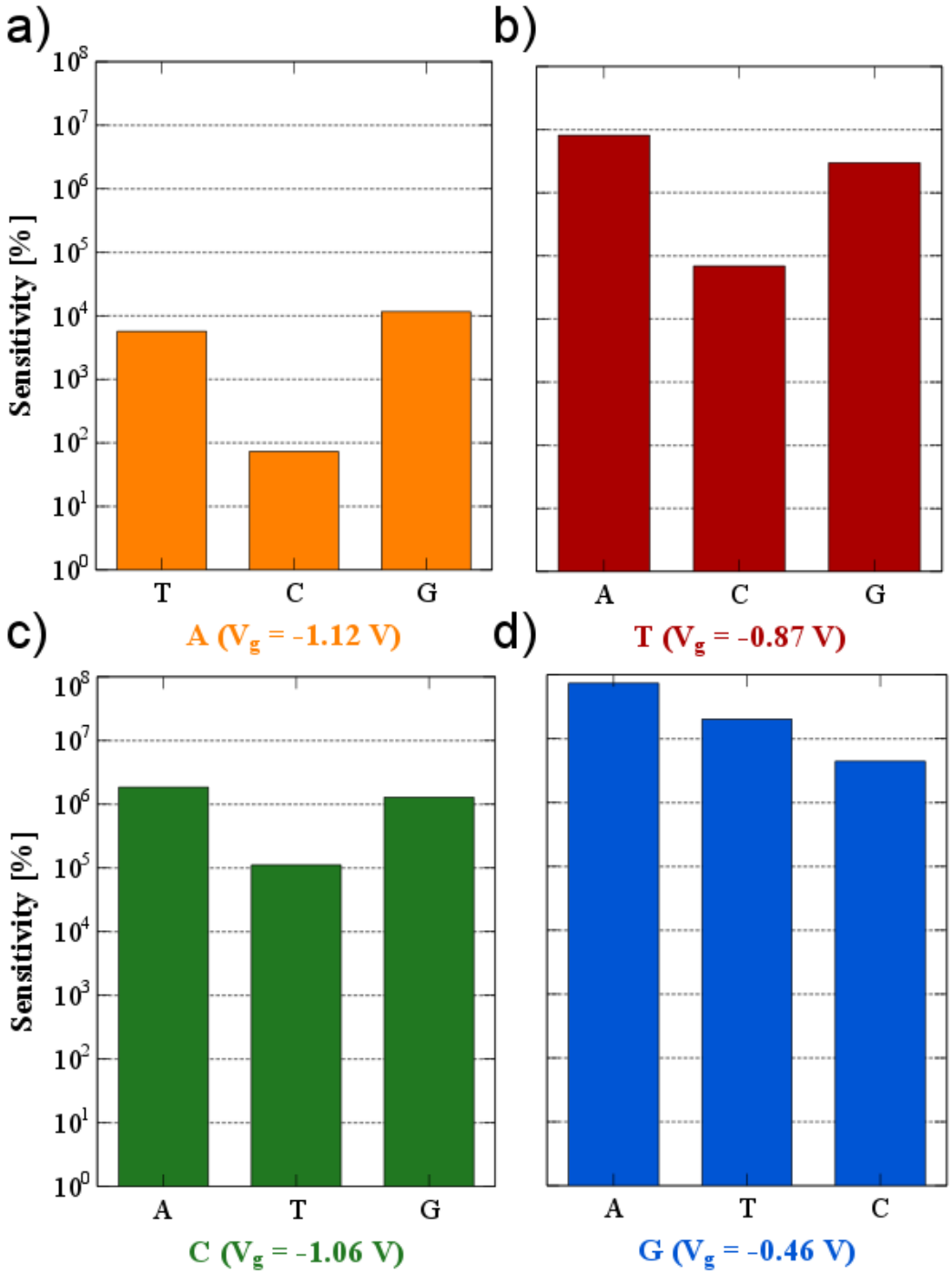

Figure 5.6: The device sensitivity is plotted on a semi-log scale for different gating voltages corresponding to the transmission peaks of the reference nucleotides for the memantine-functionalized device. The labels denote the reference nucleotide and the respective gating voltage.

5.4 Conclusions

In this chapter, we have presented a comparative analysis of diamondoid-functionalized Au(111) electrodes. Specifically, we investigated different diamondoids functionalizing the electrodes between which the four canonical nucleotides are inserted. In these setups, the diamondoids act either as donors or acceptors in their binding to the nucleotides. The choice of the diamondoids is based on the variability in sizes and modifications these can assume. Chemical modification of the electrodes is expected to increase the capture time of the nucleotides in the nanogap due to the formation of the hydrogen bond bridges of the nucleotides with the functionalized electrodes. Stabilizing the DNA within the functionalized gold nanogap is expected to also reduce the noise in the electrical measurements. Note, that stabilization is needed as the DNA is very flexible and is fluctuating in the nanogap. This work, though, has not accounted for these fluctuations as the main focus has been the comparison of different functionalizations of gold nanogaps based on the most prominent hydrogen bond bridges between the nucleotide and the functionalizing diamondoid. It is also expected that the surrounding environment should influence the transmission spectra. This aqueous environment was not considered here, but will be the subject of a separate study. Note, that our work is based on the suggestion that functionalized electrodes [22,23] have a high potential to improve the read-out signal for DNA. Such electrodes can be efficiently embedded in a silicon nitride nanopore. These kinds of nanopores are one among a variety of possible approaches to electrical DNA sequencing.

The electronic transmission of the different diamondoid-functionalized gold nanogaps were compared here. The diamondoid derivative known as 'memantine' has shown a higher nucleobase-specific hydrogen bonding, which lead to a better read-out of the DNA nucleobases with the mem-functionalized device. The sensitivity of such a device was also analyzed and revealed that a careful choice of the functionalizing diamondoid can resolve by up to 8 orders of magnitude a specific nucleotide with respect to the other nucleotides. This is possible as long as the device operates at the respective gating voltage for a given reference nucleotide. This voltage enhances significantly the coupling of the left and right electrodes allowing the generation of a large transverse tunneling current across the nanogap. This strong coupling was found in all devices studied here, whenever the gating voltage corresponds to a transmission peak. It remains to be shown in which way the observations made here will be altered when the memantine-functionalized electrodes are inserted into a nanopore containing a salt solution. Specifically, the longitudinal electric field which drags the DNA through such a

nanopore [115] and the transverse electric field for measuring the transverse tunneling current will introduce additional complex features into the read-out device. These factors should be further probed in order to realize a diamondoid-functionalized nanopore for biosensing applications.

Acknowledgment

Part of this chapter was reproduced from Ref. [116] with permissions from the IOP Publishing.

6 Hybrid Metallic-Semiconductor MoS_2

In this chapter, we move to second sequencing scheme namely, the current modulation sensing. With this aim, we investigate a novel 2D material based on MoS_2. We present the structural, electronic, and electronic transport properties of this material. A point defect analysis gives hints on the electrochemical pore opening in this material. In addition, relevance of our system to nanopore is discussed in Appendix B.

6.1 Introduction

Two-dimensional (2D) materials have attracted high interest in the last years. Starting with graphene and its numerous potential applications, the research of 2D nanomaterials [117, 118] was followed by the intense investigations on 2D transition metal dichalcogenides (TMDs) [119, 120]. TMDs (MX_2, with M=V, Mo, W, etc., and X=S, Se, etc.) are quasi two-dimensional layered materials with strong inter-layer ionic-covalent bonding. 2D TMDs can be found in two phases, semiconducting (2H) and metallic (1T). Liquid-phase exfoliation is the typical method to produce the monolayer TMDs from their layered counterparts [121, 122]. It was shown, that the transition from the 2H to the 1T phase of MoS_2, $MoSe_2$, WS_2, and WSe_2 during their chemical exfoliation depends on the MX_2 composition of these materials [123].

The most famous member of the 2D TMD family is MoS_2, which has been used as a dry lubricant for many decades in its bulk form. In the earlier studies, focus was given on MoS_2-based nanoparticles, such as MoS_2 nested inorganic fullerenes, nanotubes [124], and MoS_2 nanoclusters [125] used as catalysts [126]. The investigations then turned to MoS_2 surfaces [127, 128] and their ability to adsorb hydrogen [129]. The research on MoS_2 has shown a four-fold increase since the year 2010 when the direct bandgap in the single-layered structure was discovered [120, 130]. The coexistence of a metallic and semiconducting phase has been reported in MoS_2 in the past in a number of studies [131–133]. This represents a distinct polymorphism in terms of structural and electronic

properties; a marked deviation from graphene. The coexistence of the semiconducting (2H) and metallic (1T) phase in MoS_2 monolayers has been characterized [134–137]. In principle, gliding only one S plane of MoS_2 to the center of the hexagonal rings of the semiconducting 2H phase will gradually transform the structure to the metallic 1T phase [131]. During this transformation, while the size of the 1T part increases, three different boundaries, α, β, and γ, emerge. The α boundary is related with the Mo-Mo distance shrinking, the β boundary involves the Mo+S gliding, and the γ boundary is based on the S gliding [131]. The recent development of controlled techniques to induce 2H to 1T phase transition [131,138] opens up promising routes for an atomically precise fabrication of single-layered chemically homogeneous electronic devices. Lately, another important achievement in the field was the formation of nanopores in MoS_2 [139]. These nanopores are formed using an electrochemical reaction method [140] and it has been demonstrated that DNA can be translocated through them within a salt solution [141]. These nanopores are efficient in discriminating among DNA nucleotides [142] and can lead to a novel sequencing technique [1,2].

In this study, we focus on hybrid monolayers of MoS_2. The term 'hybrid' refers to the combination of the two different phases (2H and 1T) composing the monolayer. It accounts for the polymorphicity of MoS_2 linking to materials with tunable functionalities. The combination of different phases in constructing the hybrid structures offers additional pathways to electrons and are expected to enhance the electronic transport properties along the hybrid monolayers. This would be relevant to electronics applications, but also for sequencing DNA using a hybrid MoS_2 in which a nanopore can be opened. Within a similar context, the capability of MoS_2 monolayers to act as highly sensitive and selective gas sensors have also been explored experimentally [143–146]. Accordingly, the electronic current confinement on the entrenched 1T MoS_2 nanoroad could make a hybrid MoS_2 device more sensitive to the electronic characteristics of possibly adsorbed biomolecules than the single-phase MoS_2 devices. This article is organized as follows: we first present the methodology used and then proceed to the results on the structural, electronic, and transport properties of hybrid MoS_2 monolayers. Our results also include a point-defect analysis, which reveals the stability characteristics of the hybrid monolayers. In the end, we discuss the implications of our results on novel nano-bio-technological applications of hybrid MoS_2 2D materials.

6.2 Computational Details

Density functional theory (DFT) [58, 59] based simulations as implemented in the code SIESTA [88] were carried out. We have used the generalized gradient approximation of Perdew-Burke-Erzernhof (PBE-GGA) [62], and the norm-conserving Troullier-Martins pseudopotentials [89]. For expanding the Kohn-Sham states, we have considered a double-ζ with polarization basis-set (DZP). An energy shift of 0.01 Ry with a real space sampling grid (mesh cutoff) of 200 Ry, and $10 \times 1 \times 12$ k-points within the Monkhorst-Pack scheme were used. This mesh was found suitable for the smallest unit in Fig.6.1a. The geometry relaxations were performed until the net forces of each atomic component become smaller than 0.01 eV/Å. The electronic transport calculations are performed using DFT combined with the non-equilibrium Green's functions (NEGF) formalism, as implemented in TranSIESTA [76].

We have first carried out benchmark calculations separately on both the pristine metallic and semiconducting phases of MoS_2. For the pristine 1T phase the lattice parameter of 3.23 Å and the Mo-S bond-length of 2.47 Å were found. Note that since the pristine free-standing 1T phase is not very stable, there are no experimental data to compare to. We also find that 2H MoS_2 is a semiconductor with a direct bandgap, a lattice constant, and a Mo-S bond-length of 1.64 eV, 3.23 Å, and 2.45 Å , respectively. These values are in a very good agreement with previous theoretical results [147–149].

In this work, we study a monolayer hybrid MoS_2 structure, which combines both the 1T (metallic) and the 2H (semiconducting) phase of MoS_2. More specifically, a 1T phase is embedded in the 2H phase as evident from Fig.6.1e. In order to investigate the electronic properties of the hybrid MoS_2 system we have considered different supercell sizes. The different unit-cells used to generate these super-cells are shown in Fig.6.1a-d. These correspond to 36, 48, 60, and 66 atoms per unit cell, respectively. By going from the 36 up to 66 atoms unit cell system, the width of the embedded 1T nanoribbon is increased from 4.7 Å to 20.5 Å. A kgrid of $60 \times 1 \times 90$ was used for the Monkorst-pack sampling of the density of states.

The setup for the transport calculations across the hybrid MoS_2 monolayer is shown in Fig.6.1e. The hybrid MoS_2 device is composed of the two electrodes (left and right) and the scattering region (device). Both parts, the leads and the scattering region are hybrid, meaning that these are composed of both the 1T and 2H phases. With this setup, the electronic transport occurs along the 1T ribbon. The structure shown in Fig.6.1d was relaxed further up to a force tolerance of 0.001 eV/Å. The resulting relaxed structure

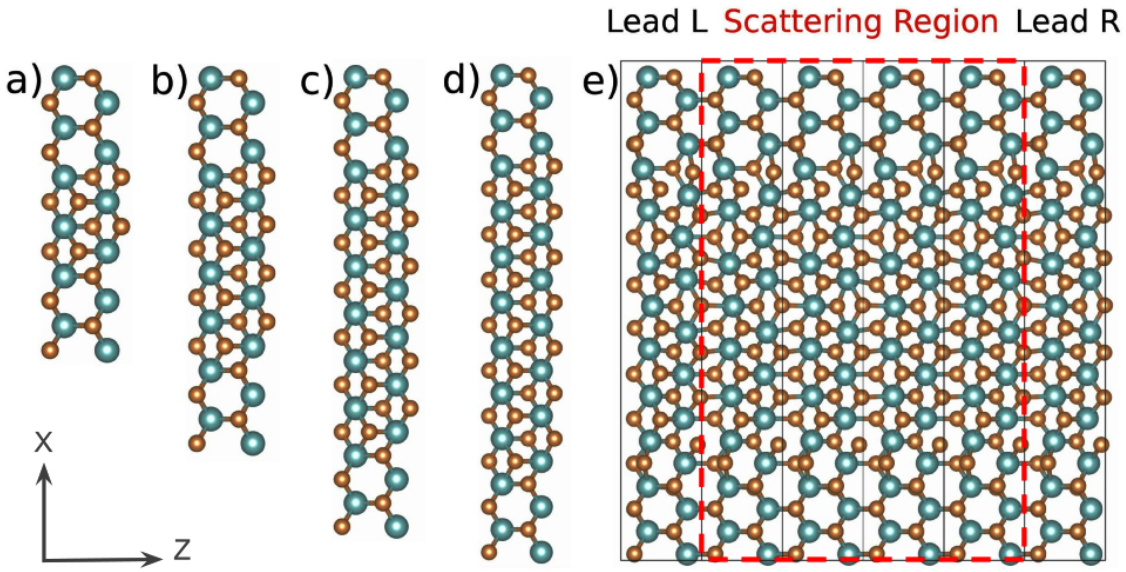

Figure 6.1: Hybrid MoS_2 structures for different widths of the metallic 1T ribbons. Four different unit cells were modelled: a) a 36 atom unit cell with 1 unit of 1T embedded into 2H, b) a 48 atom unit cell with 3 units of 1T embedded in 2H, c) a 60 atom unit cell with 5 units of 1T embedded in 2H, d) a 66 atom unit cell with 6 units of 1T embedded in 2H. In e) the transport setup is depicted. Both the leads and the scattering region of the device are shown. The leads are build from a single unit cell of 66 atoms in a structure based on that as shown in panel d) but with relaxation of the atoms included. The scattering region is composed of 4 repeated unit cells each containing 66 atoms, in the same structure as in the leads. The electronic transport occurs along the z-direction. The S atoms are shown in brown and the Mo atoms in cyan. The same color coding will be used in the following.

formed the lead for the transport set up. The device region was generated by replicating four units of the leads along the z-direction. Finally, the transmission was computed by coupling the device to semi-infinite leads. Due to the large size of the system, the Brillouin zone sampling was restricted to the Γ-point. For the transport calculations, finite structures rather than periodic supercells were considered.

6.3 Results and Discussion

6.3.1 Structural Characteristics and Defect Analysis

We have initially considered a hybrid structure with zig-zag edges along the interface (Fig. 6.2). In this case, the fully relaxed atomic structure led to buckling, in agreement with previous results [150]. Note, that this buckling did not lead to any significant induced curvature outwards or inwards the hybrid structure. Theoretical studies have shown that neither the armchair [151] or the zigzag [137] interfaces in hybrid MoS_2 show out-of-plane distortion. Nevertheless, our findings demonstrate that the armchair interface does not show inflection, but is the most stable against buckling. Accordingly, the armchair interface will be the one considered herein (Fig. 6.1). We begin our analysis with the structural details of the hybrid MoS_2 monolayers. Representative fully relaxed structures with varying 1T regions are shown in Fig.6.3. Inspection of the side view of these reveals a planar system in which distorted bonds due to the interface are evident. From a structural point of view, it is clearly visible from the top views in Fig.6.3 that the interfaces are armchair-like and not symmetric.

Hence, we chose a non symmetric interface, which did not lead to buckling consistent with the experimentally stable structures [135]. In order to generate this interface, the β- and γ-phases of the interface were shifted by one unit cell in the 'bottom' interface with respect to the 'top' one ('bottom' and 'top' refer to the interfaces clearly seen in Fig.6.1) [151]. From Fig.6.3 it was verified that the 2H phase does not change, whereas the 1T phase presents a structural distortion induced by the interface. Each of the 1T phases contains a Mo-Mo trimer unit. In the pristine 1T phase, all of the Mo-Mo distances are equal to the lattice constant. In our hybrid model, the observed distortion in the 1T region (for all 1T sizes modeled here) can be quantified by the Mo-Mo distance shortening along two of the Mo-Mo distance. These distances are in the range of 2.75 Å to 2.85 Å . The third Mo-Mo distance remains undistorted and its values are close

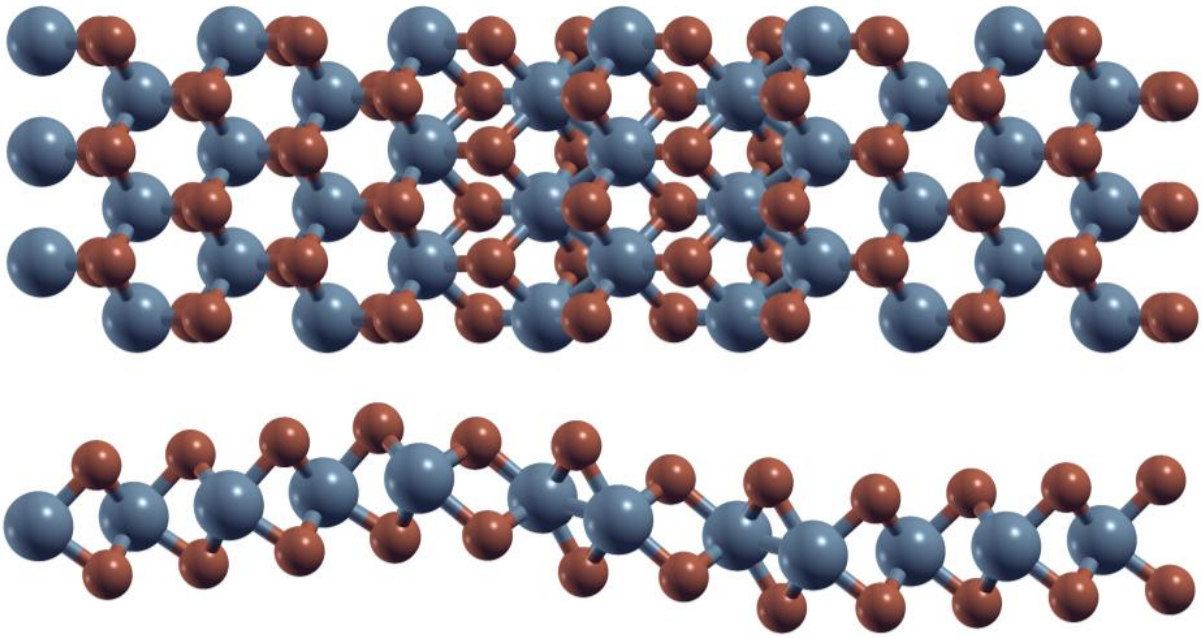

Figure 6.2: Hybrid MoS_2 with zig-zag edges along interface after structural relaxation.*Top panel:* the in-plane view of the monolayer. *Bottom panel:* side view of the structure. Out of plane buckling is clearly visible in the view.

to the lattice parameter (3.15 Å). Similar experimental results have been reported a Mo-Mo distance of 2.9 Å [133, 152]. Such a partial distortion in the Mo-Mo trimer unit of 1T remains as the number of 1T units increases. This can be confirmed also for the smallest unit cell taken (36 atoms/unit cell in Fig.6.1a) in which the 1T region is very thin and equal to about 4.7 Å. Further inspection of this in Fig.6.3 reveals the atomically sharp interface in conjunction to the experiments [135]. It is worth noting that no atom loss or affluence was observed in our hybrid monolayers, in accordance with previous theoretical investigation [137].

In order to study the energetic stability of the hybrid system model, we have calculated the formation energy of single sulfur vacancies. Aiming to identify the regions which are energetically more favorable to form vacancies, we move along a sulfur line across the armchair interface of the monolayer as shown in Fig.6.4 and remove one sulfur atom (labeled and pointed by the arrows in the figure) leaving the monolayer with a single vacancy. The stability is cast in form of the formation energy of the single point sulfur defect in the monolayer. The calculation of the formation energy, E_{form}, for a single sulfur vacancy in hybrid MoS_2 is based on the comparison of the total energies of the monolayers with and without the vacancy on the chemical potential of a single sulfur

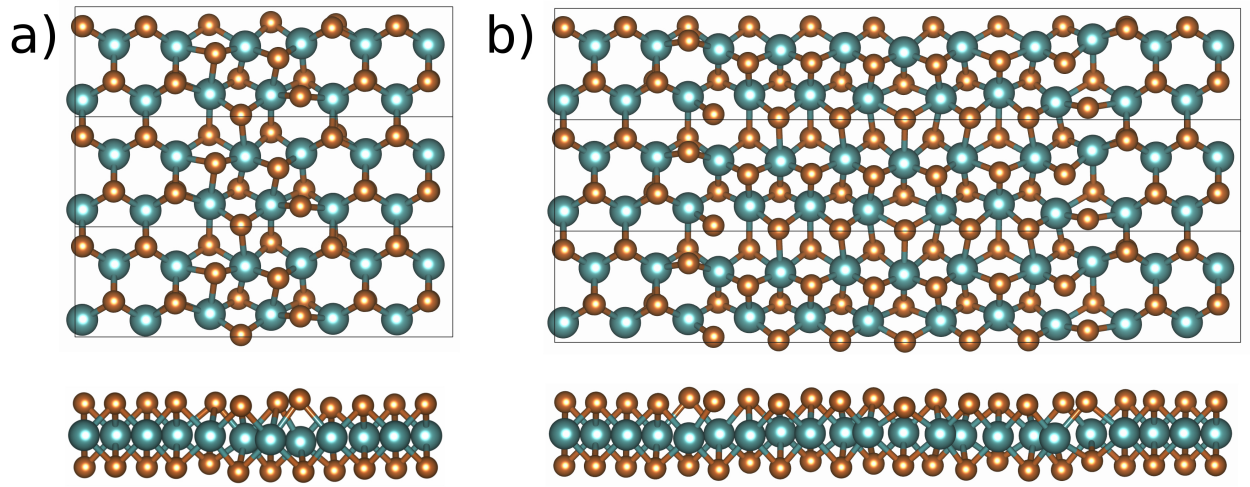

Figure 6.3: Relaxed structures of the hybrid MoS_2 monolayer for the smallest and largest unit cells from Fig. 6.1(a,d). The upper panels show top views, while the lower panels shows a side views of the relaxed structures. The gray rectangular regions in the top panel indicate the three periodic unit cells in the structures.

atom as calculated through our simulations. Accordingly, the formation energy is given through

$$E_{form} = E_{defect} + \mu_s - E_{pristine} \tag{6.1}$$

where E_{defect} is the total energy of the system with a single sulfur vacancy, $E_{pristine}$ is the total energy of the pristine monolayer, and μ_s is the chemical potential of S atoms. The μ_s is obtained from the stable S_8 ring, which is very similar to the bulk value of μ_s [153]. The sulphur vacancy formation is an endothermic process, meaning that the more positive the formation energy, the more unlikely the formation of the vacancy. The relative magnitudes of the thus calculated defect formation energies are shown in Fig.6.4. The formation energy has its smallest value when sulfur atom number 9 is removed from the monolayer. This S atom is located at the interface region. The variation in single vacancy formation energy exhibits another local minimum corresponding to the removal of sulfur atom number 5 slightly further away from the interface. This removal corresponds to a defect formation energy which is about 0.5 eV higher than that for atom number 9 at the interface mentioned above.

It is worth stressing that we have also investigated the sequential removal of sulfur atoms along the two semiconductor-metallic interfaces in the hybrid MoS_2 shown in Fig.6.4. The results (not shown) confirm that most of these sulfur atoms have a defect formation energy of about 1 eV similar to the lowest energy in Fig.6.4 denoting that indeed the interface atoms should be easier to remove. Note, that we have only investigated the removal of sulfur atoms since the formation energy of a molybdenum vacancy is expected

to be much larger (by 4 eV) than to that for sulfur [154].

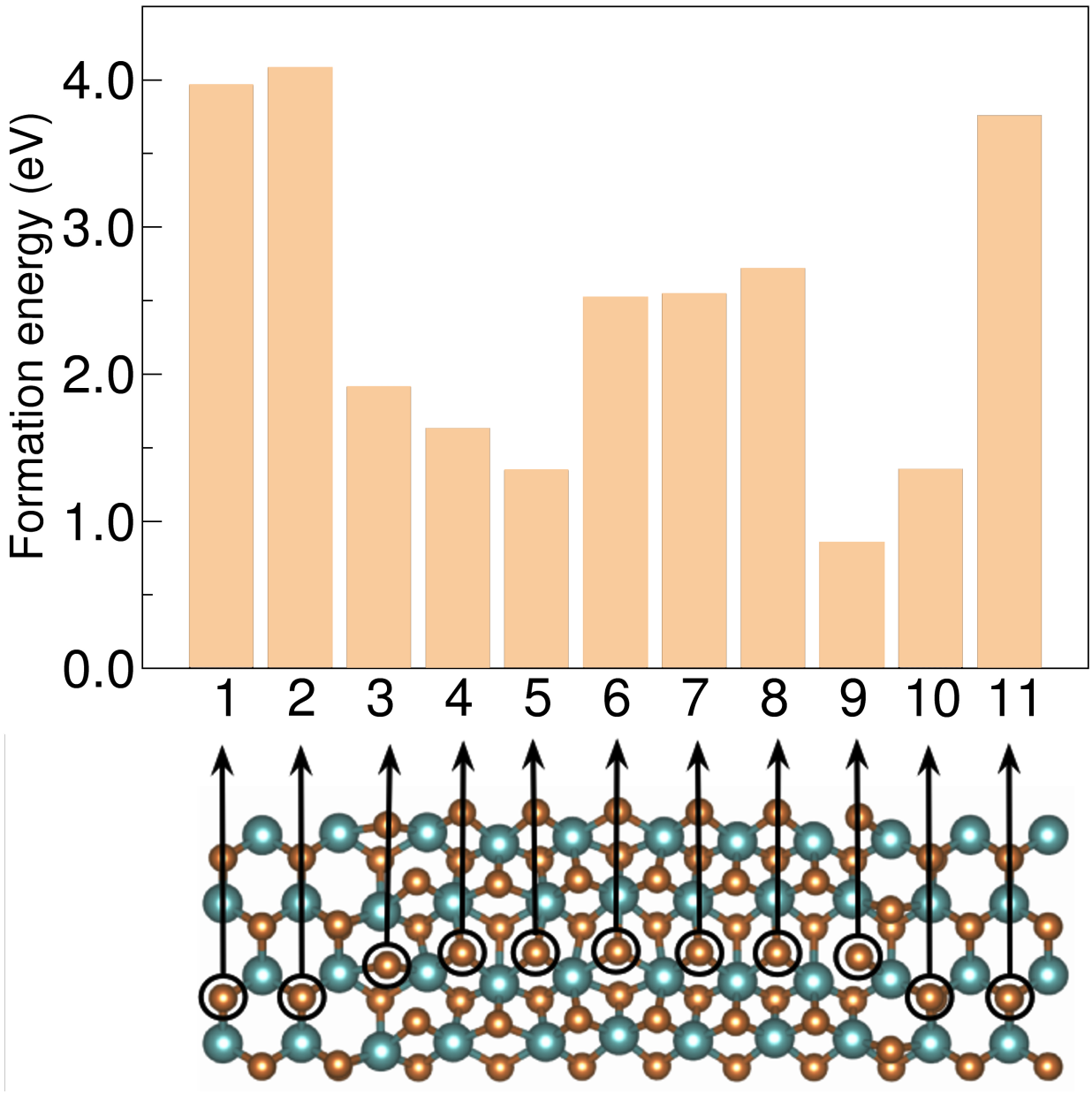

Figure 6.4: Single vacancy formation energies (E_{form}) of sulfur sites located along a vertical line crossing the 66 atom unit cell system . Each bar in the graph gives the formation energy of a single S defect for the corresponding S atoms from the string of encircled atoms below, as denoted by the respective arrow.

6.3.2 Electronic Properties

The precise fabrication of electronic devices built from hybrid materials such as the 1T/2H MoS_2 monolayer consider here [131, 138] requires a deep understanding of how

the electronic structure could be affected by changing the size, as well as the shape of the 2H and 1T domains in the MoS_2 heterostructure. We have therefore investigated the influence of the width of the embedded 1T-MoS_2 on the electronic properties of the hybrid monolayer. Through the analysis of the electronic density of states (DOS) (shown only for the largest width - see Fig.6.5), we find that for all the different widths of the 1T ribbon considered here, the hybrid monolayer shows a metallic behavior.

The total electronic DOS of the largest hybrid MoS_2 considered here (see Fig.6.3b) is depicted in Fig.6.5a. Results are shown only for this structure, as the relevant properties for the smaller structures are qualitatively similar. The top and bottom panels of this graph also display the projected and partial DOS (PDOS) of the same system. From Fig.6.5a it can be seen that in the vicinity of the Fermi level the largest contribution comes from the 1T phase. In addition, a comparison of the Mo and S contributions reveals that in both phases, the largest contribution originates from the Mo rather than the S atoms. Regarding the different orbital contributions to the electronic structure, it is known from the literature that in 2H MoS_2 both valence and conducting bands are mainly dominated by the $4d$ states of Mo with a slight contribution from the $3p$ states of S [155]. For the single-phase metallic 1T-MoS_2, the $4d$ states of Mo and the $3p$ states of S contribute to the electronic states in the vicinity of the Fermi level [155]. The projected DOS decomposition with respect to the $3p$ and $4d$ orbitals of the S and Mo atoms in the upper graph of Fig.6.5a corroborate with previous observations. Indeed, around the Fermi level (from -0.5 to $+0.5$ eV) the $4d$ orbitals of Mo and the $3p$ orbitals of S from the 1T part of the monolayer dominate. The respective orbitals of the 2H phase become more important further away from the Fermi level and are connected to the bandgap edges of this phase.

An additional important feature is related to the interface. As mentioned previously, by construction, the interfaces between the 2H and 1T phases in our hybrid MoS_2 model are not symmetric. This asymmetry prompted us to investigate the partial DOS (PDOS) and the contributions of the Mo and S atoms of the 1T and 2H phases close to both interfaces. The different atoms/regions included in the analysis are shown in Fig.6.5b. The hybrid structure is divided into three regions, the 2H phase, the top 1T, and the bottom 1T phase. The partial DOS of the Mo and S atoms in the different parts of the hybrid monolayer on both sides of the two interfaces are given in the lower panel of Fig.6.5a. It becomes clear that atoms from the 'top' and 'down' part of the 1T ribbon make different contributions to the total DOS. From this figure, we note that the 'down' part of the 1T region contributes more to the total DOS than the 'top' part of 1T close to the Fermi level, a clear confirmation of the interface asymmetry. The contributions of

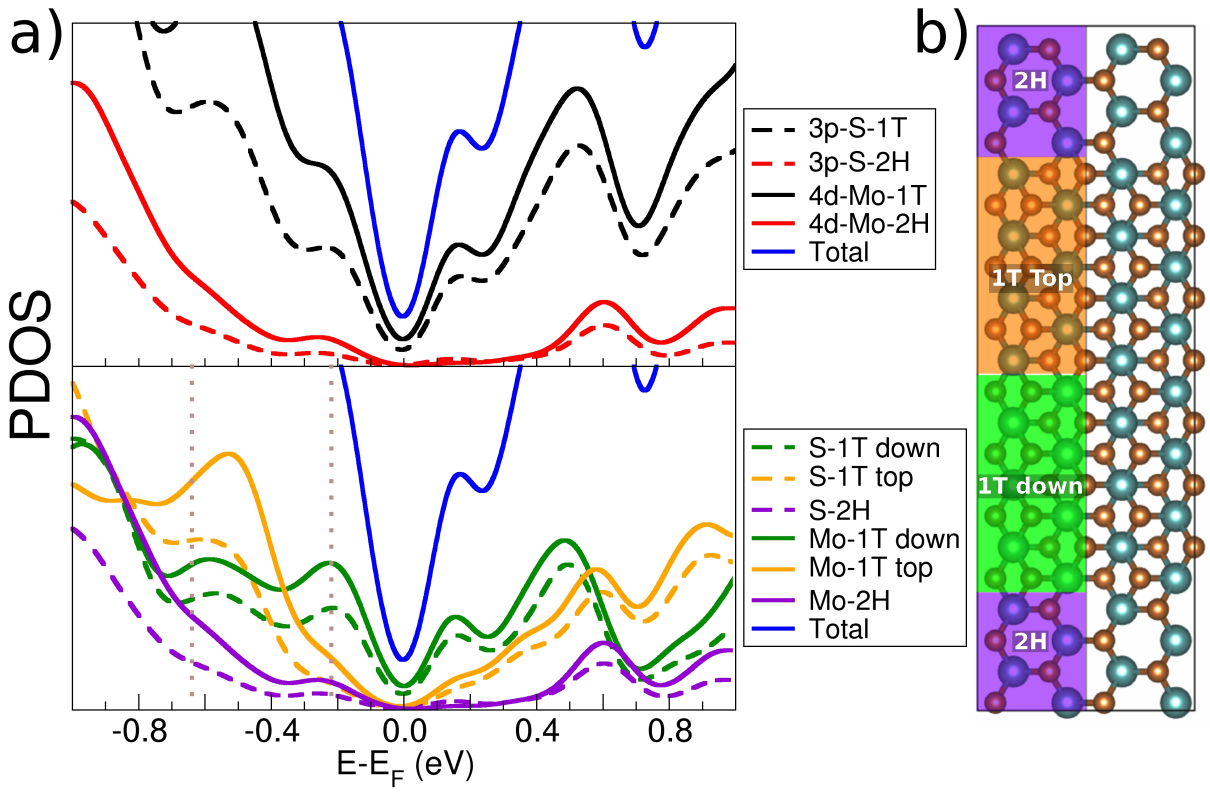

Figure 6.5: Density of states of the largest relaxed structure (66 atoms/unit cell) from Fig.6.1d. In (a) The upper graph shows the total DOS and the projected DOS with the contributions from the 3p states in S and the 4d states in Mo in both 1T and 2H phases in the hybrid MoS_2. In the lower graph the partial DOS based on the contributions of the S and Mo atoms of the 2H and 1T phases close to the two ('top' and 'down') interfaces are given. The legends correspond to the structure in b), which shows two unit cells of the largest structure in Fig.6.1d. The two dotted vertical lines in the lower graph indicate the energy interval (from -0.64 eV to -0.22 eV) used for the analysis of the local currents in Section 6.3.3. In all cases, the Fermi level (E_F) is aligned with zero on the energy axis

the Mo atoms in all parts of the system are higher than those from S, as expected. It is also clear, that more states are associated with both Mo and S atoms of the 'down' 1T part than in the case of the 'top' 1T part. In view of the transport properties , which we will discuss next, this feature would relate to additional electronic pathways for the movement of electrons along the 'down' interface of the material compared to the 'top' interface.

6.3.3 Electronic Transport

We next turn to the calculation of the electronic transport along the hybrid MoS_2 monolayer. Previous theoretical studies only considered the coexistence of the 1T and 2H phases within the same monolayer [135, 137]. But did not investigate a single 1T ribbon embedded in the 2H phase which is more closely resembling the situation in experimental studies [131] that aim for the realization of electronic transport devices. In fact, the periodic boundary conditions used in the DFT calculations induce a potential repeating across the periodic images of the hybrid MoS_2 structure. Within the transport simulations, no such periodicity is assumed. Accordingly, the DOS from the transport calculations reveals a small gap unlike the results from the periodic DFT simulations.

For the structure in Fig.6.1e, the calculated electronic transmission curves are drawn in Fig.6.6a. No transmission of the electronic current is observed for the interval of about ± 0.1 eV around the Fermi level, consistent with the gap in the total DOS in Fig.6.6b. The transport calculations were performed also by considering leads and scattering region larger than the ones shown in Fig.6.1e and have led to similar results. This successful convergence test shows that the results presented here do not change when the electrode would be made larger, as in a typical hybrid MoS_2 electronic device. Overall, the transmission profile close to the Fermi level, is well structured, having many peaks denoting a large transmission at the respective energies. In the inset of Fig.6.6a the transmission curves for the single-phase MoS_2, both the 1T and the 2H, are given for comparison. A clear metallic behavior for the 1T phase is shown, while the 2H phase shows zero transmission between roughly -1.0 to 1.0 eV. The transmission function of the hybrid MoS_2 shows a stepwise behavior indicating a ballistic transport. Although the transmission of single-phase MoS_2 shows a smoother behavior, the system is also ballistic. In the simulations, increasing the number of k-points perpendicular to the transport direction, lead to a decrease of the transmission steps became until these reached the limit of the smooth curve. The length of the scattering region along the transport direction for the systems

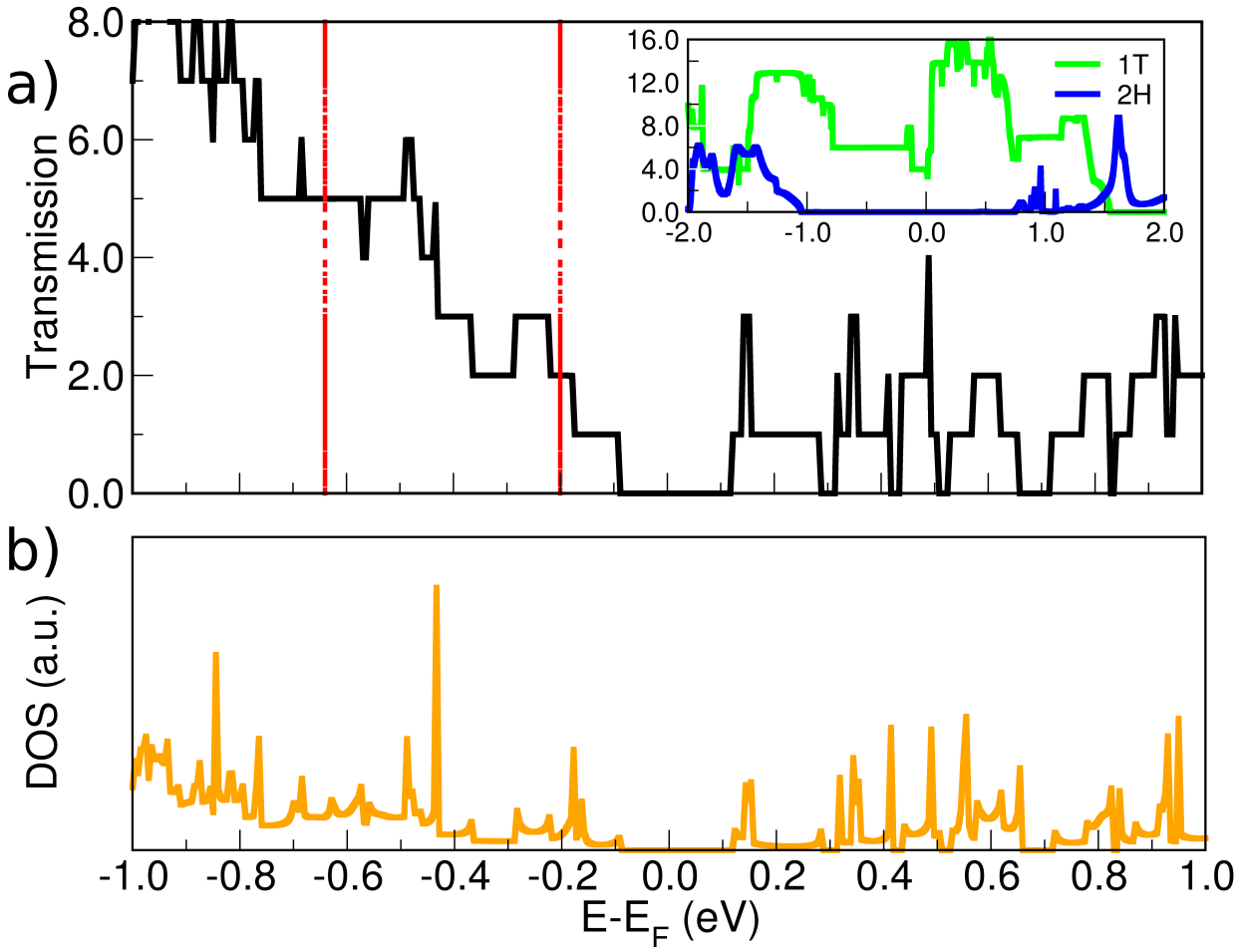

Figure 6.6: (a) The transmission spectra for the hybrid monolayer of Fig.6.1e. The vertical dotted lines at -0.64 eV and -0.22 eV correspond to the energies used in the analysis of the wavefunctions and the local currents below. The inset plots the transmission as a function of energy (in units of eV) for the single-phase 1T and 2H MoS_2 monolayer. (b) The total DOS for the same material. All data shown in this figure were obtained from the NEGF calculations.

studied here is much smaller ($\approx$ 22Å) than the electron mean free path in MoS_2 [156]. Accordingly, one might expect a ballistic transport for these systems. A similar behavior would be expected even if the device length would be increased by several factors.Note, that the gap in the hybrid case is much smaller than in the 1T case. Similar to the small DOS discrepancy between the periodic and the finite structures in Fig.6.5 and Fig.6.6b, this might indicate that in the limit of a large width of the 1T phase, the gap in the transmission $T(E)$ might close.

In order to understand the transmission curves in Fig.6.6a and unveil the microscopic mechanism behind them, the local currents transmitted across the hybrid system are visualized for the energy values -0.64 eV (Fig.6.7a) and -0.22 eV (Fig.6.7b) . The local

currents at zero bias essentially map the transmittance projection between two sites and can be obtained from the non-equilibrium Greens functions and the transmission using a Keldysh formalism [76]. Details on the full derivation of the local currents are described elsewhere [104,109]. Comparison of the two energy values reveals a qualitative difference in the electronic transmission across the hybrid MoS_2. The energy value of -0.64 eV corresponds to a higher transmission than at -0.22 eV (referring to the dotted lines in Fig.6.6a). The corresponding local currents for these two energies show also different characteristics. Interestingly, current is not flowing along the whole 1T region as was expected. The local currents are rather associated with specific parts in the 1T ribbon. Fig.6.7a shows a significant current across the top interface and the top half of the 1T region. The amount of local currents is less on the lower part of the 1T phase. This is confirmed by the zero bias scattering state eigenchannel wavefunctions (EWFs) (not shown). These wavefunctions are not equally spread across the metallic region along the transport direction. At this energy, the different signs of the EWFs on the bottom 1T part cancel out, so that there is only a small amount of local current in this region. At -0.64 eV, there is current flowing across a different part of the metallic phase in the hybrid system compared to the case at -0.22 eV. There is more current flowing across the upper half of the metallic region and less current in the lower part at -0.64 eV. At -0.22 eV (Fig.6.7b), the EWFs are spread out across the lower part of the 1T material and the bottom interface supporting the finding that local currents are found at the bottom interface. The results indicate that at both energies, both Mo and S atoms are involved in promoting the flow of the electrons and that electron motion is indeed associated mainly with the metallic region and the interface, while the 2H phase does virtually not participate. Note, that we have chosen two energy values which link the electronic properties shown in Fig.6.5 to the asymmetry in the structure and transport properties in Fig.6.7 and the EWFs. Other energies should lead to different contributions in these properties.

One can observe that by construction the bottom and the top interface are not symmetric to each other (see Figs.6.1, 6.5b) as mentioned in the section on the structural characteristics of the hybrid MoS_2. Accordingly, depending on the energy, only one of the two interfaces is strongly related to the transport. Across that interface, a layer of Mo and S atoms from the 2H region are involved in the transport. This is evident from the local currents. Nevertheless, we have observed that the energy (or gating voltage) controls which parts of the metallic regions are involved in the transmission. As a way to unveil the mechanism which leads to a transmission along part of the metallic region, we turn again to the partial DOS in the lower graph of Fig.6.5a. Due to the asymmetry of the interface the 'down' part of the 1T ribbon has shown a larger contribution to the PDOS

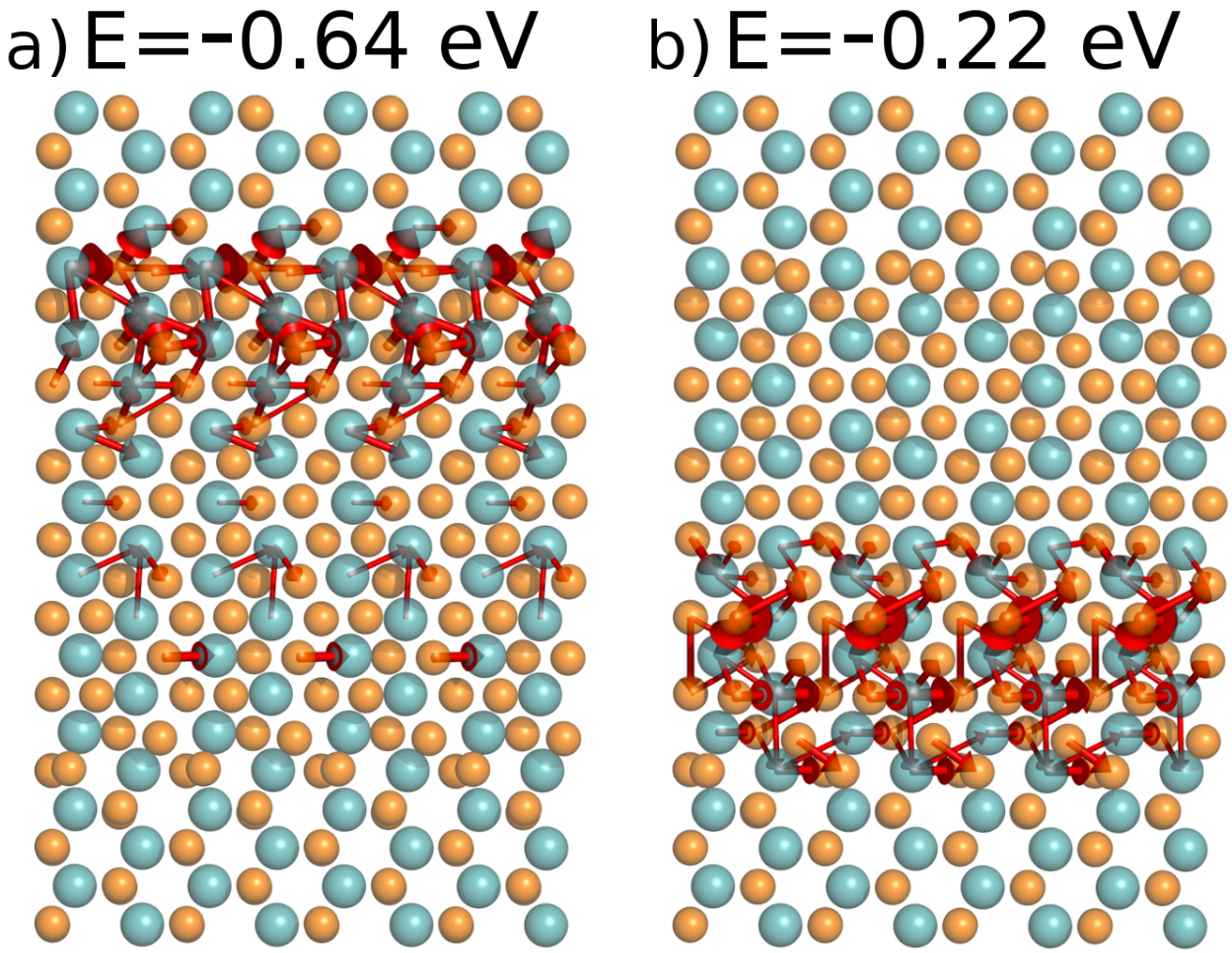

Figure 6.7: Local currents for the setup shown in Fig. 6.1e are depicted. The results are shown for two energies corresponding to the vicinity of transmission peaks (see Fig.6.6a) at -0.64 eV (left panel) and -0.22 eV (right panel).

close to the Fermi level than the 'top' 1T part (green and orange lines in the lower graph in Fig.6.5a. This observation can explain the non-homogeneous current flow through the 1T ribbon. In addition, the higher DOS at -0.64 eV compared to -0.22 eV justifies why the currents are localized in the upper 1T part in the former case and the lower 1T part in the latter case as visualized in Fig.6.7. Nevertheless, on the interface at each energy value a current accumulation due to interface states has been observed. This analysis shows the strong dependence of the electron transport along the hybrid MoS_2 monolayer on its PDOS and the available electronic states at different parts of the material. Accordingly, these results suggest that a careful design of the hybrid interface would selectively tune the electronic transport along the hybrid monolayer and control which part of the embedded ribbon is involved in the transmission. Such a design would link to the exact experimental gating voltages leading to the desired transmission pattern.

6.4 Summary

In this work, we have probed the structural, electronic, and transport properties, as well as the stability of hybrid MoS_2 monolayers. These hybrid systems are composed of a 1T metallic ribbon embedded in the 2H MoS_2 phase forming an interface with armchair edges. We have varied the size of the embedded metallic ribbon in order to assess its influence on the properties of the hybrid system and have obtained converged properties. We have observed the formation of a stable, planar interface which includes atomic sites of different stabilities. Following a single sulfur vacancy analysis along the heterostructure, we have identified the unstable regions of the hybrid system, which are located at the armchair interface. The electronic properties of the hybrid monolayer showed a clear metallic character, as the 1T part of the heterostructure introduces states in the electronic bandgap of the 2H region. Clear electronic transmission signals across the structure, which become negligible very close to the Fermi energy have been observed and are attributed to the finite structures in the calculations. Extrapolation to a large periodic hybrid MoS_2 is expected to promote electron transmission also close to the Fermi level. Visualization of the local currents at different energies clearly manifest the flow of electrons across the metallic part and the interface of the material. The exact features vary with the exact energy value and the asymmetry of the interface. The local currents have verified the strong influence of interface states on the transmission spectra.

Interpretation of our results in view of the current high interest on 2D MoS_2 and in general on TMD structures would lead to 2D materials with tunable properties. This

would be a special feature of 2D TMDs as opposed to graphene. Specifically, the variable properties of hybrid MoS_2 would allow for a selective design of electronic devices as controlling the interface between the semiconducting and the embedded metallic phase would lead to a modulation of the transmitted current. Tuning the interface would control not only the amount of current flowing along a device, but also the part of the device that is conducting. A further thorough investigation of this polymorphicity, as proposed through our work, would lead to new materials and novel applications in nanoelectronics well beyond those based on graphene. Specifically, our point defect investigation is highly relevant to the nanopore formation using an electrochemical reaction process in MoS_2 nanopores and the subsequent detection of translocating DNA [142]. Within this concept, our analysis provides a deeper understanding on the earliest stages of the nanopore formation process and a a qualitative insight at the direction of pore growth. The results denote, that in order to begin a pore opening process in a hybrid MoS_2 monolayer, first a sulfur atom at the interface needs to be missing. Using then an electrochemical reaction process the pore opening can be initiated in the neighborhood of the single point defect. We conclude that based on our results, the pore growth is therefore likely to start at the interface and move favorably in the direction of the 1T phase/interface rather than towards the 2H phase. A first view of the Hybrid MoS_2 based nanopore (Fig. B.1) generated along these lines can be seen in Appendix B. Accordingly, our work provides important insights regarding the pathways for selectively opening a nanopore in hybrid MoS_2 leading to properties superior to those of single-phase MoS_2. These results are expected to have a large impact on the fabrication of novel nanopores, biosensors, and tunable electronic devices.

Acknowledgment

Reproduced with permission from [56]. Copyright [2016] American Chemical Society.

Part IV

Conclusions

7 Summary and Outlook

The field of nanopore sequencing has evolved rapidly over the last three decades. The first sequencers based on biological nanopores are commercially available now. Starting from the beginning of last decade, attempts have been made to take advantage of the huge progress achieved in the semiconductor process technologies. This has resulted in the development of sequencing techniques based on solid state substrates and sensing schemes beyond ionic current. However, miniaturization of such sensing schemes leads to difficulties in the spatial confinement of translocating molecule in the vicinity of the sensors and the nature of sensed signal itself subject to quantum mechanical effects. This thesis aims to take on the aforementioned challenges from a computational modeling perspective.

The main goal of this thesis was to improve the reading out features of nanopores by using transverse electronic transport calculations. This was divided in to two parts. In the first part, detection was made through tunneling sequencing scheme, while in the second part a current modulation scheme is proposed for the detection of the nucleobases. Our proposal is a novel 2D material based on MoS_2. The electronic transport was modeled by the non-equilibrium Green's function (NEGF) method coupled to density functional theory. In addition, the electronic structure calculation were performed using density functional theory (DFT).

Tunneling sequencing involves reading out the DNA sequencing by means of metal electrodes embedded in the nanopore as the biomolecules translocated through the pore. The main challenges of the tunneling sequencing scheme is to improve the electronic coupling between the translocating molecule and the metal electrodes. The experimentally accessible tunneling current amplitudes show broad overlapping distribution, possibly arising from large number of molecular conformation in the nanogap. Diamondoids are a family of diamond caged molecules with hydrogen terminations. A large number of chemical derivatives of diamondoids are also available, along with excellent stability, and tunable electronic properties, making them ideal for nanotechnology applications. Our proposal in this thesis is to modify the metal electrode (via thiol group)

with derivatives of diamondoid molecules. These molecules can form hydrogen bond bridge with DNA nucleobases. The investigation in itself is divided into two steps. The first step involves an investigation at the level of DFT to unravel the interaction of isolated diamondoid derivatives with nucleobases. The hydrogen bonded complexes formed between three nitrogen doped derivatives of amantadine with the four pristine, one methylated, and one mutated nucleobases were investigated. The calculated interaction energies were found to be of moderate strength, ideal for hydrogen bond bridge. In addition, we also looked at the variation of hydrogen bonding subject to translation and rotation along a reference axis. Finally, a qualitative analysis of electronic band gap was presented to access the sensing potential of such molecules. The second step consisting of investigating the electronic transport across single (diamondoid) functionalized gold electrodes. The second step was performed in line with the isolated molecules chosen in the first step. The calculated transmission curve, revealed that each of the nucleotides has a distinct resonance peak below the Fermi level. We suggested a gating sensing scheme to sample these distinct peak for the purpose of sensing. Consequently the concept of device sensitivity was introduced to compare the effectiveness of the device at a reference gating voltage in distinguishing the nucleotide's. The device sensitivity plots in turn revealed a clear pathway in discriminating the pristine nucleotides, methylation, and mutation. Comparison of the device sensitivity for three difference diamondoid functionalization revealed memantine to be the best functionalizing molecule. In the next step, We will investigate electronic transport across double (memantine) functionalized gold electrodes devices. This will unravel the effect of a second functionalization i.e. the backbone grabber memantine electrode, towards discriminating the DNA nucleotides. Issues such as a conformation scan, the influence of environment (water and ions) etc. have not been investigated in this thesis. To tackle these issues, *ab initio* molecular dynamics simulations of double functionalized devices interacting with short polynucleotides along with the environment are expected to be performed in further steps.

In the second part, we turned out attention to sensing scheme beyond electron tunneling. We investigated 2D material beyond graphene, that can be a potential current modulation sensor for DNA. The availability of structural polymorphism, and hydrophilic nature of MoS_2 made it an ideal candidate. For this purpose a hybrid monolayer consisting of metallic 1T-MoS_2 embedded in semi-conducting 2H-MoS_2 was chosen. The structural, interface (i.e. separating metal and semiconducting regions), electronic, and point defect formation in this hybrid monolayer was investigated. Structural relaxation revealed that the non-symmetric armchair interface to be stable, and distortion in the Mo-Mo dis-

tances in the metallic region. Electronic transport calculations further revealed that the non-symmetric nature of interface leads to asymmetry in the current flow across the two interfaces by means of gating. The point defect analysis gave further hints to the initiation of pore opening by electrochemical reaction. Further, a first view of the hybrid MoS_2 based nanopore (Fig. B.1) is discussed in Appendix B. We have provided a preliminary discussion on a nanopore opening on a hybrid MoS_2 monolayer. A number of dangling bond were observed on the pore edges. Work is under progress to chemically passivate the pore edges. Different chemical groups will be considered for the passivation. Analysis will be performed to understand their effects on the stability, and electronic property of the nanopore. Once the nanopore formation, and edge passivation are characterized, topics such as DNA sensing, conformation scan, inclusion of water and ions etc. are expected to be taken up further.

Part V

Appendix

A Diamondoid Functionalised Devices

The projected density of states (PDOS) as computed through the DFT-NEGF formalism are discussed in this appendix. Focus is given on the shaded energy interval [-1.40,-0.75] eV (Fig. 4.3 in Chapter 4), which should be relevant for experiments. The calculations were performed using the *Inelastica* package [157]. All the PDOS curves have been plotted in the top panels of Fig. A.1a-A.1d corresponding to each nucleotide within the amantadine functionalized electrodes (Fig. 4.1b). The transmission curves have been reproduced in the bottom panels in these figures. The PDOS has been decomposed into the electronic contributions coming from the diamondoid ('ama'), the nucleotides (A, T, C, G), and the gold ('Au'). As observed in Fig. 4.3, all transmission curves show a resonance peak (in the energy interval) for each nucleotide. For example, in the case of A (Fig. A.1a) the resonance peak in the transmission curve is clearly complemented by an increase in PDOS occupancy at exactly the same energy (-0.98 eV). Inspection of all PDOS curves reveal that the resonance peak in the transmission curves arises from the nucleotide contribution. The other components of the 'ama' and 'Au', do not show the same behavior in all the cases.

In Chapter 4), we had observed that T has a smaller resonance peak compared to all the other nucleotides. On analyzing the PDOS curve (Fig. A.1b), it can be observed that there is an increase in contribution from the T component at -1.26 eV. But this is significantly lower in PDOS occupancy in comparison to other nucleotide cases, resulting in a smaller resonance peak in the transmission curve for T. The bulk of the contribution towards the transmission curve in the energy range seems to be arising from the contribution of 'ama' component. In all the other cases, the nucleotide component seems to be the highest contributor towards the PDOS at their respective resonance peaks. Notice that for C (Fig. A.1c), there are two distinct resonance peaks in the energy interval. For the analysis purpose the peak with larger transmission value (i.e. at -1.3eV) was chosen.

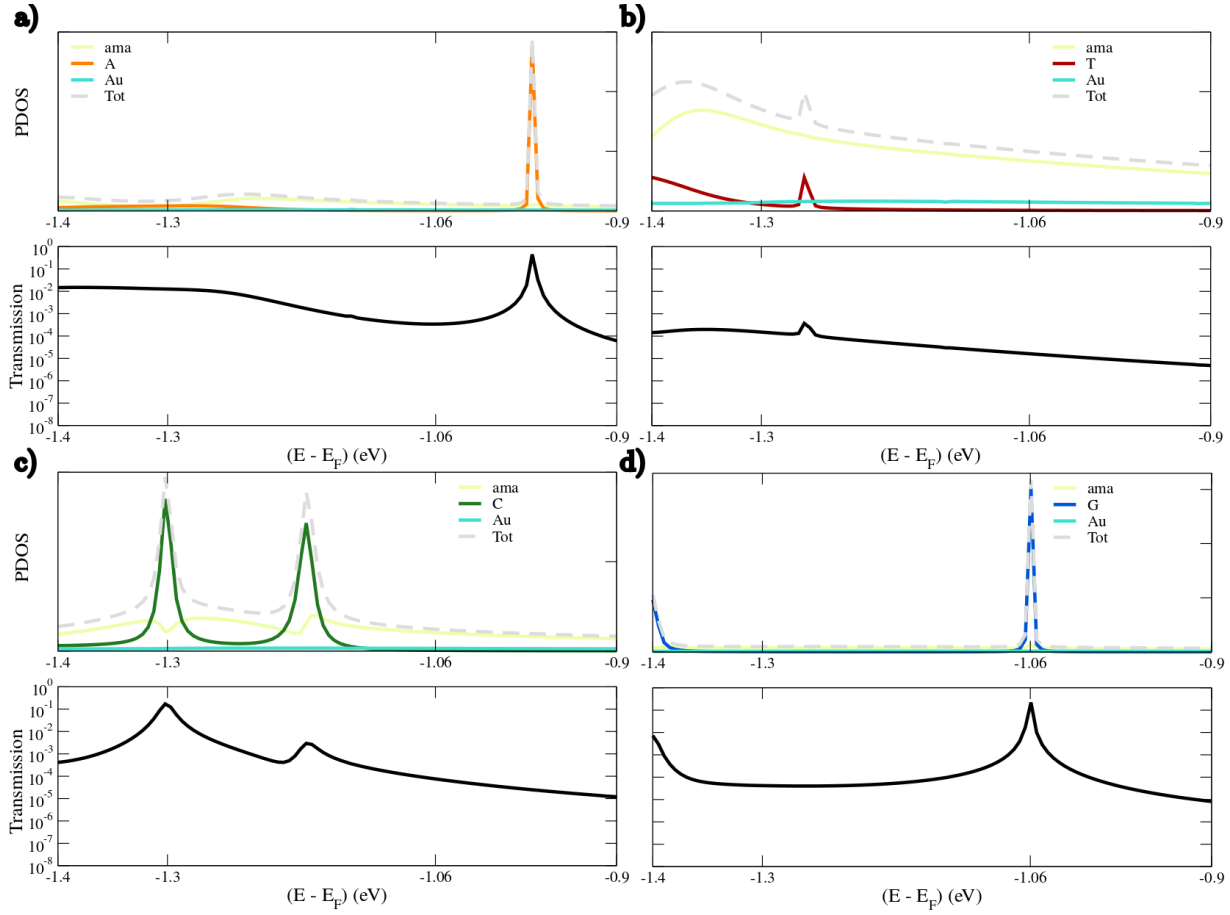

Figure A.1: PDOS (top panel) and transmission curve (bottom panel) plotted on a semi-log scale for amantine functionalized devices (Fig. 4.1b) : a) deoxyadenosine monophosphate (A), b) deoxythymidine monophosphate (T) c)deoxycytidine monophosphate (C) and d) deoxyguanosine monophosphate (G). The energy axis has been shifted so as to align zero with the Fermi energy, E_F.

B Hybrid MoS_2 Nanopore

As a preliminary study towards using a hybrid MoS_2 for biosensing, we have investigated the electronic properties of a hybrid MoS_2 based nanopore. For this a hole was opened in this material. The structure for the nanopore opening was generated by replicating six units of the 66 atom armchair unit cell shown in Fig.6.1d. Starting from the neighborhood of the identified point S vacancy at the interface from the analysis of Fig. 6.4, a pore was formed in the metallic region of monolayer. The diameter ($\approx 12.5\mathring{A}$) of the pore was chosen from a geometric consideration so as to fit in the smallest nucleotide. The resulting structure was fully relaxed with density functional theory. A kgrid of $20\times1\times20$ was used for the Monkorst-pack sampling of the density of states (DOS).

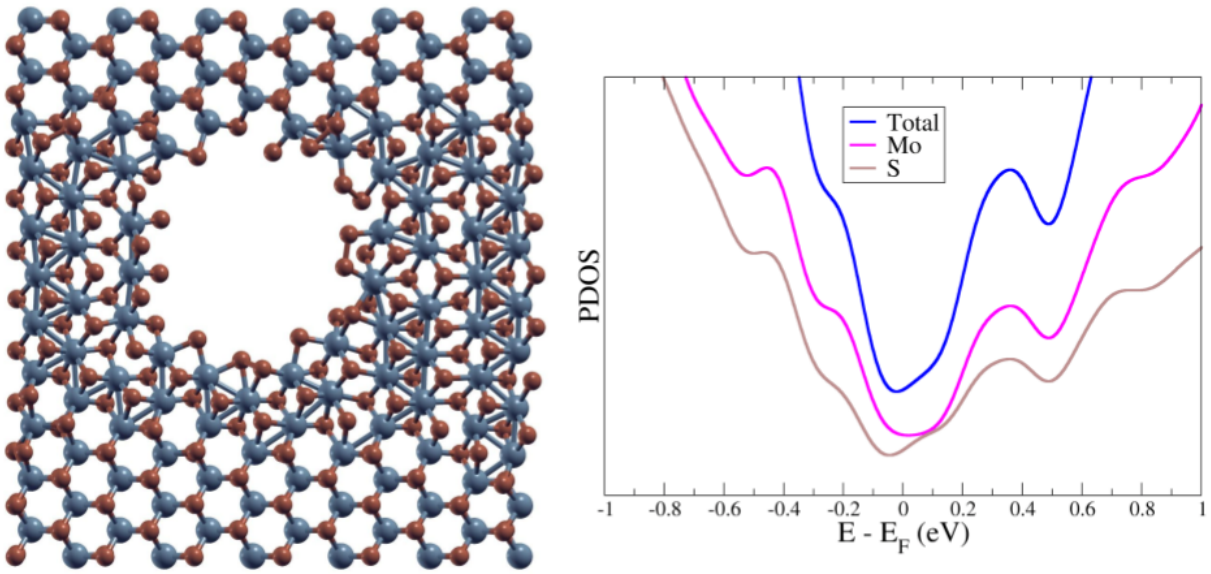

Figure B.1: *Left panel:* Hybrid MoS_2 based nanopore. *Right panel:* Density of states calculated for the structure in left panel. In all cases, the Fermi level (E_F) is aligned with zero on the energy axis.

The the *left panel* of Fig. B.1 shows the relaxed structure of nanopore. Since the pore opening was performed using geometric consideration as explained above, the pore seems to have grown more towards the top interface. The DOS plot can be seen in the *right panel* of Fig. B.1. Notice that similar to the DOS for the pristine monolayer (Fig. 6.5), the structure with the nanopore also shows occupancy at the Fermi level suggesting a metallic nature. Similar to the pristine monolayer case, the larger contribution towards the DOS comes from Mo atoms. Notice that most of the pore edges are S atom terminated as seen in the *left panel* of Fig. B.1. A number of dangling bonds can also be observed along the pore edges. Atoms or chemical groups have to be introduced to passivate the pore edges. Previous studies on 2H-MoS_2 monolayer based nanopore has not looked in to the chemical passivation of pore edges [141]. A number of chemical groups will be considered for chemical passivation of pore edges (e.g. hydrogen). The effect of such chemical passivation in promoting the structural stability, and the electronic properties of the nanopore will be examined. The non-symmetric nature of the interface is also expected to offer interesting biosensing perspectives by means of tunable current flow by gating as observed in Chapter 6. These would be considered in our further investigations.

List of Figures

List of Tables

Bibliography

[1] Building a better nanopore. *Nat Nano*, 11(2):105–105, 2016. Editorial.

[2] D. Branton, D. W. Deamer, A. Marziali, H. Bayley, S. A. Benner, T. Butler, M. Di Ventra, S. Garaj, A. Hibbs, X. Huang, S. B. Jovanovich, P. S. Krstic, S. Lindsay, X. S. Ling, C. H. Mastrangelo, A. Meller, J. S. Oliver, Y. V. Pershin, J. M. Ramsey, R. Riehn, G. V. Soni, V. Tabard-Cossa, M. Wanunu, M. Wiggin, and J. A. Schloss. The potential and challenges of nanopore sequencing. *Nat Biotech*, 26(10):1146–1153, 2008.

[3] K. Lee, É. D. Murray, L. Kong, B. I. Lundqvist, and D. C. Langreth. Higher-accuracy van der waals density functional. *Phys. Rev. B*, 82:081101, 2010.

[4] K. K. Saha, M. Drndić, and B. K. Nikolić. DNA base-specific modulation of microampere transverse edge currents through a metallic graphene nanoribbon with a nanopore. *Nano Letters*, 12(1):50–55, 2012.

[5] S. Carson and M. Wanunu. Challenges in DNA motion control and sequence readout using nanopore devices. *Nanotechnology*, 26(7):074004, 2015.

[6] J. M. Berg, J. L. Tymoczko, and L. Stryer. *Biochemistry, Fifth Edition*. W.H. Freeman, 2002.

[7] J. D. Watson and F. H. C. Crick. A structure for deoxyribose nucleic acid. *Nature*, 171:737–738, 1953.

[8] M. Tyers and M. Mann. From genomics to proteomics. *Nature*, 422(6928):193–197, 2003.

[9] M. Kuroda, T. Ohta, I. Uchiyama, T. Baba, H. Yuzawa, I. Kobayashi, L. Cui, A. Oguchi, K. Aoki, Y. Nagai, J. Lian, T. Ito, M. Kanamori, H. Matsumaru, A. Maruyama, H. Murakami, A. Hosoyama, Y. Mizutani-Ui, N. K. Takahashi, T. Sawano, R. Inoue, C. Kaito, K. Sekimizu, H. Hirakawa, S. Kuhara, S. Goto,

J. Yabuzaki, M. Kanehisa, A. Yamashita, K. Oshima, K. Furuya, C. Yoshino, T. Shiba, M. Hattori, N. Ogasawara, H. Hayashi, and K. Hiramatsu. Whole genome sequencing of meticillin-resistant staphylococcus aureus. *Lancet*, 357(9264):1225–1240, 2001.

[10] P. W. Laird. The power and the promise of DNA methylation markers. *Nat Rev Cancer*, 3(4):253–266, 2003.

[11] S. Kanvah, J. Joseph, G. B. Schuster, R. N. Barnett, C. L. Cleveland, and U. Landman. Oxidation of DNA: Damage to nucleobases. *Accounts of Chemical Research*, 43(2):280–287, 2010.

[12] L. Chin, J. N. Andersen, and P. A. Futreal. Cancer genomics: from discovery science to personalized medicine. *Nat Med*, 17(3):297–303, 2011.

[13] G. S. Ginsburg and H. F. Willard. Genomic and personalized medicine: foundations and applications. *Translational Research*, 154(6):277–287, 2009.

[14] `https://www.genome.gov/11006943/`.

[15] F. Sanger, S. Nicklen, and A. R. Coulson. DNA sequencing with chain-terminating inhibitors. *Proceedings of the National Academy of Sciences*, 74(12):5463–5467, 1977.

[16] `https://www.genome.gov/27541954/dna-sequencing-costs-data/`.

[17] D. A. Wheeler, M. Srinivasan, M. Egholm, Y. Shen, L. Chen, A. McGuire, W. He, Y. Chen, V. Makhijani, G. T. Roth, X. Gomes, K. Tartaro, F. Niazi, C. L. Turcotte, G. P. Irzyk, J. R. Lupski, C. Chinault, X. Song, Y. Liu, Y. Yuan, L. Nazareth, X. Qin, D. M. Muzny, M. Margulies, G. M. Weinstock, R. A. Gibbs, and J. M. Rothberg. The complete genome of an individual by massively parallel DNA sequencing. *Nature*, 452(7189):872–876, 2008.

[18] L. J. Steinbock and A. Radenovic. The emergence of nanopores in next-generation sequencing. *Nanotechnology*, 26(7):074003, 2015.

[19] B. M. Venkatesan and R. Bashir. Nanopore sensors for nucleic acid analysis. *Nat Nano*, 6(10):615–624, 2011.

[20] W. Humphrey, A. Dalke, and K. Schulten. VMD – Visual Molecular Dynamics. *Journal of Molecular Graphics*, 14:33–38, 1996.

[21] M. Wanunu, J. Sutin, B. McNally, A. Chow, and A. Meller. DNA translocation governed by interactions with solid-state nanopores. *Biophysical Journal*, 95(10):4716–4725, 2008.

[22] M. Fyta. Threading DNA through nanopores for biosensing applications. *Journal of Physics: Condensed Matter*, 27(27):273101, 2015.

[23] J. J. Kasianowicz, E. Brandin, D. Branton, and D. W. Deamer. Characterization of individual polynucleotide molecules using a membrane channel. *Proceedings of the National Academy of Sciences*, 93(24):13770–13773, 1996.

[24] `https://www.nanoporetech.com/products-services/minion-mki`.

[25] A. H. Laszlo, I. M. Derrington, B. C. Ross, H. Brinkerhoff, A. Adey, I. C. Nova, J. M. Craig, K. W. Langford, J. M. Samson, R. Daza, K. Doering, J. Shendure, and J. H. Gundlach. Decoding long nanopore sequencing reads of natural DNA. *Nat Biotech*, 32(8):829–833, 2014.

[26] S. Lindsay. The promises and challenges of solid-state sequencing. *Nat Nano*, 11(2):109–111, 2016.

[27] B. N. Miles, A. P. Ivanov, K. A. Wilson, F. Dogan, D. Japrung, and J. B. Edel. Single molecule sensing with solid-state nanopores: novel materials, methods, and applications. *Chem. Soc. Rev.*, 42:15–28, 2013.

[28] A. J. Storm, J. H. Chen, X. S. Ling, H. W. Zandbergen, and C. Dekker. Fabrication of solid-state nanopores with single-nanometre precision. *Nat Mater*, 2(8):537–540, 2003.

[29] J. Li, D. Stein, C. McMullan, D. Branton, M. J. Aziz, and J. A. Golovchenko. Ion-beam sculpting at nanometre length scales. *Nature*, 412(6843):166–169, 2001.

[30] S. J. Heerema and C. Dekker. Graphene nanodevices for DNA sequencing. *Nat Nano*, 11(2):127–136, Feb 2016.

[31] M. Zwolak and M. Di Ventra. Electronic signature of DNA nucleotides via transverse transport. *Nano Letters*, 5(3):421–424, 2005.

[32] J. Lagerqvist, M. Zwolak, and M. Di Ventra. Fast DNA sequencing via transverse electronic transport. *Nano Letters*, 6(4):779–782, 2006.

[33] M. Tsutsui, M. Taniguchi, and T. Kawai. Fabrication of 0.5 nm electrode gaps using self-breaking technique. *Applied Physics Letters*, 93(16):163115, 2008.

[34] M. Tsutsui, M. Taniguchi, K. Yokota, and T. Kawai. Identifying single nucleotides by tunnelling current. *Nat Nano*, 5(4):286–290, 2010.

[35] `http://www.quantumbiosystems.com/`.

[36] M. Di Ventra and M. Taniguchi. Decoding DNA, RNA and peptides with quantum tunnelling. *Nat Nano*, 11(2):117–126, 2016.

[37] J. Prasongkit, G. T. Feliciano, A. R. Rocha, Y. He, T. Osotchan, R. Ahuja, and R. H. Scheicher. Theoretical assessment of feasibility to sequence DNA through interlayer electronic tunneling transport at aligned nanopores in bilayer graphene. *Scientific Reports*, 5:17560, 2015.

[38] A. P. Marchand. Diamondoid hydrocarbons–delving into nature's bounty. *Science*, 299(5603):52–53, 2003.

[39] J. E. Dahl, S. G. Liu, and R. M. K. Carlson. Isolation and structure of higher diamondoids, nanometer-sized diamond molecules. *Science*, 299(5603):96–99, 2003.

[40] Y. Zhou, A. D. Brittain, D. Kong, M. Xiao, Y. Meng, and L. Sun. Derivatization of diamondoids for functional applications. *J. Mater. Chem. C*, 3:6947–6961, 2015.

[41] G. C. McIntosh, M. Yoon, S. Berber, and D. Tománek. Diamond fragments as building blocks of functional nanostructures. *Phys. Rev. B*, 70:045401, 2004.

[42] W. L. Yang, J. D. Fabbri, T. M. Willey, J. R. I. Lee, J. E. Dahl, R. M. K. Carlson, P. R. Schreiner, A. A. Fokin, B. A. Tkachenko, N. A. Fokina, W. Meevasana, N. Mannella, K. Tanaka, X. J. Zhou, T. van Buuren, M. A. Kelly, Z. Hussain, N. A. Melosh, and Z.-X. Shen. Monochromatic electron photoemission from diamondoid monolayers. *Science*, 316(5830):1460–1462, 2007.

[43] L. Landt, K. Klünder, J. E. Dahl, R. M. K. Carlson, T. Möller, and C. Bostedt. Optical response of diamond nanocrystals as a function of particle size, shape, and symmetry. *Phys. Rev. Lett.*, 103:047402, 2009.

[44] M. Vörös and A. Gali. Optical absorption of diamond nanocrystals from *ab initio* density-functional calculations. *Phys. Rev. B*, 80:161411, 2009.

[45] M. Vörös, T. Demjén, T. Szilvási, and A. Gali. Tuning the optical gap of nanometer-size diamond cages by sulfurization: A time-dependent density functional study. *Phys. Rev. Lett.*, 108:267401, 2012.

[46] L. Landt, C. Bostedt, D. Wolter, T. Möller, J. E. P. Dahl, R. M. K. Carlson, B. A. Tkachenko, A. A. Fokin, P. R. Schreiner, A. Kulesza, R. Mitrić, and V. Bonačić-Koutecký. Experimental and theoretical study of the absorption properties of thiolated diamondoids. *The Journal of Chemical Physics*, 132(14):144305, 2010.

[47] B. Adhikari and M. Fyta. Towards double-functionalized small diamondoids: selective electronic band-gap tuning. *Nanotechnology*, 26(3):035701, 2015.

[48] H. Schwertfeger, A. A. Fokin, and P. R. Schreiner. Diamonds are a chemist's best friend: Diamondoid chemistry beyond adamantane. *Angewandte Chemie International Edition*, 47(6):1022–1036, 2008.

[49] W. A. Clay, J. E. P. Dahl, R. M. K. Carlson, N. A. Melosh, and Z-X. Shen. Physical properties of materials derived from diamondoid molecules. *Reports on Progress in Physics*, 78(1):016501, 2015.

[50] N. D. Drummond. Nanomaterials: Diamondoids display their potential. *Nat Nano*, 2(8):462–463, 2007.

[51] G. Sivaraman, R. G Amorim, R. H. Scheicher, and M. Fyta. Diamondoid-functionalized gold nanogaps as sensors for natural, mutated, and epigenetically modified DNA nucleotides. *Nanoscale*, 8(19):10105–10112, 2016.

[52] L. Wanka, K. Iqbal, and P. R. Schreiner. The lipophilic bullet hits the targets: Medicinal chemistry of adamantane derivatives. *Chemical Reviews*, 113(5):3516–3604, 2013.

[53] Y. Xue and G. A. Mansoori. Self-assembly of diamondoid molecules and derivatives (md simulations and dft calculations). *International Journal of Molecular Sciences*, 11(1):288–303, 2010.

[54] B. Adhikari, S. Meng, and M. Fyta. Carbene-mediated self-assembly of diamondoids on metal surfaces. *Nanoscale*, 8:8966–8975, 2016.

[55] S. B. Legoas, R. P. B. dos Santos, K. S. Troche, V. R. Coluci, and D. S. Galvão. Ordered phases of encapsulated diamondoids into carbon nanotubes. *Nanotechnology*, 22(31):315708, 2011.

[56] G. Sivaraman, F. A. L. de Souza, R. G. Amorim, W. L. Scopel, M. Fyta, and R. H. Scheicher. Electronic transport along hybrid MoS_2 monolayers. *The Journal of Physical Chemistry C*, 120(41):23389–23396, 2016.

[57] E. Kaxiras. *Atomic and electronic structure of solids*. Cambridge University Press, 2003.

[58] P. Hohenberg and W. Kohn. Inhomogeneous electron gas. *Phys. Rev.*, 136:B864–B871, 1964.

[59] W. Kohn and L. J. Sham. Self-consistent equations including exchange and correlation effects. *Phys. Rev.*, 140:A1133–A1138, 1965.

[60] A. D. Becke. Density-functional exchange-energy approximation with correct asymptotic behavior. *Phys. Rev. A*, 38:3098–3100, 1988.

[61] Chengteh Lee, Weitao Yang, and Robert G. Parr. Development of the colle-salvetti correlation-energy formula into a functional of the electron density. *Phys. Rev. B*, 37:785–789, 1988.

[62] J. P. Perdew, K. Burke, and M. Ernzerhof. Generalized gradient approximation made simple. *Phys. Rev. Lett.*, 77:3865–3868, 1996.

[63] K. Burke. Perspective on density functional theory. *The Journal of chemical physics*, 136(15):150901, 2012.

[64] J. Kohanoff. *Electronic structure calculations for solids and molecules: theory and computational methods*. Cambridge University Press, 2006.

[65] D. R. Hamann, M. Schlüter, and C. Chiang. Norm-conserving pseudopotentials. *Phys. Rev. Lett.*, 43:1494–1497, 1979.

[66] J. Junquera, Ó. Paz, D. Sánchez-Portal, and E. Artacho. Numerical atomic orbitals for linear-scaling calculations. *Phys. Rev. B*, 64:235111, 2001.

[67] S.F. Boys and F. Bernardi. The calculation of small molecular interactions by the differences of separate total energies. some procedures with reduced errors. *Molecular Physics*, 19(4):553–566, 1970.

[68] J. R. Heath and M. A. Ratner. Molecular electronics. *Physics Today*, 56:43–49, 2003.

[69] W. Y. Kim, Y. C. Choi, S. K. Min, Y. Cho, and K. S. Kim. Application of quantum chemistry to nanotechnology: electron and spin transport in molecular devices. *Chemical Society Reviews*, 38(8):2319–2333, 2009.

[70] A. K. Geim and K. S. Novoselov. The rise of graphene. *Nature materials*, 6(3):183–191, 2007.

[71] Y. Xue, S. Datta, and M. A. Ratner. First-principles based matrix Green's function approach to molecular electronic devices: general formalism. *Chemical Physics*, 281(2):151–170, 2002.

[72] S. Datta. Nanoscale device modeling: the Green's function method. *Superlattices and microstructures*, 28(4):253–278, 2000.

[73] M. Paulsson. Non equilibrium green's functions for dummies: Introduction to the one particle NEGF equations. *arXiv preprint cond-mat/0210519*, 2002.

[74] S. Datta. *Quantum transport: atom to transistor*. Cambridge University Press, 2005.

[75] M. Di Ventra. *Electrical transport in nanoscale systems*, volume 14. Cambridge University Press.

[76] M. Brandbyge, J. Mozos, P. Ordejón, J. Taylor, and K. Stokbro. Density-functional method for nonequilibrium electron transport. *Phys. Rev. B*, 65:165401, 2002.

[77] H. He, R. H. Scheicher, , R. Pandey, A. R. Rocha, , S. Sanvito, A. Grigoriev, , R. Ahuja, and S. P. Karna. Functionalized nanopore-embedded electrodes for rapid dna sequencing. *The Journal of Physical Chemistry C*, 112(10):3456–3459, 2008.

[78] A. L. Stouffer, R. Acharya, D. Salom, A. S. Levine, L. Di Costanzo, C. S. Soto, V. Tereshko, V. Nanda, S. Stayrook, and W. F. DeGrado. Structural basis for the function and inhibition of an influenza virus proton channel. *Nature*, 451(7178):596–599, 2008.

[79] H. Huang, E. Pierstorff, E. Osawa, and D. Ho. Active nanodiamond hydrogels for chemotherapeutic delivery. *Nano Letters*, 7(11):3305–3314, 2007.

[80] A. A. Spasov, T. V. Khamidova, L. I. Bugaeva, and I. S. Morozov. Adamantane derivatives: Pharmacological and toxicological properties (review). *Pharmaceutical Chemistry Journal*, 34(1):1–7, 2000.

[81] J. R. Schnell and J. J. Chou. Structure and mechanism of the m2 proton channel of influenza a virus. *Nature*, 451(7178):591–595, 2008.

[82] W. J. Geldenhuys, S. F. Malan, J. R. Bloomquist, A. P. Marchand, and C. J. Van der Schyf. Pharmacology and structure-activity relationships of bioactive polycyclic cage compounds: A focus on pentacycloundecane derivatives. *Medicinal Research Reviews*, 25(1):21–48, 2005.

[83] B. Adhikari, G. Sivaraman, and M. Fyta. Diamondoid-based molecular junction: a computational study. *Nanotechnology , (2016)*, 27:485207, 2016.

[84] Y. Wang, E. Kioupakis, X. Lu, D. Wegner, R. Yamachika, J. E. Dahl, R. M. K. Carlson, S. G. Louie, and M. F. Crommie. Spatially resolved electronic and vibronic properties of single diamondoid molecules. *Nat Mater*, 7(1):38–42, 2008.

[85] K. T. Narasimha, C. Ge, J. D. Fabbri, W. Clay, B. A. Tkachenko, A. A. Fokin, Peter R. Schreiner, J. E. Dahl, R. M. K. Carlson, S. X., and N. A. Melosh. Ultralow effective work function surfaces using diamondoid monolayers. *Nat Nano*, 11(3):267–272, 2016.

[86] L. Landt, M. Staiger, D. Wolter, K. Klünder, P. Zimmermann, T. M. Willey, T. van Buuren, D. Brehmer, P. R. Schreiner, B. A. Tkachenko, A. A. Fokin, T. Möller, and C. Bostedt. The influence of a single thiol group on the electronic and optical properties of the smallest diamondoid adamantane. *The Journal of Chemical Physics*, 132(2):024710, 2010.

[87] T. Rander, M. Staiger, R. Richter, T. Zimmermann, L. Landt, D. Wolter, J. E. Dahl, R. M. K. Carlson, B. A. Tkachenko, N. A. Fokina, P. R. Schreiner, T. Möller, and C. Bostedt. Electronic structure tuning of diamondoids through functionalization. *The Journal of Chemical Physics*, 138(2):024310, 2013.

[88] J. M. Soler, E. Artacho, J. D. Gale, A. García, J. Junquera, P. Ordejón, and D. Sánchez-Portal. The SIESTA method for ab initio order- n materials simulation. *Journal of Physics: Condensed Matter*, 14(11):2745, 2002.

[89] N. Troullier and J. L. Martins. Efficient pseudopotentials for plane-wave calculations. *Phys. Rev. B*, 43:1993–2006, 1991.

[90] J. Klimeš and A. Michaelides. Perspective: Advances and challenges in treating van der waals dispersion forces in density functional theory. *The Journal of Chemical Physics*, 137(12):120901, 2012.

[91] J Šponer, P. Jurečka, and P. Hobza. Accurate interaction energies of hydrogen-bonded nucleic acid base pairs. *Journal of the American Chemical Society*, 126(32):10142–10151, 2004.

[92] V. R. Cooper, T. Thonhauser, and D. C. Langreth. An application of the van der waals density functional: Hydrogen bonding and stacking interactions between nucleobases. *The Journal of Chemical Physics*, 128(20):204102, 2008.

[93] J. Ireta, J. Neugebauer, and M. Scheffler. On the accuracy of DFT for describing hydrogen bonds: dependence on the bond directionality. *The Journal of Physical Chemistry A*, 108(26):5692–5698, 2004.

[94] T. Steiner. The hydrogen bond in the solid state. *Angewandte Chemie International Edition*, 41(1):48–76, 2002.

[95] C. S. Ku and D. H. Roukos. From next-generation sequencing to nanopore sequencing technology: paving the way to personalized genomic medicine. *Expert review of medical devices*, 10(1):1–6, 2013.

[96] P. W. Laird. The power and the promise of DNA methylation markers. *Nat Rev Cancer*, 3:253–266, 2003.

[97] S. Kanvah, J. Joseph, G. B. Schuster, R. N. Barnett, C. L. Cleveland, and U. Landman. Oxidation of DNA: Damage to nucleobases. *Accounts of Chemical Research*, 43(2):280—-287, 2010.

[98] G. Sivaraman and M. Fyta. Chemically modified diamondoids as biosensors for DNA. *Nanoscale*, 6:4225–4232, 2014.

[99] G. Sivaraman and M. Fyta. Diamondoids as DNA methylation and mutation probes. *EPL*, 108:17005, 2014.

[100] E. L. van Dijk, H. Auger, Y. Jaszczyszyn, and C. Thermes. Ten years of next-generation sequencing technology. *Trends in Genetics*, 30(9):418–426, 2014.

[101] Amit Meller, Lucas Nivon, and Daniel Branton. Voltage-driven dna translocations through a nanopore. *Phys. Rev. Lett.*, 86:3435–3438, 2001.

[102] M. Tsutsui, M. Taniguchi, K. Yokota, and T. Kawai. Identifying single nucleotides by tunnelling current. *Nat. Nanotechnol.*, 5(4):286–290, 2010.

[103] P. Krstić, B. Ashcroft, and S. Lindsay. Physical model for recognition tunneling. *Nanotechnology*, 26(8):084001.

[104] N. Okabayashi, M. Paulsson, H. Ueba, Y. Konda, and T. Komeda. Inelastic tunneling spectroscopy of alkanethiol molecules: High-resolution spectroscopy and theoretical simulations. *Phys. Rev. Lett.*, 104:077801, 2010.

[105] T. M. Willey, J. D. Fabbri, J. R. I. Lee, P. R. Schreiner, A. A. Fokin, B. A. Tkachenko, N. A. Fokina, J. E. P. Dahl, R. M. K. Carlson, A. L. Vance, W. Yang, L. J. Terminello, T. van Buuren, and N. A. Melosh. Near-edge X-ray absorption fine structure spectroscopy of diamondoid thiol monolayers on gold. *Journal of the American Chemical Society*, 130(32):10536—-10544, 2008.

[106] R. H. Scheicher, A. Grigoriev, and R. Ahuja. DNA sequencing with nanopores from an ab initio perspective. *Journal of Materials Science*, 47:7439–7446, 2012.

[107] N. W. Ashcroft and N. D. Mermin. *Solid State Physics*. Holt, Rinehart and Winston, New York, 1976.

[108] S. K. Min, W. Y. Kim, Y. Cho, and K. S. Kim. Fast DNA sequencing with a graphene-based nanochannel device. *Nature Nanotechnology*, 6(3):162–165, 2011.

[109] M. Paulsson and M. Brandbyge. Transmission eigenchannels from nonequilibrium Green's functions. *Phys. Rev. B*, 76:115117, 2007.

[110] W. Ding, C. F. A. Negre, L. Vogt, and V. S. Batista. Single molecule rectification induced by the asymmetry of a single frontier orbital. *Journal of Chemical Theory and Computation*, 10(8):3393–3400, 2014.

[111] A. Batra, P. Darancet, Q. Chen, J. S. Meisner, J. R. Widawsky, J. B. Neaton, C. Nuckolls, and L. Venkataraman. Tuning rectification in single-molecular diodes. *Nano Letters*, 13(12):6233–6237, 2013.

[112] F. C. Maier, G. Sivaraman, and M. Fyta. The role of a diamondoid as a hydrogen donor or acceptor in probing DNA nucleobases. *Eur. Phys. J. E*, 37:95, 2014.

[113] M. Zwolak and M. Di Ventra. *Colloquium* : Physical approaches to DNA sequencing and detection. *Rev. Mod. Phys.*, 80:141–165, 2008.

[114] S. Huang, J. He, S. Chang, P. Zhang, F. Liang, S. Li, M. Tuchband, A. Fuhrmann, R. Ros, and S. Lindsay. Identifying single bases in a DNA oligomer with electron tunnelling. *Nat Nano*, 5(12):868—-873, 2010.

[115] D. Deamer, M. Akeson, and D. Branton. Three decades of nanopore sequencing. *Nat Biotech*, 34(5):518—-524, 2016.

[116] G. Sivaraman, R. G. Amorim, R. H. Scheicher, and M. Fyta. Benchmark investigation of diamondoid-functionalized electrodes for nanopore DNA sequencing. *Nanotechnology*, 27(41):414002, 2016.

[117] S. Lebègue and O. Eriksson. Electronic structure of two-dimensional crystals from *Ab Initio* theory. *Phys. Rev. B*, 79:115409, 2009.

[118] S. Lebègue, T. Björkman, M. Klintenberg, R. M. Nieminen, and O. Eriksson. Two-dimensional materials from data filtering and *Ab Initio* calculations. *Phys. Rev. X*, 3:031002, 2013.

[119] R. Mas-Balleste, C. Gomez-Navarro, J. Gomez-Herrero, and F. Zamora. 2D materials: To graphene and beyond. *Nanoscale*, 3:20–30, 2011.

[120] K. F. Mak, C. Lee, J. Hone, J. Shan, and T. F. Heinz. Atomically thin MoS_2: A new direct-gap semiconductor. *Phys. Rev. Lett.*, 105:136805, 2010.

[121] J. N. Coleman, M. Lotya, A. O'Neill, S. D. Bergin, P. J. King, U. Khan, K. Young, A. Gaucher, S. De, R. J. Smith, I. V. Shvets, S. K. Arora, G. Stanton, H. Kim, K. Lee, G. T. Kim, G. S. Duesberg, T. Hallam, J. J. Boland, J. J. Wang, J. F. Donegan, J. C. Grunlan, G. Moriarty, A. Shmeliov, R. J. Nicholls, J. M. Perkins, E. M. Grieveson, K. Theuwissen, D. W. McComb, P. D. Nellist, and V. Nicolosi. Two-dimensional nanosheets produced by liquid exfoliation of layered materials. *Science*, 331(6017):568–571, 2011.

[122] K. Wang, J. Wang, J. Fan, M. Lotya, A. O'Neill, D. Fox, Y. Feng, X. Zhang, B. Jiang, Q. Zhao, H. Zhang, J. N. Coleman, L. Zhang, and W. J. Blau. Ultrafast saturable absorption of two-dimensional MoS_2 nanosheets. *ACS Nano*, 7(10):9260–9267, 2013.

[123] A. Ambrosi, Z. Sofer, and M. Pumera. $2H \rightarrow 1T$ phase transition and hydrogen evolution activity of MoS_2, $MoSe_2$, WS_2 and WSe_2 strongly depends on the MX_2 composition. *Chem. Commun.*, 51:8450–8453, 2015.

[124] Y. Feldman, E. Wasserman, D. J. Srolovitz, and R. Tenne. High-rate, gas-phase growth of MoS_2 nested inorganic fullerenes and nanotubes. *Science*, 267(5195):222–225, 1995.

[125] J. V. Lauritsen, M. V. Bollinger, E. Lægsgaard, K. W. Jacobsen, J. K. Nørskov, B. S. Clausen, H. Topsøe, and F. Besenbacher. Atomic-scale insight into structure and morphology changes of MoS_2 nanoclusters in hydrotreating catalysts. *J. Catal.*, 221(2):510–522, 2004.

[126] K. L. McBride and J. D. Head. DFT investigation of MoS_2 nanoclusters used as desulfurization catalysts. *Int. J. Quantum Chem*, 109(15):3570–3582, 2009.

[127] S. Cristol, J. F. Paul, E. Payen, D. Bougeard, S. Clémendot, and F. Hutschka. Theoretical study of the MoS_2 (100) surface: a chemical potential analysis of sulfur and hydrogen coverage. 2. effect of the total pressure on surface stability. *J. Phys. Chem. B*, 106(22):5659–5667, 2002.

[128] M. Huang and K. Cho. Density functional theory study of CO hydrogenation on a MoS_2 surface. *J. Phys. Chem. C*, 113(13):5238–5243, 2009.

[129] V. Alexiev, R. Prins, and T. Weber. DFT study of MoS_2 and hydrogen adsorbed on the $(10\bar{1}0)$ face of MoS_2. *Phys. Chem. Chem. Phys.*, 3:5326–5336, 2001.

[130] Q. H. Wang, K. Kalantar-Zadeh, A. Kis, J. N. Coleman, and M. S. Strano. Electronics and optoelectronics of two-dimensional transition metal dichalcogenides. *Nat. Nanotechnol.*, 7(11):699–712, 2012.

[131] Y. Lin, D. O. Dumcenco, Y. Huang, and K. Suenaga. Atomic mechanism of the semiconducting-to-metallic phase transition in single-layered MoS_2. *Nat. Nanotechnol.*, 9(5):391–396, 2014.

[132] I. Song, C. Park, and H. C. Choi. Synthesis and properties of molybdenum disulphide: from bulk to atomic layers. *RSC Adv.*, 5:7495–7514, 2015.

[133] D. Voiry, A. Mohite, and M. Chhowalla. Phase engineering of transition metal dichalcogenides. *Chem. Soc. Rev.*, 44:2702–2712, 2015.

[134] G. Eda, H. Yamaguchi, D. Voiry, T. Fujita, M. Chen, and M. Chhowalla. Photoluminescence from chemically exfoliated MoS_2. *Nano Lett.*, 11(12):5111–5116, 2011.

[135] G. Eda, T. Fujita, H. Yamaguchi, D. Voiry, M. Chen, and M. Chhowalla. Coherent atomic and electronic heterostructures of single-layer MoS_2. *ACS Nano*, 6(8):7311–7317, 2012.

[136] W. Qiao, S. Yan, X. Song, X. Zhang, X. He, W. Zhong, and Y. Du. Luminescent monolayer MoS_2 quantum dots produced by multi-exfoliation based on lithium intercalation. *Appl. Surf. Sci.*, 359:130–136, 2015.

[137] X. Guo, G. Yang, J. Zhang, and X. Xu. Structural, mechanical and electronic properties of in-plane 1T/2H phase interface of MoS_2 heterostructures. *AIP Adv.*, 5(9):097174, 2015.

[138] R. Kappera, D. Voiry, S. E. Yalcin, B. Branch, G. Gupta, A. D. Mohite, and M. Chhowalla. Phase-engineered low-resistance contacts for ultrathin MoS_2 transistors. *Nat. Mater.*, 13(12):1128–1134, 2014.

[139] K. Liu, J. Feng, A. Kis, and A. Radenovic. Atomically thin molybdenum disulfide nanopores with high sensitivity for DNA translocation. *ACS Nano*, 8(3):2504–2511, 2014.

[140] J. Feng, K. Liu, M. Graf, M. Lihter, R. D. Bulushev, D. Dumcenco, D. T. L. Alexander, D. Krasnozhon, T. Vuletic, A. Kis, and A. Radenovic. Electrochemical reaction in single layer MoS_2: Nanopores opened atom by atom. *Nano Lett.*, 15(5):3431–3438, 2015.

[141] A. B. Farimani, K. Min, and N. R. Aluru. DNA base detection using a single-layer MoS_2. *ACS Nano*, 8(8):7914–7922, 2014.

[142] J. Feng, K. Liu, R. D. Bulushev, S. Khlybov, D. Dumcenco, A. Kis, and A. Radenovic. Identification of single nucleotides in MoS_2 nanopores. *Nat. Nanotechnol.*, 10(12):1070–1076, 2015.

[143] B. Cho, M. G. Hahm, M. Choi, J. Yoon, A. R. Kim, Y. Lee, S. Park, J. Kwon, C. S. Kim, M. Song, Y. Jeong, K. Nam, S. Lee, T. J. Yoo, C. G. Kang, B. H. Lee, H. C. Ko, P. M. Ajayan, and D. Kim. Charge-transfer-based gas sensing using atomic-layer MoS_2. *Sci. Rep.*, 5:8052, 2015.

[144] G. Liu, S. L. Rumyantsev, C. Jiang, M. S. Shur, and A. A. Balandin. Selective gas sensing with h-BN capped MoS_2 heterostructure thin-film transistors. *IEEE Electron Device Lett.*, 36(11):1202–1204, 2015.

[145] F. K. Perkins, A. L. Friedman, E. Cobas, P. M. Campbell, G. G. Jernigan, and B. T. Jonker. Chemical vapor sensing with monolayer MoS_2. *Nano Lett.*, 13(2):668–673, 2013.

[146] D. J. Late, Y. Huang, B. Liu, J. Acharya, S. N. Shirodkar, J. Luo, A. Yan, D. Charles, U. V. Waghmare, V. P. Dravid, and C. N. R. Rao. Sensing behavior of atomically thin-layered MoS_2 transistors. *ACS Nano*, 7(6):4879–4891, 2013.

[147] Y. Ding, Y. Wang, J. Ni, L. Shi, S. Shi, and W. Tang. First principles study of structural, vibrational and electronic properties of graphene-like MX_2 (M= Mo, Nb, W, Ta; X= S, Se, Te) monolayers. *Physica B: Condensed Matter*, 406(11):2254–2260, 2011.

[148] P. Johari and V. B. Shenoy. Tuning the electronic properties of semiconducting transition metal dichalcogenides by applying mechanical strains. *ACS Nano*, 6(6):5449–5456, 2012.

[149] M. Kan, J. Y. Wang, X. W. Li, S. H. Zhang, Y. W. Li, Y. Kawazoe, Q. Sun, and P. Jena. Structures and phase transition of a MoS_2 monolayer. *J. Phys. Chem. C*, 118(3):1515–1522, 2014.

[150] K. N. Duerloo, Y. Li, and E. J. Reed. Structural phase transitions in two-dimensional Mo- and W-dichalcogenide monolayers. *Nat. Commun.*, 5(4214), 2014.

[151] Z. Hu, S. Zhang, Y. Zhang, D. Wang, H. Zeng, and L. Liu. Modulating the phase transition between metallic and semiconducting single-layer MoS_2 and WS_2 through size effects. *Phys. Chem. Chem. Phys.*, 17(2):1099–1105, 2015.

[152] J. Heising and M. G. Kanatzidis. Structure of restacked MoS_2 and WS_2 elucidated by electron crystallography. *J. Am. Chem. Soc.*, 121(4):638–643, 1999.

[153] K. C. Santosh, R. C. Longo, R. Addou, R. M. Wallace, and K. Cho. Impact of intrinsic atomic defects on the electronic structure of MoS_2 monolayers. *Nanotechnology*, 25(37):375703, 2014.

[154] J. Hong, Z. Hu, M. Probert, K. Li, D. Lv, X. Yang, L. Gu, N. Mao, Q. Feng, L. Xie, J. Zhang, D. Wu, Z. Zhang, C. Jin, W. Ji, X. Zhang, J. Yuan, and Z. Zhang. Exploring atomic defects in molybdenum disulphide monolayers. *Nat. Commun.*, 6(6293), 2015.

[155] Q. Tang and D. Jiang. Stabilization and band-gap tuning of the 1T-MoS_2 monolayer by covalent functionalization. *Chem. Mater.*, 27(10):3743–3748, 2015.

[156] B. Radisavljevic, A. Radenovic, J. Brivio, i. V. Giacometti, and A. Kis. Single-layer MoS_2 transistors. *Nat. Nanotechnol.*, 6(3):147–150, 2011.

[157] `http://dipc.ehu.es/frederiksen/inelastica/index.php/Main_Page`.